Atmospheric Ozone Retrieval using Radiance Measurements from the Chappuis and Hartley-Huggins Absorption Bands

A Thesis
Submitted to the Faculty of Graduate Studies and Research
in Partial Fulfillment of the Requirements
for the Degree of
Master of Science
in the Department of Physics and Engineering Physics

by
Christopher Z. Roth
Saskatoon, Saskatchewan

In presenting this thesis in partial fulfillment of the requirements for a Postgraduate degree from the University of Saskatchewan, the author agrees that the Libraries of this University may make it freely available for inspection. The author further agrees that permission for copying of this thesis in any manner, in whole or in part, for scholarly purposes may be granted by the professor who supervised this thesis work or, in his absence, by the Head of the Department or the Dean of the College in which this thesis work was done. It is understood that any copying or publication or use of this thesis or parts thereof for financial gain shall not be allowed without written approval from the author. It is also understood that due recognition shall be given to the author and to the University of Saskatchewan in any scholarly use which may be made of any material in this thesis.

Requests for permission to copy or to make other use of material in this thesis in whole or in part should be addressed to:

Head of the Department of Physics and Engineering Physics
116 Science Place
University of Saskatchewan
Saskatoon, Saskatchewan
Canada
S7N 5E2

Abstract

The monitoring of global ozone in the atmosphere is a necessary prerequisite to understanding atmospheric chemistry and managing atmospheric constituents. Satellite systems have been developed to measure ozone and other constituents accurately on a global basis. However, within this area there is considerable room for advancement in the techniques used to measure ozone from a satellite platform.

The Canadian instrument OSIRIS onboard the Swedish-led satellite Odin contains an optical spectrograph that is used for measuring limb radiance in the atmosphere. There are various proven techniques to convert limb radiance data into ozone density profiles. This work presents a new technique that combines radiance data from both the Chappuis and Hartley-Huggins bands to retrieve ozone density. The new technique extends the current upper limit of Chappuis-only retrievals from 40 km to 60 km.

The major portion of this work describes the implementation of this new technique. Briefly, a Multiplicative Algebraic Reconstructive Technique, together with the SaskTRAN radiative transfer model, is used to invert the limb radiance data into ozone density profiles.

An overview of the resulting ozone density profiles is presented together with comparisons against other ozone products as a first order verification of the results.

This work will be used to produce a new ozone data set from the OSIRIS limb radiance data consisting of ozone density profiles that are valid to 60 km.

Acknowledgements

My first thanks goes to the Institute of Space and Atmospheric Studies for the opportunity to study as a member of this institute and a student of the University of Saskatchewan. Further thanks are due to both the Institute and the University for the financial support I received over the course of this degree.

Thanks to fellow students Michael Stoicescu and Truitt Wiensz for their support and friendship. Special thanks to PhD student Adam Bourassa for being my daily sounding board, and for his friendship.

Thanks to OSIRIS flight director Dr. Nick Lloyd for asking hard questions and his willingness to help.

Special thanks to my supervisors: Dr. Ted Llewellyn for his in-depth knowledge of atmospheric science and his oversight of the OSIRIS team; and Dr. Doug Degenstein for his commitment to this project, his ability to teach, and his encouragement to excel.

Final thanks go to my family for their constant love and support.

To Rebecca Roth, my wife.

Contents

List of Tables

List of Figures

Glossary of Terms

CVT	Chappuis Vector Triplet
HVP	Hartley-Huggins Vector Pair
MART	Multiplicative Algebraic Reconstructive Technique
OS	Optical Spectrograph
OSIRIS	Optical Spectrograph and InfraRed Imaging System
SAA	Solar Azimuth Angle
SaskTRAN	Radiative Transfer Model of the University of Saskatchewan
SaskMART	Saskatchewan Multiplicative Algebraic Reconstructive Technique
SZA	Solar Zenith Angle
UV	Ultraviolet

Chapter 1

Introduction and Background

The objective of this work is to retrieve vertical number density profiles of atmospheric ozone from radiance data collected by the Optical Spectrograph and InfraRed Imaging System (OSIRIS). The SaskTRAN radiative transfer model developed at the University of Saskatchewan and a new retrieval technique outlined in this work will be used to create an ozone database for the entire OSIRIS mission. The new retrieval technique is an inversion method that incorporates both Hartley-Huggins and Chappuis ozone absorption information.

1.1 Outline

This chapter presents the background material necessary to understanding the remainder of this work. An overview is given of relevant atmospheric physics concepts, ozone, the OSIRIS instrument, radiative transfer modelling (including SaskTRAN), inverse retrieval techniques, and the comparison data used in the remaining chapters.

The SaskMART retrieval technique is introduced in Chapter 2 and its ability to retrieve ozone profiles using information limited to the Chappuis band of the ozone cross section demonstrated. SaskMART retrievals are also compared to other ozone products with favourable results.

The finalized retrieval technique is presented in Chapter 3. Hartley-Huggins wavelength data is added to the SaskMART retrieval allowing the retrieval to be extended to higher altitudes. The results are compared with other validated ozone products and show general agreement. They demonstrate that the SaskMART retrieval method is capable of retrieving ozone density profiles up to 60 km.

Conclusions are presented in Chapter 4 together with global and polar ozone maps made with ozone profiles generated by the technique described in this work. Suggestions for future work are also discussed in the Conclusion.

1.2 Background

The following six topics are discussed in this chapter and provide the background material necessary for the remainder of this work:

- the atmosphere (§1.3)
- atmospheric ozone (§1.4 and §1.5),
- the OSIRIS instrument and its measurements (§1.6),
- atmospheric radiative transfer modelling (§1.7) and SaskTRAN specifically (§1.8),
- retrieval theory (§1.9), especially the Multiplicative Algebraic Reconstructive Technique (§1.9.4), and
- comparison ozone products (§1.10).

1.3 Atmospheric Fundamentals

The Earth's atmosphere has two basic components that constitute ∼99% of the mass: molecular nitrogen (N_2) and molecular oxygen (O_2). The remaining ∼1% of the atmosphere is made up of many different gases; however, despite their relatively low abundance, these gases have a significant impact on the atmosphere. Carbon dioxide (CO_2), water vapour (H_2O), and ozone (O_3) are among the trace gases that are responsible for maintaining the temperature profile in the atmosphere between the ground and 60 km.

1.3.1 Temperature Profile

The temperature profile, Figure 1.1, divides the atmosphere into four distinct layers: the troposphere, stratosphere, mesosphere, and thermosphere. The *troposphere* begins at the ground and continues to 10–17 km. This layer is characterized by continuously decreasing temperatures, about 7°C per km. It is the most familiar region of the atmosphere, containing most of the weather and clouds. It is also the most dynamic of the layers, the air is turbulent and well mixed horizontally and vertically.

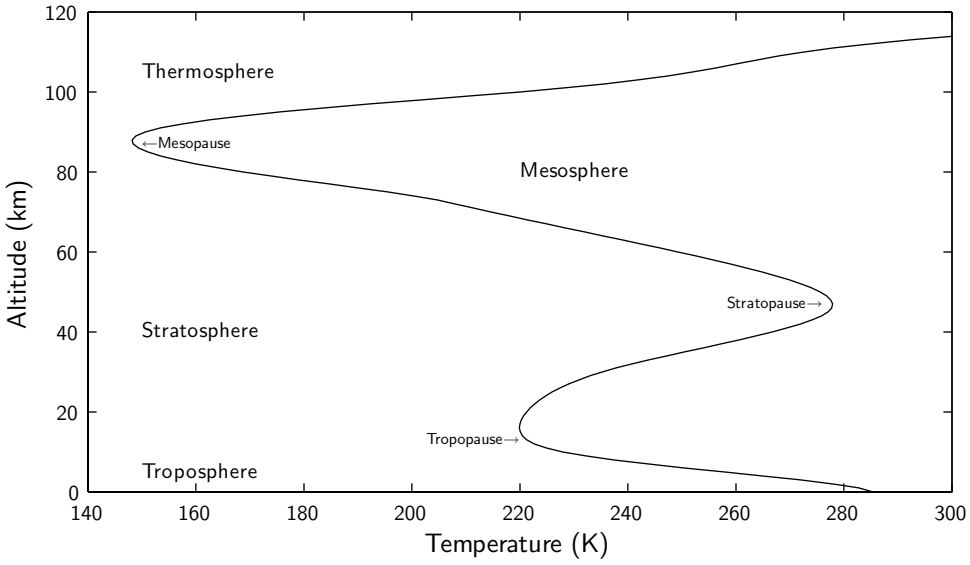

Figure 1.1: Average noontime temperature profile above Saskatoon, SK., June, 2005, illustrating the atmospheric layers. Data taken from MSISE-90 model courtesy NASA Goddard Space Flight Center.

The boundary between the troposphere and the stratosphere is the *tropopause.* The temperature increase in the *stratosphere* is due to the conversion of sunlight into heat, primarily through ozone absorption. Because of this temperature inversion, air in the stratosphere moves only slowly in the vertical direction (on the order of millimetres per second). The ozone absorption that is responsible for the temperature increase becomes negligible at higher altitudes creating a temperature peak at 45 km that marks the next boundary: the *stratopause.* In the *mesosphere* the temperature again drops at the rate of about 7°C per km until it begins to rise again in the thermosphere. The division between the mesosphere and the thermosphere is the *mesopause.* The *thermosphere* is the "top" of the atmosphere. Short-wave radiation ionizes the outermost part of the atmosphere adding heat to this layer. That heat is spread throughout the region establishing the temperature gradient seen at the top of Figure 1.1.

1.3.2 Pressure Profile

Temperature is not the only property of the atmosphere that varies with height. The rate at which the atmospheric pressure decreases with height is the pressure *scale height* where for each scale height in an isothermal atmosphere the pressure drops by

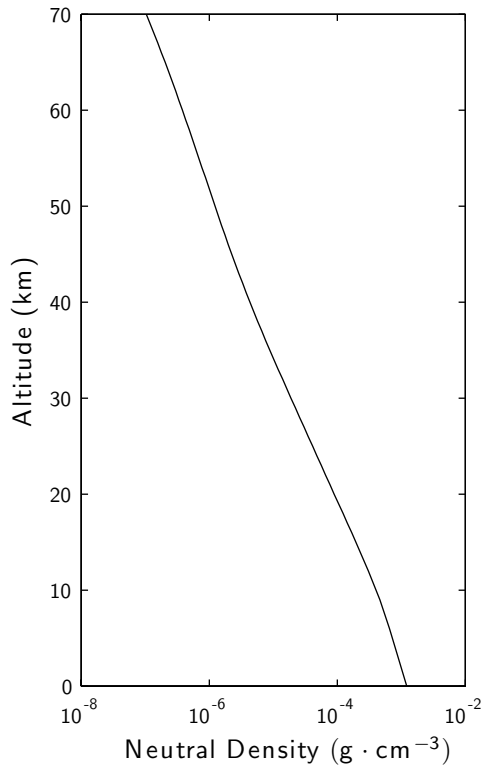

Figure 1.2: Average noontime neutral density profile taken from MSISE-90 model above Saskatoon, SK., June, 2005.

a factor of e. This is a direct result of hydrostatic balance that leads to the pressure gradient equation:

$$\nabla p = \rho \boldsymbol{g}, \tag{1.1}$$

where p is pressure, ρ is mass density, and $\boldsymbol{g}$ is gravitational acceleration. The solution of the pressure gradient equation leads to a typical scale height of 7.4 km throughout the lowest 100 km. This means that 90% of the atmospheric mass is in the troposphere and only 10% in the stratosphere. Figure 1.2 is a sample plot of the neutral density.

1.3.3 Light Absorption

Energy is added to the atmosphere through the absorption of radiation. This same absorption can also be used to infer information about the species that attenuate the light. When a photon travels through a gaseous medium there is a non-zero probability that it will interact with the medium and be absorbed. A *cross section,* $\sigma[cm^2]$, is the measurement that quantitatively describes the extinction rate of photons as they

interact with the absorber. The relationship between the extinction rate and cross section is given by:

$$q = n\sigma \qquad [\mathrm{cm}^{-1}], \tag{1.2}$$

where q is the extinction rate per unit length and n is the number density of absorbers in the medium. Integrating the R.H.S. of Equation 1.2 over a distance through the medium gives

$$\tau = \int_0^z n(z')\sigma \mathrm{d}z', \tag{1.3}$$

where τ is the optical depth of the medium and z is the distance through the medium.

Consider a beam of photons with intensity I. The interaction of the photons with the medium results in a decrease in the intensity of the beam. This is known as Beer's Law,

$$\begin{aligned} -\mathrm{d}I &= In\sigma \mathrm{d}z \\ -\mathrm{d}I &= I\mathrm{d}\tau. \end{aligned} \tag{1.4}$$

Integrating Equation 1.4 leads to

$$I(z) = I_0 e^{-\tau}, \tag{1.5}$$

where I_0 is the incident beam intensity.

The cross section is a property of the absorber and varies with wavelength, λ. Wavelengths with a smaller cross section have a smaller optical depth for the same path and the atmosphere is more transparent at those wavelengths. It is the decrease in photon intensity that both heats the atmosphere and provides an observable feature.

1.4 Ozone

The majority of atmospheric ozone is located above the troposphere and protects life on Earth by shielding it from ultraviolet (UV) radiation. Without ozone, the surface of the Earth would be bathed in UV radiation, which is harmful to eyes and skin as well as being able to break DNA molecular bonds. Recent anthropogenic chemical additions to the atmosphere can destroy ozone so that measurement of the atmospheric ozone column became the subject of worldwide interest and debate (*Cicerone*, 1974; *Molina and Rowland*, 1974). Research has shown that stratospheric

ozone concentrations have declined over the past three or four decades (*Wayne*, 2000). However, there has been some recent speculation that the ozone loss rate is decreasing due to conformity with the Montreal Protocol that mandated the removal of ozone depleting substances (*Weatherhead et al.*, 2000; *Newchurch et al.*, 2003).

1.4.1 Ozone Absorption

After the initial discovery of ozone by *Schönbein* (1840) in a laboratory and the subsequent tropospheric discovery by *Houzeau* (1858), Hartley made a spectroscopic study that showed ozone has absorption features in both the visible and ultraviolet regions (*Hartley*, 1881b,a); his work was validated a year later by *Chappuis* (1882).

As previously noted, ozone filters out most of the solar radiation in the ultraviolet range. The UV portion of the ozone cross section, also known as the Hartley continuum and the Hartley-Huggins bands, begins and ends around 200 and 300 nm. The absorption feature in the visible, known as the Chappuis band, absorbs wavelengths between 500 and 700 nm. The weak absorption at wavelengths beyond 700 nm is due to the Wulf bands. The absorption in the Hartley-Huggins region is much stronger than the absorption in the Chappuis band. Figure 1.3 is a plot of the absorption of the two bands as a function of wavelength. Figure 1.4 is a plot of the absorption of the solar spectrum by a typical ozone column. This figure clearly demonstrates the absorption cross section in the two regions, especially the Hartley-Huggins bands. As most of the ozone in the atmosphere resides in the stratosphere, it is in this region that the conversion of UV-light into heat energy is dominant.

1.4.2 Ozone Chemistry

The first theoretical description of the ozone layer was given by *Chapman* (1930). He developed a steady-state photochemical model based on oxygen-only reactions. Combining the Chapman reaction scheme with insights from the last seventy years produces the following reactions:

$$O_2 + h\nu \rightarrow O + O \tag{1.6a}$$

$$O + O_2 + M \rightarrow O_3 + M \tag{1.6b}$$

$$O_3 + h\nu \rightarrow O_2 + O \tag{1.6c}$$

$$O_3 + O \rightarrow O_2 + O_2 \tag{1.6d}$$

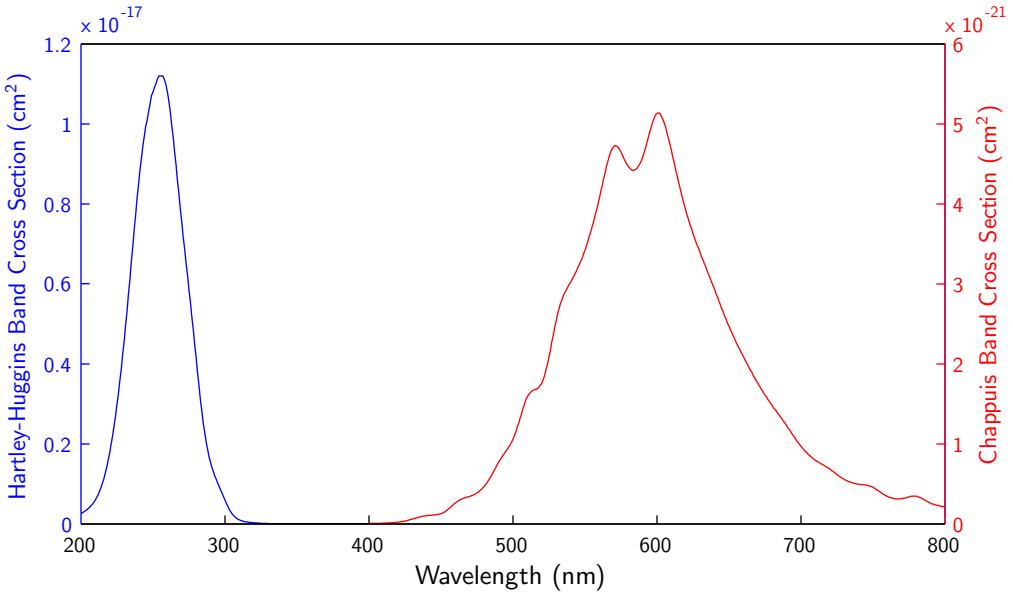

Figure 1.3: Cross section of ozone by wavelength. Note the different scales for the Hartley-Huggins and Chappuis bands.

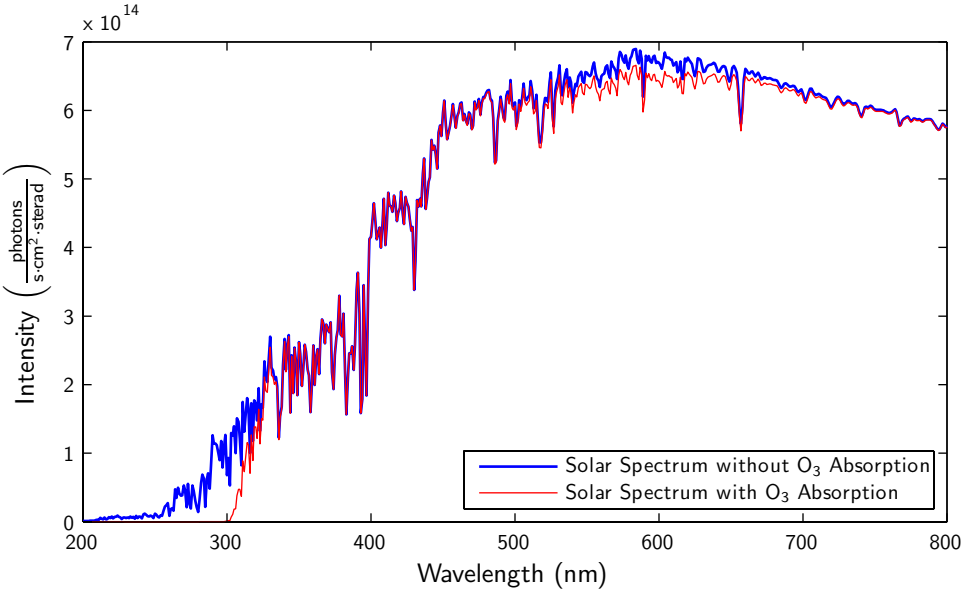

Figure 1.4: Calculated solar spectrum intensity before and after travelling through a standard atmospheric amount of O_3.

$$O_3 + O_3 \rightarrow O_2 + O_2 + O_2 \tag{1.6e}$$

$$O + O + M \rightarrow O_2 + M \tag{1.6f}$$

Because Reaction 1.6b is very efficient at converting O back into O_3, it is the sum of [O] and [O_3] (where the brackets denote concentration) that is important and not just the O_3 concentration. The combination of O and O_3 is known as *odd oxygen.* Reactions 1.6a, 1.6b, and 1.6c provide the mechanism for converting UV-light into heat.

The reactions in (1.6) can be divided into three groups: those that produce odd oxygen, Reaction 1.6a; those that balance the ratio of O and O_3 concentrations, Reactions 1.6b and 1.6c; and those that destroy odd oxygen, Reactions 1.6d, 1.6e, and 1.6f. However, due to the low concentration of O in the stratosphere, Reaction 1.6f is too slow in comparison with Reactions 1.6d and 1.6e to make a measurable difference and can be neglected.

Summing Reaction 1.6a and Reaction 1.6b we have:

$$\begin{aligned} O_2 + h\nu &\rightarrow 2O \\ \underline{2O + 2O_2 + 2M \rightarrow 2O_3 + 2M}&\,, \\ 3O_2 + h\nu &\rightarrow 2O_3 \end{aligned} \tag{1.7}$$

which describes the production mechanism for O_3.

After sunset, when Reaction 1.6c stops but Reaction 1.6b remains, the concentration of O drops rapidly. The rate of Reaction 1.6b decreases with increasing altitude so that the ratio [O_3]/[O] is higher at lower latitudes.

The odd oxygen reactions provide a basic foundation for understanding the sources and sinks of odd oxygen but do not give the complete story. The measured rate of Reaction 1.6d is much smaller than that required by the oxygen only model. However, *Bates and Nicolet* (1950) showed the rate of Reaction 1.6d is significantly increased in the presence of a catalyst. An example of a catalytic cycle that increases the rate of Reaction 1.6d is:

$$\begin{aligned} Cl + O_3 &\rightarrow ClO + O_2 \\ \underline{ClO + O \rightarrow Cl + O_2}& \\ O_3 + O &\rightarrow O_2 + O_2 \end{aligned} \tag{1.8}$$

Other catalytic cycles also increase the rate of Reaction 1.6e. One such example is:

$$\begin{aligned} \mathrm{OH} + \mathrm{O_3} &\rightarrow \mathrm{HO_2} + \mathrm{O_2} \\ \underline{\mathrm{HO_2} + \mathrm{O_3} \rightarrow \mathrm{OH} + \mathrm{O_2} + \mathrm{O_2}} \\ \mathrm{O_3} + \mathrm{O_3} &\rightarrow \mathrm{O_2} + \mathrm{O_2} + \mathrm{O_2} \end{aligned} \tag{1.9}$$

1.4.3 Chapman Layers

The existence of a layer-like structure is expected for any species whose concentration depends on photochemical production in an atmosphere of varying optical depth. These layers are known as *Chapman layers* and have a profile defined by the Chapman function. Because odd oxygen is produced photochemically, its shape closely matches the Chapman function.

The Chapman layer shape can be qualitatively understood by a simple model in which incident radiation travels downward from the top of the atmosphere. As light travels through the atmosphere it interacts with the medium and so decreases in intensity. The lower the altitude the light reaches, the denser the background atmosphere and so more absorption. At a certain point, all of the incident radiation has been absorbed leaving no more radiation available for absorption and a layer is expected. As the dominant mechanism for ozone production is Reaction 1.6a, a Chapman layer is expected.

Following *Wayne* (2000), a simple derivation of the Chapman function is given below. The isothermal derivation begins by noting that the background atmospheric number density, n, can be written as

$$n = n_0 e^{-z/H}, \tag{1.10}$$

where n_0 is the reference number density, z is the altitude above the reference, and H is the scale height of the atmosphere. The optical absorption of the atmosphere was given in Equation 1.4. If we assume a plane parallel atmosphere, then for an increase in altitude, $\mathrm{d}z$, the path length to the Sun has decreased by $\sec\theta \mathrm{d}z$, where θ is the solar zenith angle (see Figure 1.5). Equation 1.4 then becomes

$$\mathrm{d}I = In\sigma \sec\theta \mathrm{d}z. \tag{1.11}$$

Combining Equation 1.10 and Equation 1.11 and integrating yields

$$I = I_\infty \exp(-n_0 \sigma H \sec\theta e^{-z/H}) \tag{1.12}$$

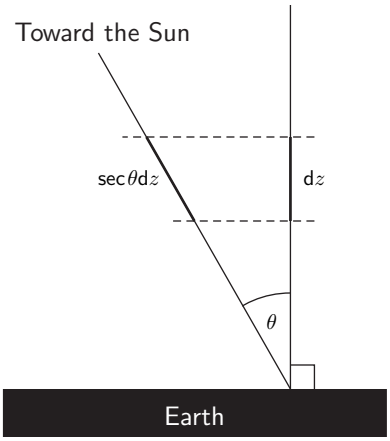

Figure 1.5: The path length to the sun increases by $\sec\theta \mathrm{d}z$ as the altitude increases by $\mathrm{d}z$.

where I_∞ is the light intensity at $z = \infty$, which is just the incoming radiation from the sun. The rate, q, at which energy is removed from the incoming radiation per unit length is given by:

$$q = \mathrm{d}I_z/(\sec\theta \mathrm{d}z)$$
$$q = I_\infty n_0 \sigma \cos\theta \exp\left(-\frac{z}{H} - n_0 \sigma H \sec\theta e^{-z/H} \right) \tag{1.13}$$

The maximum of rate of Equation 1.13 corresponds to the peak in the Chapman layer.

The peak height of O_2 photodissociation caused by photons around 220 nm (in the O_2 Herzberg band), is in the stratosphere; hence, it is here that the greatest concentration of odd oxygen, and therefore ozone, is found (*Wayne*, 2000). Figure 1.6 is a sketch of the Chapman function. The altitude units are arbitrary.

Although Chapman layer chemistry neglects the other processes responsible for the distribution of ozone throughout the atmosphere, it still explains the typical ozone profile that can be seen all over the globe.

1.5 Previous Ozone Study

Ever since the importance of atmospheric ozone was recognized, measurements of atmospheric ozone have been made around the globe in order to understand the behavior of the ozone layer and, more recently, its depletion. Ground based instruments

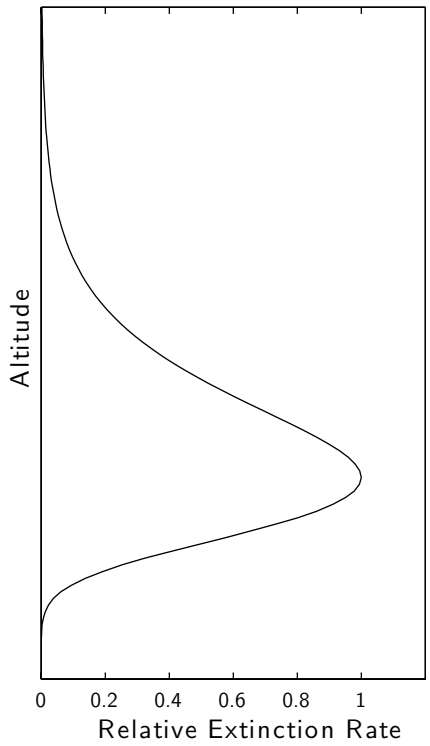

Figure 1.6: Sketch of the Chapman function using Equation 1.13 with arbitrary altitude. The sketch shows that the extinction rate increases (from top to bottom) until it reaches a maximum and then quickly drops to zero.

were first used to monitor ozone and later balloon and satellite borne instruments have provided measurements.

1.5.1 Ground Based

While studying meteors at Oxford, *Lindemann and Dobson* (1923) discovered that the temperature of the stratosphere increased with altitude. They concluded that the governing process in the stratosphere must be radiative and that the temperature inversion was due to UV radiation being converted into heat through ozone absorption; the prediction made by *Hartley* (1881a) decades earlier was confirmed.

This discovery prompted an increase in ground based research into atmospheric ozone. One of the first instruments used to measure ozone was the Dobson spectrophotometer developed in 1924. This device observed the Hartley-Huggins bands of the spectrum and from measurements of the absoption inferred the amount of ozone in a vertical column above the instrument. Brewer spectrophotometers, based on the Dobson instrument, are presently used to measure the ozone vertical column.

1.5.2 Balloon

Balloon borne ozone sondes are instruments that measure the partial pressure of ozone and total atmospheric pressure as they rise through the atmosphere. The ozone density profile is mapped until the balloon fails at around 30–35 km. Because of their ability to make direct measurements, ozone sondes are an accurate instrument for the measurement of ozone in the atmosphere.

1.5.3 Satellite Based

There are a number of different ways to measure ozone from a satellite platform, each with its own advantages and disadvantages (see Table 1.1).

The first satellite based instrument to measure atmospheric ozone columns was the Total Ozone Mapping Spectrometer (TOMS) onboard NASA's Nimbus-7 satellite (*Heath et al.*, 1975). TOMS began collecting data in 1978 and remained active onboard Nimbus-7 until 1993. Other versions of the TOMS instrument have been launched on NASA's Earth Probe, Meteor-3 and OMI satellites, so providing continued global coverage from 1978 to the present. Analysis of TOMS data over that period showed a clear reduction in total global ozone. As the TOMS instrument only measures the total ozone columns many other instruments have been designed to determine the vertical ozone density profile.

Another instrument that measures total ozone columns is the Global Ozone Monitoring Experiment (GOME) on board European Space Agency's ERS-2 (*Burrows et al.*, 1999).

NASA's Stratospheric Aerosol and Gas Experiment (SAGE) satellites measure ozone (*McCormick et al.*, 1989, 1991). SAGE II and SAGE III primarily retrieve ozone by occultation, *i.e.*, they observe the sun rising or setting and determine the amount of ozone in the atmospheric limb by measuring the amount of absorption. Occultation is necessarily restricted to two measurements per orbit as scans can only be made when the instrument observes the sun ascending or descending through the limb. SAGE III also uses limb scattered light (*Rault*, 2004, 2005) but this does not yet yield a primary product.

The Atmospheric Chemistry Experiment (ACE) onboard SCISAT-1, a Canadian satellite, is another instrument that measures ozone density profiles via solar occultation (*Bernath et al.*, 2005). The Polar Ozone and Aerosol Measurement III

(POAM III) instrument developed by the United State's Naval Research Laboratory on board SPOT-4 (*Lucke et al.*, 1999) and NASA's Halogen Occultation Experiment (HALOE) instrument on board the Upper Atmosphere Research Satellite (UARS) (*Russell et al.*, 1993) are two more ozone profilers.

The European Space Agency's satellite Envisat contains the Scanning Imaging Absorption Spectrometer for Atmospheric Chartography (SCIAMACHY) instrument that retrieves ozone from measurements of limb scattered light (*Bovensmann et al.*, 1999).

The first use of limb scattered light to retrieve ozone density profiles was with the Ultraviolet Spectrometer (UVS) on the Solar Mesosphere Explorer (SME) satellite (*Rusch et al.*, 1984). The Shuttle Ozone Limb Sounding Experiment/Limb Ozone Retrieval Experiment (SOLSE/LORE) instrument on NASA's space shuttle also used the limb scattered light technique (*McPeters et al.*, 2000).

Table 1.1 compares different ozone measuring instruments and their respective measurement techniques. Instruments that measure the total ozone density of a column have excellent global coverage, but no vertical resolution. Solar occultation instruments have excellent vertical resolution, but limited coverage. In contrast, instruments using the limb scattered technique have both excellent global coverage and good vertical resolution.

Table 1.1: Comparison of Different Satellite Instruments.

	Column	**Occultation**	**Limb Scattered**
		SAGE II	
	TOMS	SAGE III	SAGE III[a]
Examples	GOME	ACE	SCIAMCHY
		POAM	OSIRIS
		HALOE	
Coverage	Global, daily	Orbit Dependent[b]	Global[c], daily
Vertical Resolution	none	<2 km	<5 km

[a]Not a primary product.

[b]SAGE II and SAGE III cover only certain latitude bands. ACE has global coverage several times per year.

[c]Sunlit portion of the atmosphere only.

1.6 OSIRIS

The Optical Spectrograph and InfraRed Imaging System (OSIRIS) is a Canadian instrument onboard the Swedish Odin satellite launched on February 20, 2001 (*Murtagh et al.*, 2002). It was designed to measure limb scattered light from the atmosphere of the Earth in the visible and infrared spectral regions.

The Odin orbit was selected so that the instrumentation would view local dusk when travelling north and local dawn when travelling south, *i.e.*, it is in a sun-synchronous near-terminator orbit. The design parameters resulted in an orbit with an inclination of 98°, an orbital period of 96 minutes and near-global coverage (latitude range of 82°S to 82°N). The orbit path for each hemisphere is illuminated during summer and dark during winter; solar zenith angles range from 60–120°. Twice yearly, near equinox, the orbit path is along the terminator. During these terminator orbits the solar zenith angle remains close to 90° at all points along the orbit. An overview of OSIRIS can be found in *Llewellyn et al.* (2004).

1.6.1 The Optical Spectrograph

The Optical Spectrograph, scans the limb of the atmosphere and spectrally dispersed radiance data is collected with approximately 1 nm resolution over a wavelength range of 280–810 nm. As the Odin satellite orbits the Earth, the spectrograph records the spectrum approximately once every two seconds. It nods up and down so that its line of sight scans tangent altitudes between 10 and 100 km. A complete scan of about 50 individual tangent altitude exposures is shown in Figure 1.7. There are approximately 60 scans in each orbit. Certain ozone features are readily apparent in a comparison of the normalized spectra from 15 and 40 km (Figure 1.8). These spectra are normalized at 480 nm and show the strong absorption in the Hartley-Huggins region and the weaker absorption in the Chappuis region. The data gap from 480 to 530 nm is due to a spectral order sorter in front of the CCD.

1.7 Radiative Transfer Modelling

Information about atmospheric constituents is contained in the outgoing solar ultraviolet, visible, and infrared light from the atmosphere of the Earth. The satellite experiments outlined in § 1.5.3 all convert measurements of this light into ozone measure-

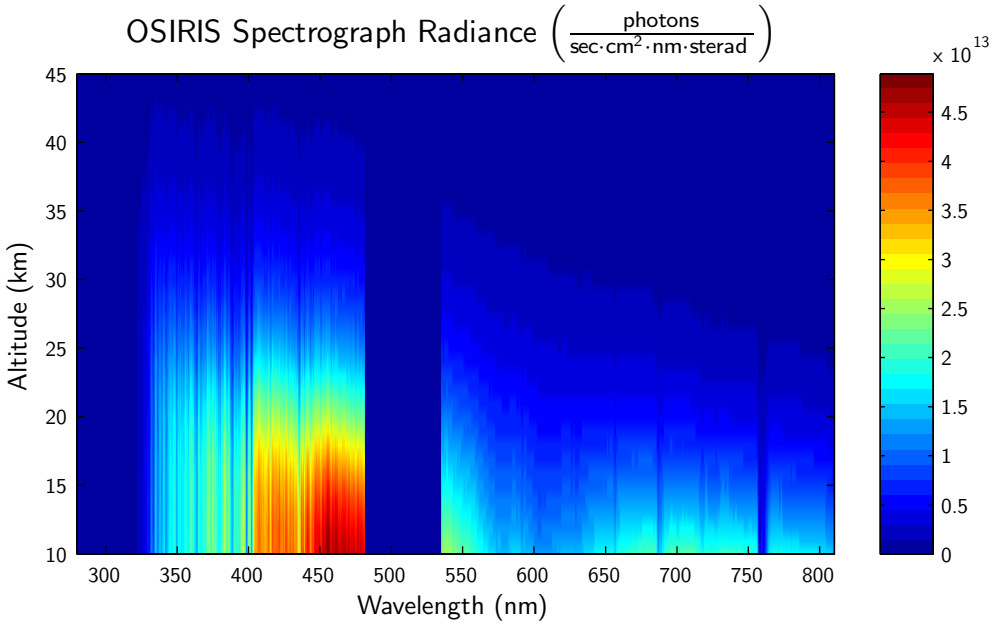

Figure 1.7: Typical OSIRIS Spectrograph scan (Orbit 6432, Scan 12). The data was collected during a 90 second time period.

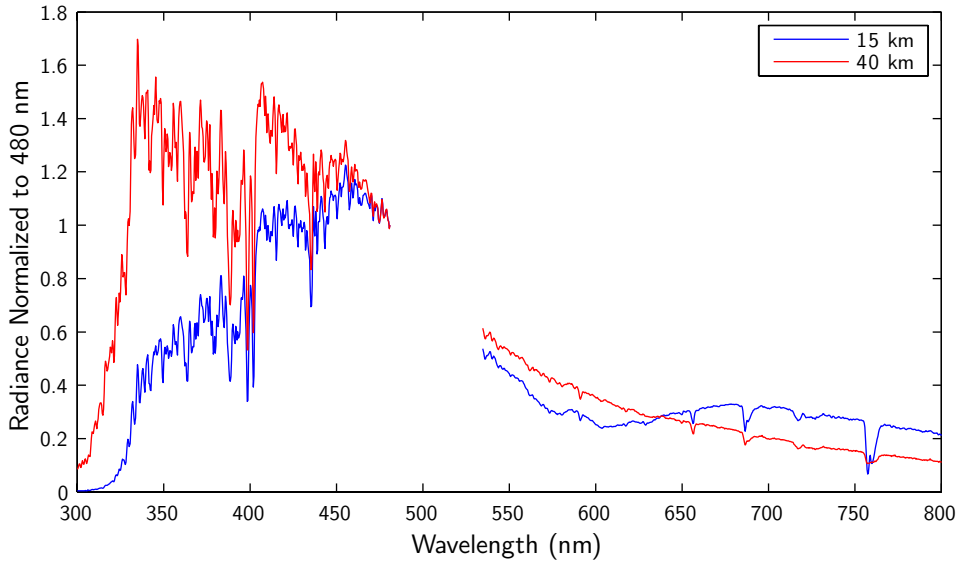

Figure 1.8: Comparison of normalized 15 and 40 km radiance data from Figure 1.7. The dip around 600 nm in the 15 km line is due to the Chappuis portion of ozone absorption. Strong absorption also takes place around 300 nm in the 15 km line due to the Hartley-Huggins bands. The radiance from 15 km contains relatively less blue light and relatively more red light (due to Rayleigh scattering).

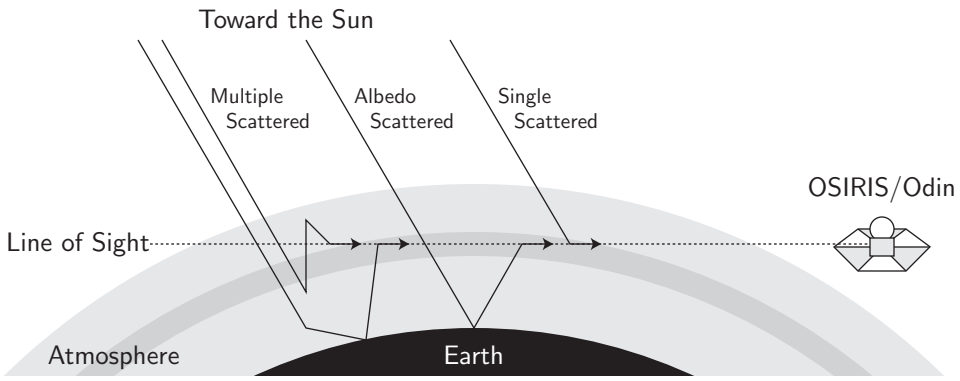

Figure 1.9: The different scattering mechanisms. Most of the radiance data comes from the shaded tangent height region. This figure shows the radiance from the sun coming in from the upper left in order to illustrate the scattering mechanisms; however, for the OSIRIS orbital geometry, the solar rays would be coming from a direction approximately perpendicular to the page.

ments. This includes the instruments that rely on limb scattered light *e.g.,* OSIRIS. To do this conversion a model that calculates the wavelength dependent radiance as a function of satellite position and solar geometry, known as a radiative transfer model, is needed.

There are three main sources of light that can be modelled by radiative transfer: single scattered light, multiple scattered light and Earth or albedo scattered light (see Figure 1.9). Although single scattered light is the dominant source, the contributions of multiple scattered light and albedo scattered light are not negligible.

Modelling limb scattered light is complicated because, unlike nadir viewing geometries, the line of sight path lengths through the atmosphere are long and extend over distances that prohibit the reduction of the spherical Earth to a flat Earth model. Therefore, the curvature of the surface of the Earth must be taken into account in any limb scatter radiative transfer model. The path length, l, through any 1 km tangent layer at height, z, neglecting refractive bending, is

$$l = 2\sqrt{(z + R_e + 1\text{km})^2 - (z + R_e)^2}, \tag{1.14}$$

where R_e is the radius of the Earth. For the region of interest where z = 1–100 km, l is between 225 and 228 km for an Earth radius of 6378 km. However, despite the modelling difficulty, these long path lengths are the benefit of the tangential viewing geometry in that any change in the density of a given atmospheric constituent translates into a measurable change in the modelled limb radiances.

A number of radiative transfer models have been developed specifically to model limb scattered radiance including SaskTRAN, GSLS (*Flittner et al.*, 2000), LIMBTRAN (*Griffioen and Oikarinen*, 2000; *Sioris et al.*, 2003; *von Savigny et al.*, 2003; *Haley et al.*, 2004), and VECTOR (*McLinden et al.*, 2002). There are other radiative transfer models not specifically developed for a limb viewing geometry that can be used to model limb scattered light including CDI (*Rozanov et al.*, 2000), and SIRO (*Oikarinen et al.*, 1999; *Oikarinen*, 2001, 2002). Comparisons between the models mentioned above and other models have been made by *Griffioen and Oikarinen* (2000), *McLinden et al.* (2002), and *Loughman et al.* (2004). Additional comparisons have been made for SaskTRAN. The results show good agreement between SaskTRAN and the other models (*Bourassa et al.*, 2007).

A brief description of the various types of radiative transfer models is given below in order to provide the foundation for the discussion of SaskTRAN.

1.7.1 Pseudo-Spherical

Pseudo-spherical limb radiance radiative transfer models combine a series of independent plane-parallel radiative transfer models to approximate a spherical radiative transfer model. Different points along the line of sight are assigned different weights according to their respective geometry. The single scatter and multiple scatter contributions are integrated along the line of sight, over the various models. Pseudo-spherical models are capable of accounting for the albedo of the Earth.

The advantage to pseudo-spherical models is their simplicity and computational speed; the disadvantage is the lack of accuracy inherent in the assumptions.

LIMBTRAN (*Griffioen and Oikarinen*, 2000), and CDI (*Rozanov et al.*, 2000) are two examples of Pseudo-spherical radiative transfer models.

1.7.2 Spherical

Spherical models take the curvature of the atmosphere into account when calculating the limb radiances. That is, the properties relating to each point along the line of sight, *e.g.,* path length, SZA, *etc.*, are based on a the curvature of the Earth. Because spherical models do not make simplifications for the curvature of the Earth, the calculation time increases over pseudo-spherical models; however, the accuracy of the model also increases.

GSLS (*Herman et al.*, 1994) and SaskTRAN (*Bourassa et al.*, 2007) are spherical radiative transfer models.

1.7.3 Statistical

Statistical radiative transfer models are Monte Carlo simulations that determine the limb radiance. The basis is this: many photons are tracked backwards from their end position, *i.e.*, the satellite in space, and scattered through the atmosphere to their end trajectories in space, *i.e.* toward the sun. This technique relies on the fact that a probability can be assigned to each scattering event a photon has in the atmosphere and that these probabilities can be integrated over a large number of trial photons to simulate the physical radiative transfer process.

Although this technique is arguably the most accurate, the disadvantage is the amount of computer time required. The statistical noise varies inversely with the number of trial photons. Therefore, to get a statistically meaningful result many photons must be traced.

SIRO (*Oikarinen et al.*, 1999; *Oikarinen*, 2001, 2002) is a radiative transfer model based on the statistical technique.

In terms of accuracy, the statistical models provide the best answer; however, they also require the most computational resources. The spherical models are typically within two or three percent of the statistical models, whereas the pseudo-spherical models can be systematically off by as much as ten percent (*Loughman et al.*, 2004).

1.8 SaskTRAN

An atmospheric radiative transfer model is required to derive the ozone number densities from the OSIRIS measurements. The radiative transfer model used for this work is SaskTRAN, which is computer code developed and written by our group for the specific limb viewing geometry of the OSIRIS instrument. This model uses the equations outlined in Section 1.3.3 to calculate the amount of radiation that should be seen by OSIRIS at a given location and viewing angle.

SaskTRAN allows the user to set various parameters that determine the accuracy of the modelled radiance, these include:

- the neutral density profile,
- the ozone density profile,

- the background stratospheric aerosol profile,
- the background NO_2 profile,
- the Earth albedo, and
- the number of multiple scattering orders (two orders are shown in Figure 1.9).

The modelled results of SaskTRAN agree well with data collected by OSIRIS as well as the results from other radiative transfer models such as LIMBTRAN.

1.9 Retrieval Theory, an Inversion Process

In this section, a general overview of retrieval theory is given (§1.9.1), followed by a survey of various retrieval methods:

- Optimal Estimation (§1.9.2)
- Chahine Relaxation (§1.9.3), and
- Weighted Multiplicative Algebraic Relaxation (§1.9.4)

The final technique, Weighted Multiplicative Algebraic Relaxation, is the technique used in the present research.

1.9.1 The Measurements and the Model

The calculation of the ozone density in the atmosphere from limb scattered light measurements is an inverse process. An initial ozone density profile is assumed and the limb radiance is calculated with SaskTRAN. The differences between SaskTRAN and the OSIRIS measurements provide the feedback that is used to modify the ozone profile in order to simulate a new result that more closely matches the observation. The result is a retrieved ozone density profile.

Following *Rodgers* (2000), the m measurements are given by the vector, $\mathbf{y}$. The unknown atmospheric parameter is called the *state vector,* $\mathbf{x}$, with values at n locations. For this work the n locations are adjacent altitudes. The model, or system of equations, that represents the physical process that describes how the measurements result from the atmospheric parameters is called the *forward model,* $\mathbf{A}$. The measurement vector relates to the state vector and the forward model through

$$\mathbf{y} = \mathbf{A}(\mathbf{x}). \tag{1.15}$$

For a known set of measurements, $\mathbf{y}$, (*e.g.,* the limb scattered brightnesses), the unknown state vector (*e.g.,* the ozone density profile) that satisfies Equation 1.15

must be determined. Two factors can lead to errors in the result: first, there are limitations in how well the model represents reality, and second, the measurement vector itself may contain error.

A Taylor expansion of Equation 1.15 gives

$$\mathbf{y} = \mathbf{A}(\mathbf{x}_0) + \frac{\partial \mathbf{A}(\mathbf{x}_0)}{\partial \mathbf{x}}\Delta\mathbf{x} + \frac{1}{2}\frac{\partial^2 \mathbf{A}(\mathbf{x}_0)}{\partial \mathbf{x}^2}\Delta\mathbf{x}^2 + \sum_{n=3}^{\infty}\frac{1}{n!}\frac{\partial^n \mathbf{A}(\mathbf{x}_0)}{\partial \mathbf{x}^n}\Delta\mathbf{x}^n, \tag{1.16}$$

which is an exact representation of $\mathbf{A}$, although it requires an absolute knowledge of the forward model and an infinite number of terms. As a necessary compromise, the forward model can be represented by a system of partial derivatives with respect to each element of the state vector. This is known as a weighting function matrix or kernel, $\mathbf{K}$, and is of size $m \times n$ — a derivative at each point in the model, A_j, for each point in the state parameter, x_i.

$$\mathbf{K} = \frac{\partial \mathbf{A}(\mathbf{x})}{\partial \mathbf{x}}. \tag{1.17}$$

If the model is linear and the measurements contain no error, $\mathbf{K}$ is an exact representation of $\mathbf{A}$, *i.e.*,

$$\mathbf{y} = \mathbf{K}\mathbf{x}. \tag{1.18}$$

If this is the case, then the solution to the unknown state vector can be found through the inversion of $\mathbf{K}$.

However, many models (including the SaskTRAN radiative transfer model discussed here) are non-linear and because all measurements contain some error, $\mathbf{K}$ is an inadequate representation of $\mathbf{A}$. There are a number of different techniques available that attempt to find the state parameters that best match the observations. These methods use *a priori* constraints to reach the solution. Some of these constraints are:

- an expected solution, *e.g.,* a climatological guess,
- a discreet solution with fewer points than the number of measurements, and
- solution smoothness.

1.9.2 Optimal Estimation

The primary technique used in atmospheric studies is the statistical method of *Optimal Estimation* (*Rodgers*, 1976, 2000). This technique uses *a priori* climatological information to provide the initial state parameters. The final solution of the state parameters is constrained by this *a priori* to be within its given error. Because of

this, it is important that the provided climatological information be as accurate as possible but that it include an uncertainty that will encompass all probable solutions. The benefit of using this *a priori* is that it reduces the noise in the solution. Rodgers terms the climatological *a priori* estimate the *virtual measurement.* An overview of this technique follows.

In Gaussian statistics, the weighted average of two independent scalar measurements, x_1 and x_2, is found using their standard deviations as weights. That is,

$$\bar{x} = \left(\frac{1}{\sigma_1^2} + \frac{1}{\sigma_2^2}\right)^{-1} \left(\frac{x_1}{\sigma_1^2} + \frac{x_2}{\sigma_2^2}\right). \tag{1.19}$$

The variance of $\bar{x}$ is

$$\bar{\sigma}^2 = \left(\frac{1}{\sigma_1^2} + \frac{1}{\sigma_2^2}\right)^{-1}. \tag{1.20}$$

The weighted average of two vectors, $\mathbf{x}_1$ and $\mathbf{x}_2$, with error covariance matrices, $\mathbf{S}_1$ and $\mathbf{S}_2$, is found in a similar fashion:

$$\bar{\mathbf{x}} = \left(\mathbf{S}_1^{-1} + \mathbf{S}_2^{-1}\right)^{-1} \left(\mathbf{S}_1^{-1}\mathbf{x}_1 + \mathbf{S}_2^{-1}\mathbf{x}_2\right) \tag{1.21}$$

The variance of $\bar{\mathbf{x}}$ is

$$\bar{\mathbf{S}} = \left(\mathbf{S}_1^{-1} + \mathbf{S}_2^{-1}\right)^{-1}. \tag{1.22}$$

In terms of an atmospheric retrieval, for a linear problem with Gaussian statistics, the *a priori* or virtual profile, $\mathbf{x}_0$, with covariance matrix, $\mathbf{S}_0$ is combined with the observations $\mathbf{y} = \mathbf{K}\mathbf{x}$ and observation error covariance, $\mathbf{S}_e$, as in Equation 1.21:

$$\bar{\mathbf{x}} = \left(\mathbf{S}_0^{-1} + \mathbf{K}^T\mathbf{S}_e^{-1}\mathbf{K}\right)^{-1} \left(\mathbf{S}_0^{-1}\mathbf{x}_0 + \mathbf{K}^T\mathbf{S}_e^{-1}\mathbf{y}\right) \tag{1.23}$$

Non-linear problems solved by Optimal Estimation require Newtonian Iteration and a linear representation of the model. The linear representation is found by taking the Taylor series expansion about the current best guess of the state vector, $\mathbf{x}^{(n)}$.

$$\mathbf{y} = \mathbf{A}(\mathbf{x}^{(n)}) + \frac{\partial \mathbf{A}}{\partial \mathbf{x}}(\mathbf{x} - \mathbf{x}^{(n)}) \tag{1.24}$$

Using Equation 1.17, this becomes

$$\mathbf{K}\mathbf{x} = \mathbf{y} - \mathbf{y}^{(n)} + \mathbf{K}\mathbf{x}^{(n)}. \tag{1.25}$$

The required iterative equation is

$$\mathbf{x}^{(n+1)} = \mathbf{x}_0 + \left(\mathbf{S}_0^{-1} + \mathbf{K}^T\mathbf{S}_e^{-1}\mathbf{K}\right)^{-1} \mathbf{K}^T\mathbf{S}^{-1}[(\mathbf{y} - \mathbf{y}^{(n)}) - \mathbf{K}(\mathbf{x}_0 - \mathbf{x}^{(n)})]. \tag{1.26}$$

As the weighting function **K** changes with each iteration it must be recalculated each time, from the Taylor series, using the current state vector.

Optimal Estimation has become a mainstay in atmospheric studies due to its ease of implementation and because its solutions almost always appear reasonable as they can not depart further than the error in the *a priori.* The disadvantages of Optimal Estimation are that the *a priori* is unlikely to be normally distributed about the solution and the assumed Gaussian errors may not reflect reality.

1.9.3 Chahine Relaxation

Chahine Relaxation (*Chahine*, 1970, 1972) is another iterative solution to non-linear problems. It uses a discrete number of state parameters that correspond to the maxima of strongly peaked weighting functions such that the number of elements in the state vector, n, equals the number of elements in the observation vector, m. For atmospheric problems, the retrieval of atmospheric state parameters occurs at the altitudes where the individual measurements are most sensitive.

The iteration equation modifies each element, i, of the state vector by the ratio of the corresponding measurement vector element, $j = i$, to the current computation of the forward model. That is,

$$x_i^{(n+1)} = x_i^{(n)} \frac{y_i}{A_i(\mathbf{x}^{(n)})}. \tag{1.27}$$

In other words, the next iteration of x_i is multiplied by the ratio of the measurement to forward model at i. This is a form of Multiplicative Algebraic Reconstruction Technique (MART). In theory this produces the desired effect of converging on the "best" state parameters. The iterative process is repeated until the residuals, R_i, converge to within some error, ϵ, that reflects the measurement error, *i.e.*,

$$R_i = \left| \frac{y_i - A_i(x^{(n)})}{y_i} \right| \rightarrow \epsilon. \tag{1.28}$$

Chahine relaxation is straightforward to understand, easy to implement and provides stable results. The disadvantages are the limitations placed on the state parameter positions, an inability to incorporate extra measurements at the same altitude, and difficulty in estimating the error associated with **S**. As well, changes in one element of **S** are limited in their ability to propagate to other elements in **S** by the forward model only.

1.9.4 Weighted Multiplicative Algebraic Relaxation

The technique developed by Chahine assumes that there is a single observation for each altitude. If more than one observation occurs for a given altitude, the Chahine techniques is unable to include this additional information without doing the retrieval process separately for each observation set and then averaging the results — a definite short-coming of the Chahine technique.

A solution to this problem was developed for use with the OSIRIS tomographic volume emission rate retrievals at the University of Saskatchewan (*Degenstein*, 1999) as a modification of an existing Multiplicative Algebraic Reconstruction Technique. The main difference between this technique and that of Chahine is that multiple observation sets are integrated into the same system. This means that multiple elements in an observation vector can have an impact on the state parameter element as well as multiple observation vectors all having their "say." This allows information from multiple observations to be integrated into the same solution with each one having a given "say." Mathematically, as the relationship between each observation set, k, and the state vectors is different, each set is related through a unique forward model, A_k. The iteration equation is

$$x_i^{(n+1)} = x_i^{(n)} \sum_k \sum_j \frac{y_{jk}}{A_{jk}(\mathbf{x}^{(n)})} W_{ijk}. \tag{1.29}$$

The W_{ijk} terms make up the *weighting filter function* that relates the importance of the j^{th} element of the k^{th} observation set to the i^{th} element of the state parameter. The weighting filter function is made up of two independent sets of weights: the first relates the elements of an individual observation to each element of the state parameter, W_{ij}, and the second relates the importance of each observation as a whole to each element of the state parameter, W_{ik}. Each set of weights is normalized to unity, *i.e.*,

$$\sum_j W_{ij} = \sum_k W_{ik} = 1, \tag{1.30}$$

which means the joint weighting filter, W_{ijk} is also normalized to unity:

$$\sum_k \sum_j W_{ijk} = \sum_k \sum_j W_{ij} \cdot W_{ik} = 1. \tag{1.31}$$

The W_{ijk} terms must be chosen to reflect the relationship between observation sets, individual observation elements, and state vector elements. By incorporating

knowledge of the related physics and the forward model, an appropriate set of weights can be found. The simplest choice of weighting filter used with a single measurement set is $W_{ij} = \delta_{ij}$. If this W_{ij} is chosen with only one observation vector, *i.e.*, $W_{ik} = 1$ for only one k, this again reduces the technique to Chahine relaxation. The rationale for the weighting filter terms used in this work is discussed in Section 3.4.

1.10 Comparison Data

Sample sets of the ozone density profiles generated by the retrieval technique described in this work have been compared with other ozone products in order to validate the new technique. Specifically, the comparisons have been made for ozone products provided by SAGE II, SAGE III, and a previous OSIRIS ozone product. These three ozone products provide a reasonable base with which to compare the new retrievals.

1.10.1 OSIRIS Version 2.5

A detailed description of the method used for retrieving Version 2.5 ozone density profiles from the OSIRIS limb radiances is given by *von Savigny et al.* (2003). OSIRIS Version 2.5, also referred to as OSIRIS v.2.5, relies upon changes in the radiance of the Chappuis band to determine the amount of ozone in the atmosphere. Briefly, the retrieval algorithm is given below.

The first step is to normalize the wavelengths used in the retrieval to a tangent height of 50 km in order to reduce the sensitivity to albedo and to reduce instrument calibration effects (*von Savigny et al.*, 2003). Normalization to 50 km decreases the sensitivity to albedo because both the radiance at 50 km and the radiance below 50 km are affected the same way by an increase in Earth albedo. The same argument can be made for instrument calibration effects. For example, if the absolute calibration of the instrument is incorrect, it would affect the measurements at both altitudes in the same way, making the ratio insensitive to an error in absolute calibration.

Next, a retrieval vector is formed using three normalized Chappuis wavelengths — a reference wavelength from either side of the absorption band, and a wavelength from the ozone absorption peak. The retrieval vector is given by *von Savigny et al.* as:

$$y_C(TH_i) = \frac{I_n(\lambda_2, TH_i)}{\exp\left(\frac{1}{2}\big(\ln I_n(\lambda_1, TH_i) + \ln I_n(\lambda_3, TH_i)\big)\right)}, \tag{1.32}$$

where $y_C(TH_i)$ is the retrieval vector at tangent altitude TH_i, $I_n(\lambda_j, TH_i)$ is the normalized radiance at wavelength λ_j and tangent altitude TH_i. Re-arranging Equation 1.32 leads to:

$$y_C(TH_i) = \frac{I_n(\lambda_2, TH_i)}{\sqrt{I_n(\lambda_1, TH_i) \cdot I_n(\lambda_3, TH_i)}}, \tag{1.33}$$

which shows that the vector, $y_C(TH_i)$, is the ratio of the peak wavelength radiance and the geometric mean of the two reference wavelengths. The vector is a measurement of the decrease in radiance due to the presence of ozone (see Section 2.2 for further discussion of the Chappuis vector).

The radiative transfer model LIMBTRAN (see §1.7.1) is used to model the same three retrieval vector wavelengths forming the modelled vector. The modelled and measured vectors are then compared and the retrieved ozone density profile is updated using a nonlinear Newtonian iteration version of Optimal Estimation (see §1.9.2).

OSIRIS Version 2.5 ozone retrievals are affected by albedo, aerosols, and other instrument effects. The amount of error due to these effects has been estimated to be on the order of ten percent between 15 and 40 km (*von Savigny et al.*, 2005).

An added benefit of comparing the results of the new retrieval technique with OSIRIS Version 2.5 ozone density profiles is that the underlying data (the Optical Spectrograph measurements) are the same.

The OSIRIS Version 2.5 ozone product compares favorably with the other ozone products; although a general trend for the OSIRIS ozone density to be slightly low above 30 km has been noted by *von Savigny et al.* (2005), when the OSIRIS data set is compared with the POAM III data set. This discrepancy is one of the motivations for the present work.

1.10.2 SAGE II

SAGE II measures the attenuated solar radiation each orbital sunrise and sunset (solar occultation) using the solar irradiance outside the atmosphere as the unattenuated solar flux. As the line of sight from the satellite to the sun traverses the atmosphere, the amount of light measured by the instrument changes according to the amount of atmospheric absorption and scattering. The optical depth is calculated for each wavelength by normalizing the attenuated measurement to the direct solar measurement. Then using Beer's law, Equation 1.4, the concentration of scattering/absorbing particles is found. By using certain wavelengths, the amount of ozone needed in the

atmosphere to yield the measured optical depths can be found. SAGE II uses a modified Chahine nonlinear inversion algorithm to calculate the ozone density. A full description is given by *Chu et al.* (1989).

The ozone measurements of SAGE II have been validated to seven percent between 20 and 53 km (*Cunnold et al.*, 1989). The sources of error are aerosols, instrument effects and pointing error.

1.10.3 SAGE III

In a similar fashion to SAGE II, SAGE III measures the attenuated solar radiation at sunrise and sunset. This allows the atmospheric transmission to be calculated spatially throughout the atmosphere. The ozone profiles are then determined using a modified Chahine nonlinear inversion algorithm on data from 290 nm and 563–622 nm, *i.e.,* data from both the Chappuis and Hartley-Huggins wavelength bands. Because of the Hartley-Huggins data, the SAGE III retrieval is able to extend to higher altitudes than SAGE II. A full description is given by *Rind and McCormick* (2002).

The measurements of SAGE III ozone have been validated to five percent between 8 and 85 km (*Rind and McCormick*, 2002). The sources of error are other retrieved species (including NO_2 and aerosols), instrument effects, and pointing error.

1.11 Summary

This chapter has provided the foundation for the remainder of this work. The material covered the atmosphere (§1.3), atmospheric ozone (§1.4), and previous ozone studies (§1.5). Section 1.6 included a description of the OSIRIS instrument and the Optical Spectrograph measurements. Atmospheric radiative transfer modelling was the subject of Section 1.7 leading to the description of SaskTRAN, the radiative transfer model used in this work, Section 1.8. The various techniques used to retrieve ozone density profiles from radiance data were the subject of Section 1.9, including a detailed description of the Multiplicative Algebraic Reconstructive Technique that is used in the present work. Lastly, the comparison ozone products that are used in the present work were discussed in Section 1.10.

Chapter 2

Chappuis Ozone Retrieval

2.1 Introduction

Each of the techniques described in Section 1.9 can be used to determine ozone profiles from OSIRIS data. However, as it was developed specifically for the OSIRIS data and orbital geometry, the Multiplicative Algebraic Relaxation technique (MART) outlined in Section 1.9.4 is used to produce the ozone profiles in this work. The SaskTRAN model is used to calculate the theoretical line of sight radiances needed by the MART. The combination of the MART inversion technique and SaskTRAN radiative transfer model is referred to as the SaskMART retrieval technique.

Before considering the full retrieval treated in Chapter 3 that uses data from both the Chappuis and Hartley-Huggins band wavelengths in its inversion, this chapter is devoted to implementing the SaskMART retrieval technique using only radiance information from the Chappuis band. This simpler case demonstrates the functionality of the SaskMART retrieval and provides a direct comparison with OSIRIS Version 2.5 and SAGE II (see §1.10).

This chapter begins with an explanation of what data the SaskMART inversion technique uses to produce ozone density profiles, followed by a brief discussion of atmospheric factors that affect the inversion. Results are presented that compare the SaskMART retrievals with the previous OSIRIS ozone product and the ozone density profiles of SAGE II described in sections 1.10.1 and 1.10.2. Next, the wavelengths used by the SaskMART technique to produce the ozone retrievals are varied in order to choose suitable wavelengths. Finally, the uncertainty of the SaskMART retrieval technique is considered.

2.2 Chappuis Vector Triplet

2.2.1 Introduction

Multiplicative Algebraic Relaxation techniques adjust a modelled ozone concentration according to the ratio of two values, one measured and one modelled. For the technique to converge on a solution, the value used must be such that an increase in ozone concentration results in an increase in the value — the value used must be correlated to the density of ozone. In this chapter, the value used in the MART is not the OSIRIS radiance measurements themselves, but a combination of radiance measurements from three different wavelengths. It is:

$$\log\left(\frac{\sqrt{I_s \cdot I_l}}{I_p}\right), \tag{2.1}$$

where I_s, I_l, and I_p are the normalized radiance of a short reference wavelength, a long reference wavelength, and a peak wavelength, respectively, taken from within the Chappuis band ozone absorption. The value in Equation 2.1 meets the above conditions — it increases with an increase in ozone. If there is no ozone present in the atmosphere, the value is a constant with altitude. The value is basically the same as the vector used in previous OSIRIS ozone retrievals (Equation 1.32, § 1.10.1), only it is inverted to give a positive rather than a negative correlation. The use of a triplet vector made up of Chappuis band radiances to retrieve ozone profiles is also similar to the UV/visible pair and triplet formation theory used by SOLSE/LORE (*McPeters et al.*, 2000).

2.2.2 Normalization

All three of the wavelengths that make up the *Chappuis Vector Triplet* (CVT) have their radiances normalized to a higher altitude where there is no longer enough ozone to affect the radiance. That is,

$$I_n(TH) = \frac{I(TH)}{I(TH_{ref})}, \tag{2.2}$$

where $I_n(TH)$ and $I(TH)$ are the normalized and actual radiance at tangent height TH, respectively, and $I(TH_{ref})$ is the radiance at the reference tangent height. The result of normalization is that the effect of Earth albedo and instrument calibration on the measurements is decreased as a change in these factors affects both values the

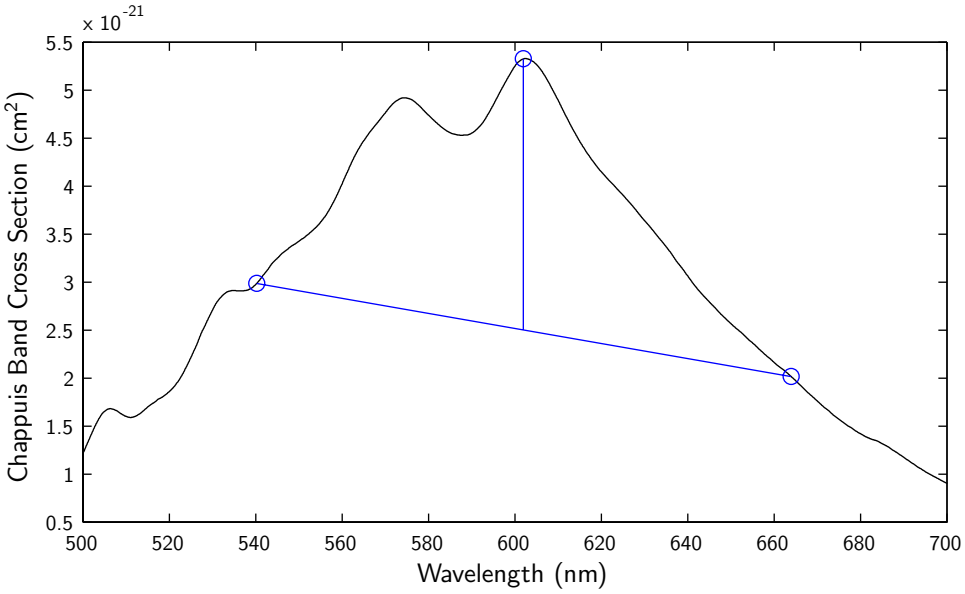

Figure 2.1: The wavelengths used in OSIRIS Version 2.5 retrievals (shown above) will also be used in the SaskMART retrieval. The ozone cross section data is at 273°K and is taken from *Burrows et al.* (1999).

same way (see Section 1.10.1). The use of normalization to minimize the vector's sensitivity to instrument absolute calibration, surface albedo, *etc.*, follows the work of *Flittner et al.* (2000), *Auvinen et al.* (2002), *Strong et al.* (2002), *McDade et al.* (2002), *von Savigny et al.* (2003), and *Haley et al.* (2004). As the highest retrieved tangent height for the Chappuis-only retrieval is 40 km, the radiance at the first tangent height above 40 km is used to normalize the radiances at the other tangent heights.

2.2.3 The CVT and Ozone Absorption

Figure 2.1 shows approximately where the short, peak, and long (left to right) wavelengths intersect the O_3 cross section.[1] Because of the difference in cross section at the peak and reference wavelengths, it is possible to infer the amount of ozone by relating the radiance information of the peak and reference wavelengths through the CVT.

The CVT represents the dip in the radiance due to ozone absorption (Figures 2.2 and 1.8); larger values of the CVT represent deeper troughs in the radiance caused by

[1]The ozone cross sections used in the analysis are temperature dependent profiles taken from *Burrows et al.* (1999).

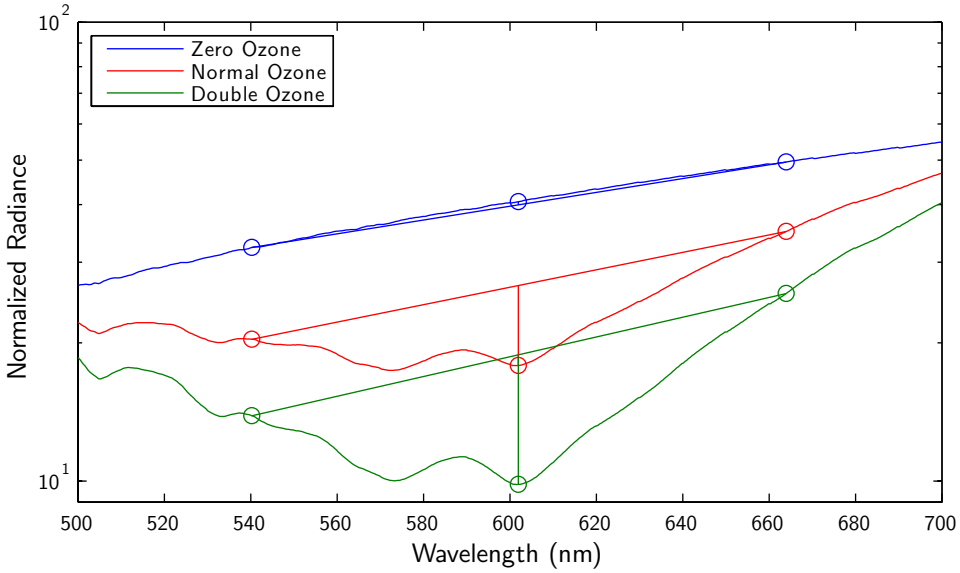

Figure 2.2: The three wavelengths of the OSIRIS Version 2.5 CVT shown on 15 km tangent altitude radiance data (normalized to 40 km). Three different ozone density profiles were used to show the effect of ozone density on the spectrum. The measurement of Equation 2.1 is correlated to the depth of the vertical lines.

increased amounts of ozone. The short and long wavelengths are outside the O_3 cross section peak and serve as reference values to the central wavelength. Figure 2.2 shows the results of these runs with SaskTRAN that changed only the amount of ozone in the model. As the amount of ozone increases so the Chappuis band absorption becomes deeper. The length of the vertical lines in Figure 2.2 is a measurement of the CVT.

The three Chappuis measured wavelengths as well as the CVT are shown in Figure 2.3. Below 40 km, where the ozone absorption is significant, the radiance at the peak wavelength decreases from the expected exponential increase (Panel (a)) and the value of the CVT increases (Panel (b)). Above 40 km, there is a slight increase in the CVT with altitude. This is due to the relative increase of the long wavelength radiance (green curve) in Panel (a) at higher altitudes. The reason for this increase in radiance contrary to the expected exponential decrease, is that the instrument optics are allowing light from lower altitudes to contaminate the signal up high (stray light signal). The reason it is apparent in the long wavelength and not the other two wavelengths is that the signal strength of the long wavelength is the lowest of the three wavelengths.

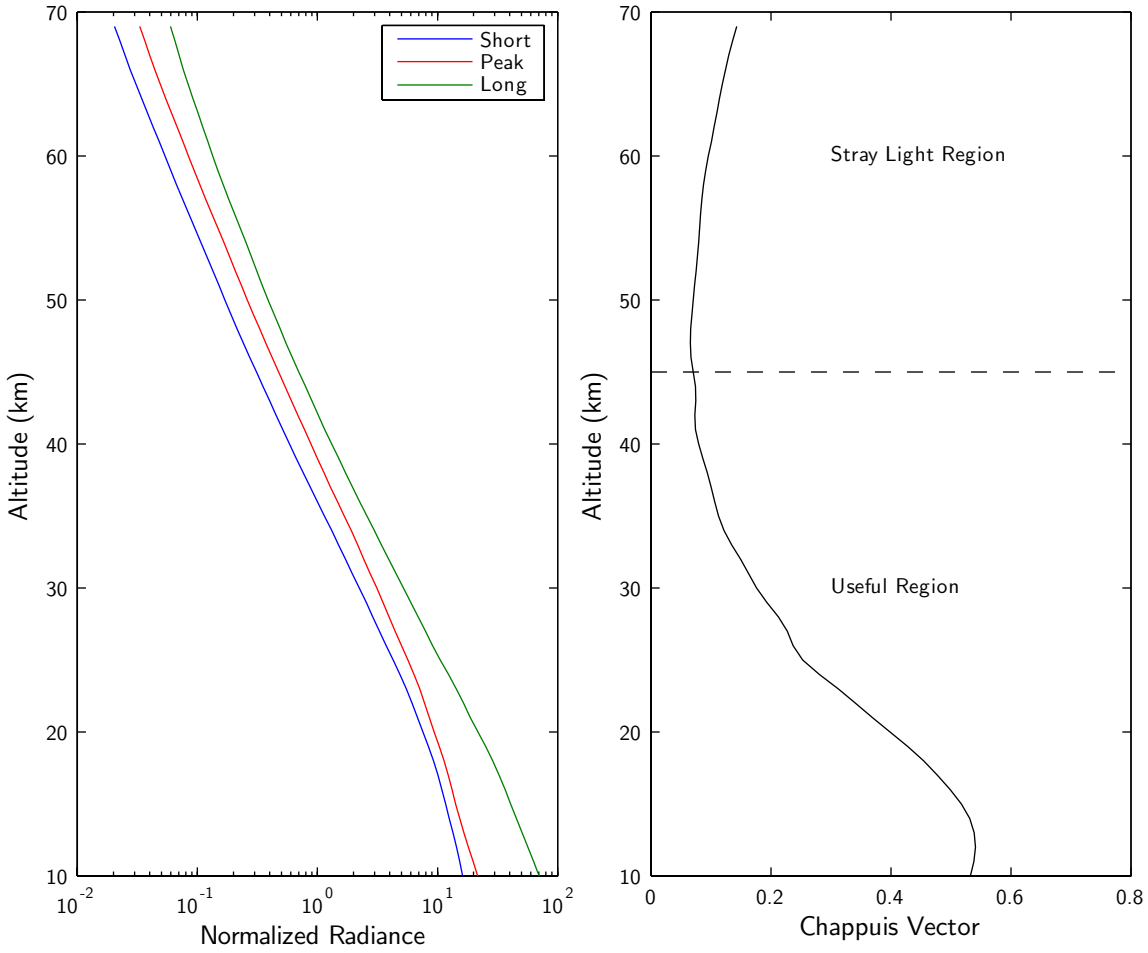

(a) The radiance of the three Chappuis wavelengths (normalized and shifted) decreases exponentially with altitude. With the introduction of ozone in significant quantities (below 40 km), the radiance profile of the peak wavelength (red) does not increase with a decrease in tangent altitude at the same rate as the two reference wavelengths.

(b) As altitude drops, the value of the Chappuis vector remains small (under 0.2) until the amount of ozone increases to a significant amount (below 40 km). With the introduction of ozone corresponding to the peak radiance drop off, the Chappuis vector increases indicating the presence of ozone.

Figure 2.3: Chappuis Radiance and Vector on Altitude

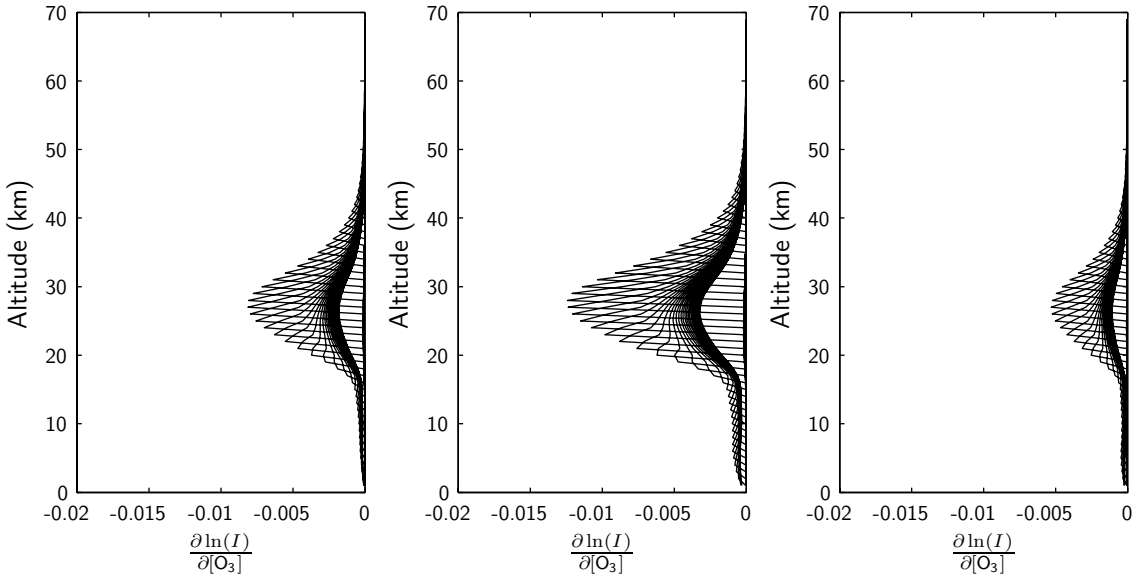

(a) Short Reference Wavelength. (b) Peak Wavelength. (c) Long Reference Wavelength.

Figure 2.4: The radiance Jacobians for the three wavelengths making up the CVT.

Figure 2.4 shows how the model radiances of the short reference, peak, and long reference wavelengths change with respect to a change in modelled ozone density. Logarithms of the radiance values are shown as it is the logarithmic values of the radiance that make up the CVT (Equation 2.1). The ozone density profile is increased by 10% at each separate altitude, and the change in radiance is calculated at each tangent altitude. The resulting changes fill a square matrix called the Jacobian. Figure 2.4 plots the radiance Jacobian. Each curve represents the change in radiance due to a change in ozone density at a given tangent altitude. Typically, the resulting change in radiance is negligible below the altitude the ozone density was changed, then spikes at that altitude and drifts back to zero change. There is a negative correlation for all three wavelengths; that is, an increase in the amount of ozone causes a decrease in the radiance. The change in radiance of the peak wavelength (Panel (b)) exceeds that of the reference wavelengths.

Figure 2.5 shows how the CVT changes with respect to a change in modelled ozone density, the values were calculated using the wavelengths shown in Figure 2.3 and the radiance Jacobians shown in Figure 2.4. For any given tangent altitude, the change in the CVT caused by a change (increase) in ozone density below that altitude is small because the line of sight radiances that make up the CVT do not travel through the region of increased ozone. The actual change is due to the multiple-

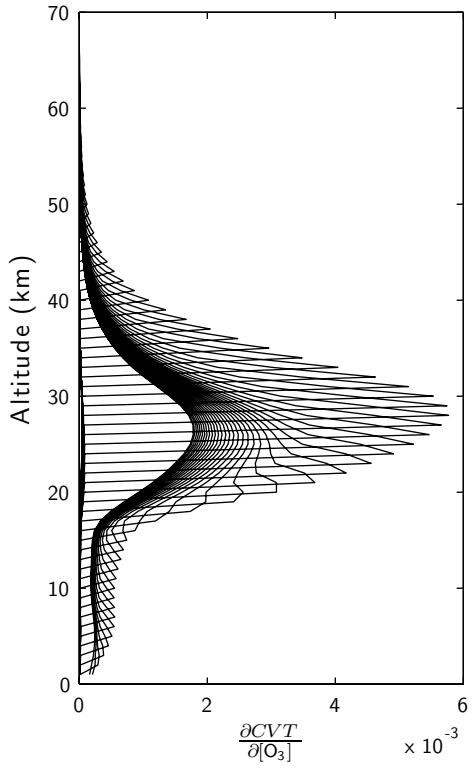

Figure 2.5: Using the radiance Jacobians of Figure 2.4, the CVT Jacobian was calculated. A positive correlation exists between the CVT and ozone density at all altitudes.

scattered light from below and is small because the ratio of multiple-scattered light to single-scattered light is low at these wavelengths. A change in ozone density at the altitude where the CVT is tangent produces a pronounced increase in the CVT. This is because the constituent radiances are significantly diminished due to increased absorption caused by the increase in ozone. Changes to the ozone density at an altitude above the CVT tangent altitude of interest continue to show a positive correlation because the line of sight passes through the changed ozone region. As the distance between the given tangent altitude and the altitude at which the ozone changes becomes larger so the overall effect on the CVT decreases due to the decrease in the line of sight path length through the changed region. The peak in the CVT Jacobian occurs at 25–30 km — near the height of the maximum ozone concentration. The range over which the CVT Jacobian is usable for the purposes of the Chappuis-only MART is 0–40 km.

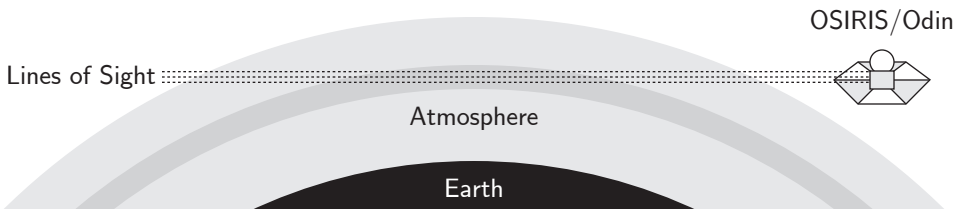

Figure 2.6: Different lines of sight through the shaded tangent altitude region.

2.2.4 Tangent Height Weighting

The value used in the MART to retrieve the amount of ozone at an given tangent height is not based on the vector of a single line of sight, rather it is based on the vectors of three lines of sight. Figure 2.6 shows that there are multiple lines of sight that pass through a given altitude range. The SaskMART retrieval takes the three longest paths through a region and uses the vector information from all three in its retrieval. They are weighted so that the highest tangent height through the region has a weight of 0.6, the next highest has a weight of 0.3, and the lowest, 0.1. These weights correspond to the W_{ij} terms in Equation 1.30.

2.2.5 The Initial Guess Ozone Profile

The initial ozone profile included in the MART, known as the *initial guess,* is taken from a climatological model of ozone based on the unpublished work of R. D. McPeters and G. J. Labow in 2002–2003. The climatology calculates the volume mixing ratio of ozone and is converted into an ozone density profile.

The MART iteratively adjusts the values of the initial guess profile until the measured and modelled vectors used in the MART are in agreement. For the Chappuis-only retrieval, the adjustments are typically made between 10 and 40 km. However, the SaskTRAN model requires the ozone density profile from the ground to 100 km. For this reason the ozone density values above the highest retrieval altitude are adjusted by the same factor as the highest retrieval altitude. The same is done for the ozone density values below the lowest retrieval altitude. This is done in order to avoid discontinuities in the modelled ozone density profile; the magnitude of ozone density above and below the retrieval region changes but the relative shape is unchanged.

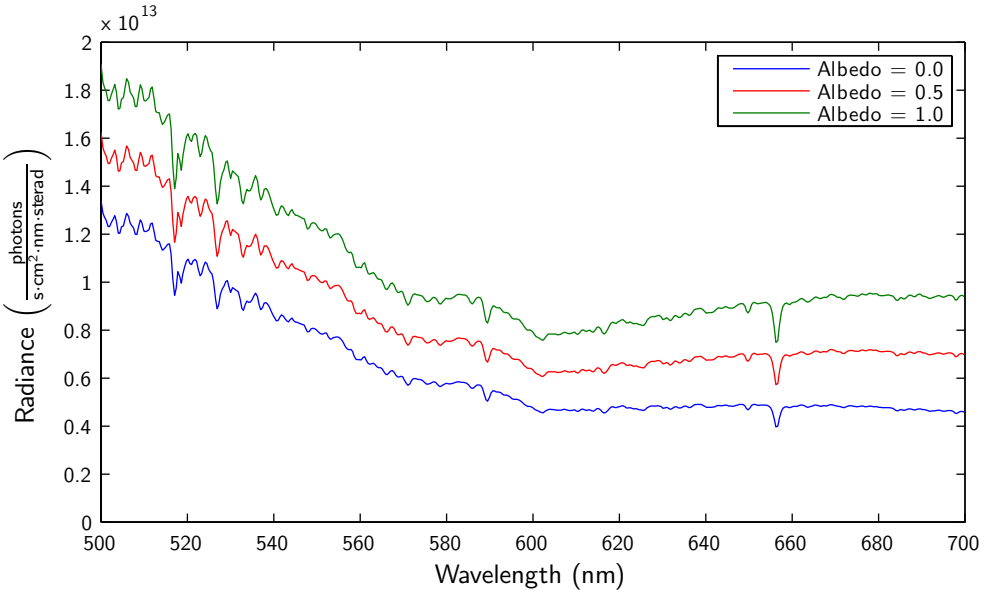

Figure 2.7: An increase in Earth albedo causes an increase in radiance at 15 km. It also raises the value of the CVT. Using the long, peak, and short wavelength values of Figure 2.1, the value of the CVT is 0.3351 for an albedo of 0.0, 0.3537 for an albedo of 0.5, and 0.3624 for an albedo of 1.0.

2.2.6 Effect of Albedo on Chappuis Vector Triplet

The Earth albedo is the ratio of light reflected from the Earth's surface to the light incident on the Earth's surface and so is a measure of the reflectivity of the Earth's surface. An increase in the value of the Earth albedo in the SaskTRAN model results in an increase in the modelled radiance. The SaskTRAN model was run for three different albedo values to show the effect of the albedo on the CVT. Figure 2.7 shows the model results for a sample scan. The change in radiance values due to the change in albedo results in a change in the CVT. However, because the effects of the albedo are generally consistent across the Chappuis wavelength range, the vector triplet changes little for a full scale change in albedo. For a increase in albedo from 0.0 to 1.0, the modelled results in Figure 2.7 give an eight percent increase in the CVT.

2.2.7 Effect of Aerosol Load on Chappuis Vector Triplet

Aerosols are suspended particles that both absorb and scatter light. Stratospheric aerosols originate from a variety of sources, natural and anthropogenic; these include volcanic eruptions (SO_2 and HCL), naturally occurring OCS and industrial pollutants (mainly SO_2). The presence of aerosols causes the amount of light scattered in the

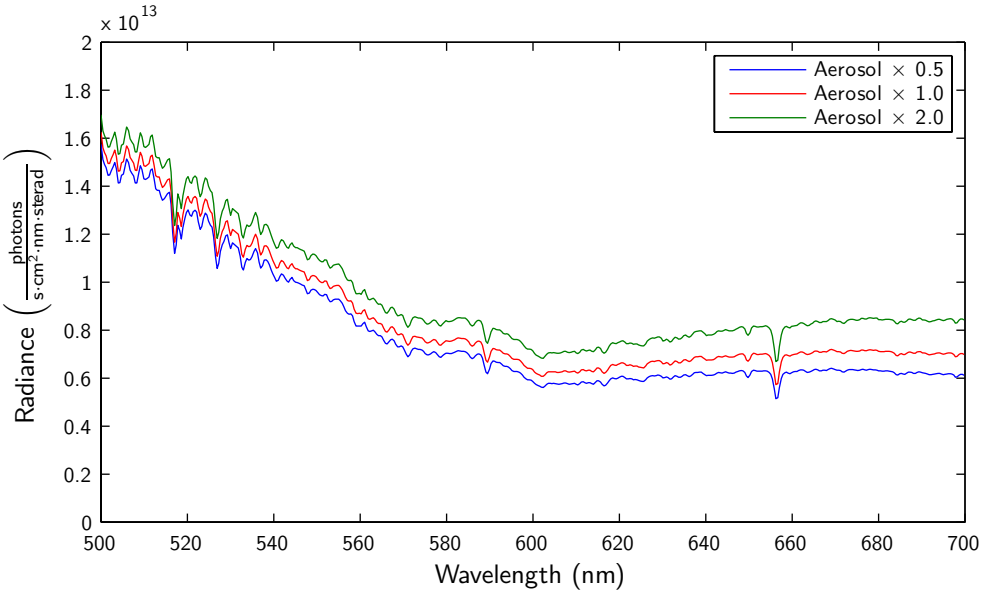

Figure 2.8: An increase in aerosol particle density causes an increase in radiance at 15 km (more in the red end of the spectrum than the blue). The value of the CVT changes slightly with change in aerosol load. The value of the CVT is 0.3509 for half the standard aerosol load, 0.3537 for the standard aerosol load, and 0.3540 for twice the standard aerosol load.

atmosphere to increase. The relative increase is larger in the red end of the spectrum than in the blue end.

The SaskTRAN model was run for three different amounts of aerosol in the atmosphere to show the effect of aerosol loading on the CVT. Figure 2.8 shows the model results for a sample scan (note that the increase in radiance is higher at the red end of the spectrum). The effect of changing the aerosol load from half to twice the standard load is less than the effect due to a full scale change in the albedo. Because the effects of aerosols are once again generally consistent across the Chappuis wavelength range, the vector triplet does not vary significantly with a large change in aerosol loading.

When the aerosol loading is halved, there is a one percent decrease in the CVT according to the results shown in Figure 2.8; when the aerosol loading is doubled, there is a negligible increase in the modelled CVT.

2.2.8 Summary

The SaskMART technique varies the amount of ozone in the model in order to align the modelled CVTs with the measured CVTs at all altitudes in the ozone retrieval.

Specifically, Equation 1.29 is used, with $x_i^{(n)}$ being the ozone number density at the i^{th} altitude after the n^{th} iteration, and the y_{jk} terms representing the k^{th} observation (measured and modelled) along a line of sight denoted by j. The k different observations are the ratios of measured and modelled CVTs.

Section 2.2.4, described how multiple lines of sight are used for each observation. This was followed by a discussion of the initial ozone density profile used in the SaskMART retrieval and how they are merged into the SaskMART retrieval. Sections 2.2.6 and 2.2.7 showed that the CVT is not affected greatly by changes in the the Earth albedo and modelled aerosol levels.

2.3 First Comparison Set

In this section, mean ozone density profiles retrieved using the SaskMART technique are compared with the previous OSIRIS ozone product and the SAGE II ozone product (see §1.10.1 and §1.10.2). While it is possible to compare individual profiles that coincide in latitude, longitude, and time, it is statistically more meaningful to compare sets of data.

2.3.1 Coincident Scans

Figure 2.9 is a superposition of OSIRIS and SAGE II scan latitudes and times. Panel (a) shows eight months of scan latitudes for both instruments. Sunlit portions of the OSIRIS orbit are evident. The data were examined for areas of increased overlap; the result is Panel (b), an enlarged view of the marked rectangle in Panel (a). Panel (b) shows that at $-37°$ latitude, January 4–6, 2004, there are 28 OSIRIS scans and nine SAGE II scans in close proximity. These two sets of scans have been compared in order to measure the accuracy of the SaskMART technique using the CVT.

However, it should first be noted that while the OSIRIS and SAGE II scans are close in latitude and time, no restriction has been placed on longitude. For this comparison, longitudinal differences are ignored in order to maintain a minimal comparison set size (adding longitudinal criteria limits the comparison to single scans). For these differences to be ignored, it is necessary to show that the variation in ozone density with longitude is small compared with the variation in ozone density with

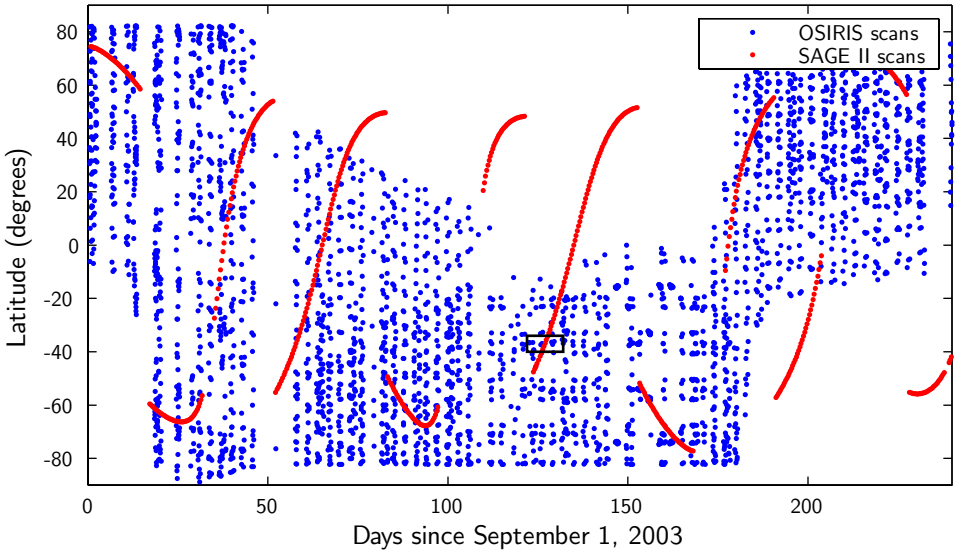

(a) OSIRIS and SAGE II scans for an eight month period starting September 1, 2004. The coincidence scans were taken from the area marked by the rectangle and enlarged in Panel (b). Note the increased coverage of OSIRIS compared with SAGE II (see §1.5.3).

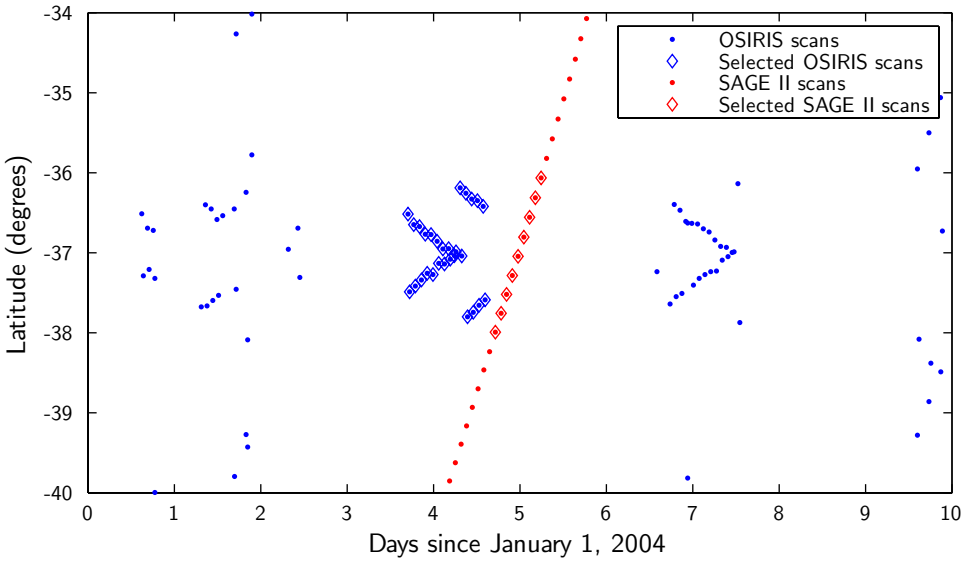

(b) Coincident OSIRIS and SAGE II scans used to compare and validate the retrieved ozone profiles. There are twenty-eight OSIRIS scans and nine SAGE II scans.

Figure 2.9: The first comparison set.

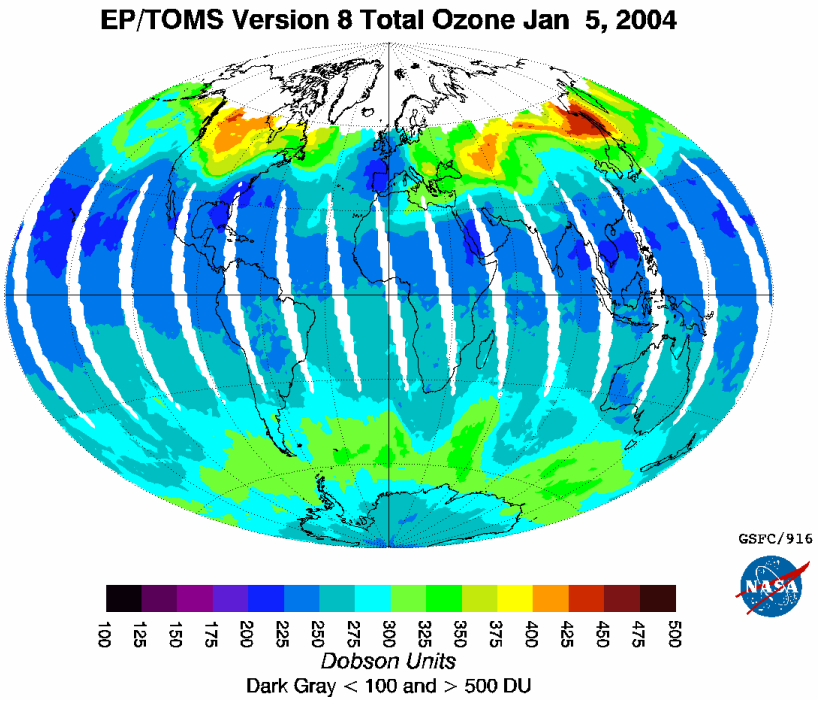

Figure 2.10: Global map of total ozone for January 5, 2004, measured by NASA's Earth Probe TOMS. In general, large scale structure in the ozone profiles occurs along longitudes. There is some structure along latitude bands; but the trend toward latitudinal homogeneity can be seen (with the exception of the northern mid-latitudes in this example). The first comparison set uses data taken by SAGE II and OSIRIS on this date, at $-37°$ latitude, where the assumption of latitudinal homogeneity holds.

latitude at the latitude of the comparison sets. Daily total ozone maps have been used to confirm this assumption.

Figure 2.10 is a global total ozone map measured by NASA's Earth Probe TOMS (total ozone mapping Spectrometer, see §1.5.3). The colour over each region indicates the total ozone column at that particular location (there is no data for the areas inside the white stripes). The figure shows that the variation with longitudinal bands is much smaller than the variation with latitudinal bands. It is apparent from Figure 2.10 that the total ozone column at $-37°$ (the latitude of Figure 2.9(b)) varies from 250 to 325 DU and is typically between 275 and 300 DU. In contrast, the variation in total ozone at different latitudes is much greater.

Additionally, by comparing total ozone maps for the days on either side of January 5, 2004, (Figures 2.10 and 2.11) show that total ozone does not vary much over a two day period at $-37°$. This validates the assumption that it is appropriate to compare scans that are within several days of each other.

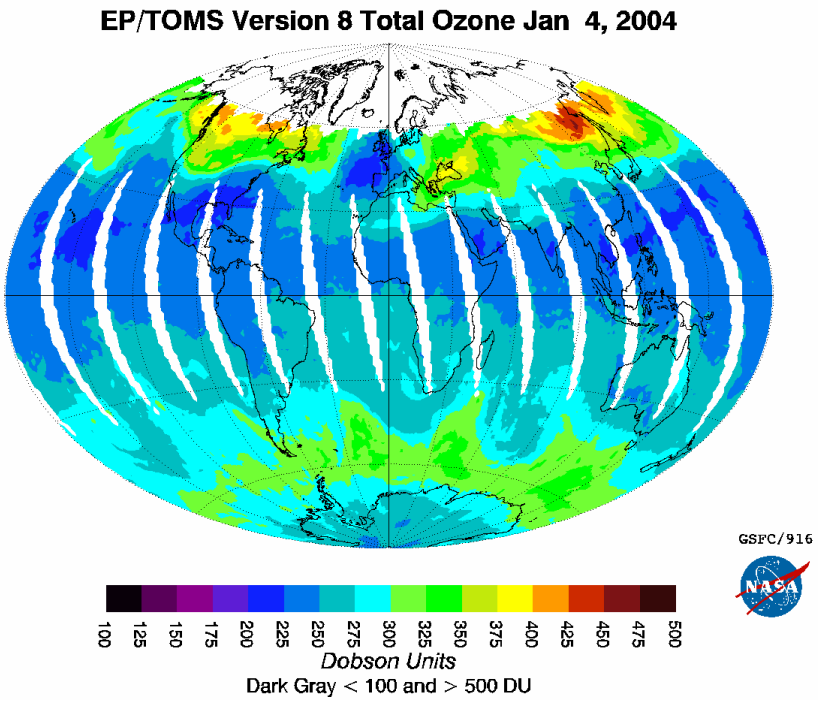

(a) EP/TOMS Total Ozone for January 4, 2004

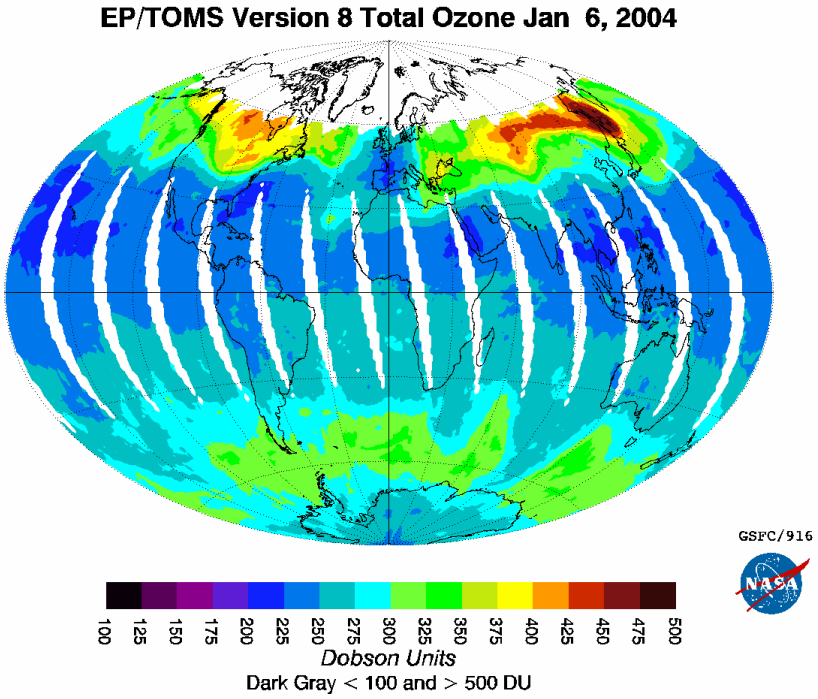

(b) EP/TOMS Total Ozone for January 6, 2004

Figure 2.11: The global maps of ozone when taken a day before and after Figure 2.10 show that over the course of two days, large scale changes in ozone density do not occur at $-37°$ latitude.

2.3.2 OSIRIS Version 2.5 and SAGE II Comparison

Before comparing any retrievals made with the SaskMART technique, it is necessary to demonstrate that the mean OSIRIS Version 2.5 and SAGE II profiles agree to within their stated limits. Figure 2.12 shows the mean OSIRIS Version 2.5 and SAGE II profiles for the latitudes and times indicated in Figure 2.9. There is agreement to within the combined 17% error between 20 and 40 km. The mean OSIRIS Version 2.5 profile is lower than the mean SAGE II profile at all altitudes. This agrees with the general trend noted in Section 1.10.1.

The dashed lines in Figure 2.12(a) represent the standard deviation of the OSIRIS Version 2.5 and SAGE II profiles. Below 30 km, the difference between the two average profiles is less than the combined standard deviation thus means that they agree statistically without consideration of the combined 17% confidence.

The fact that the mean profiles in Figure 2.12 agree to within their stated limits and have the same profile shape demonstrates that comparing OSIRIS Version 2.5 and SAGE II profiles at this latitude and time is a valid method for comparing different retrieval techniques. As the SaskMART technique uses the same underlying data as the previous OSIRIS ozone product, it is expected that SAGE II retrievals should compare with the SaskMART retrieval in much the same way as the previous OSIRIS ozone product does.

2.3.3 SaskMART Retrieval using OSIRIS Version 2.5 CVT

The SaskMART retrieval algorithm has been tested using the same wavelength triplet that is used in the OSIRIS Version 2.5 ozone product; namely, 540.24, 601.99, and 663.94 nm. The spectra in this wavelength region are shown in Figures 2.1 and 2.2. The signals at these wavelengths form the OSIRIS Version 2.5 CVT:

$$\log\left(\frac{\sqrt{I_{540}\cdot I_{664}}}{I_{602}}\right). \tag{2.3}$$

Using the Version 2.5 CVT and the SaskMART retrieval method yields the mean profiles shown in Figure 2.13. The agreement between the three mean profiles is apparent. In addition, the SaskMART retrieval corrects the systematically low concentrations above the ozone peak that are apparent in the OSIRIS Version 2.5 mean retrieval. Thus the Chappuis-only SaskMART retrieval is of comparable quality to that from OSIRIS Version 2.5.

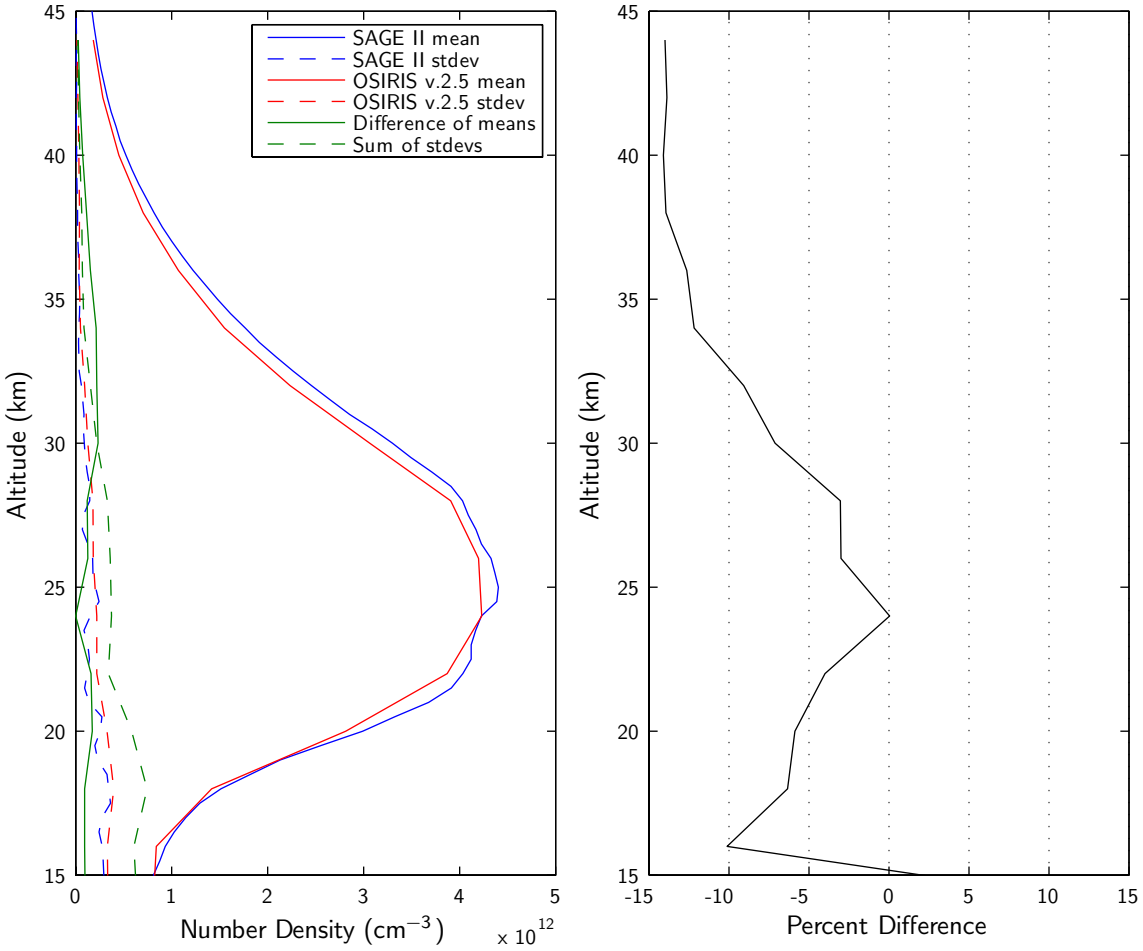

Figure 2.12: A comparison of SAGE II and OSIRIS Version 2.5 retrieved ozone profiles. OSIRIS Version 2.5 retrievals are systematically lower than SAGE II over the entire profile, this is most noticeable at and above the ozone peak. The difference between profiles is always less than 17% between 20 and 40 km.

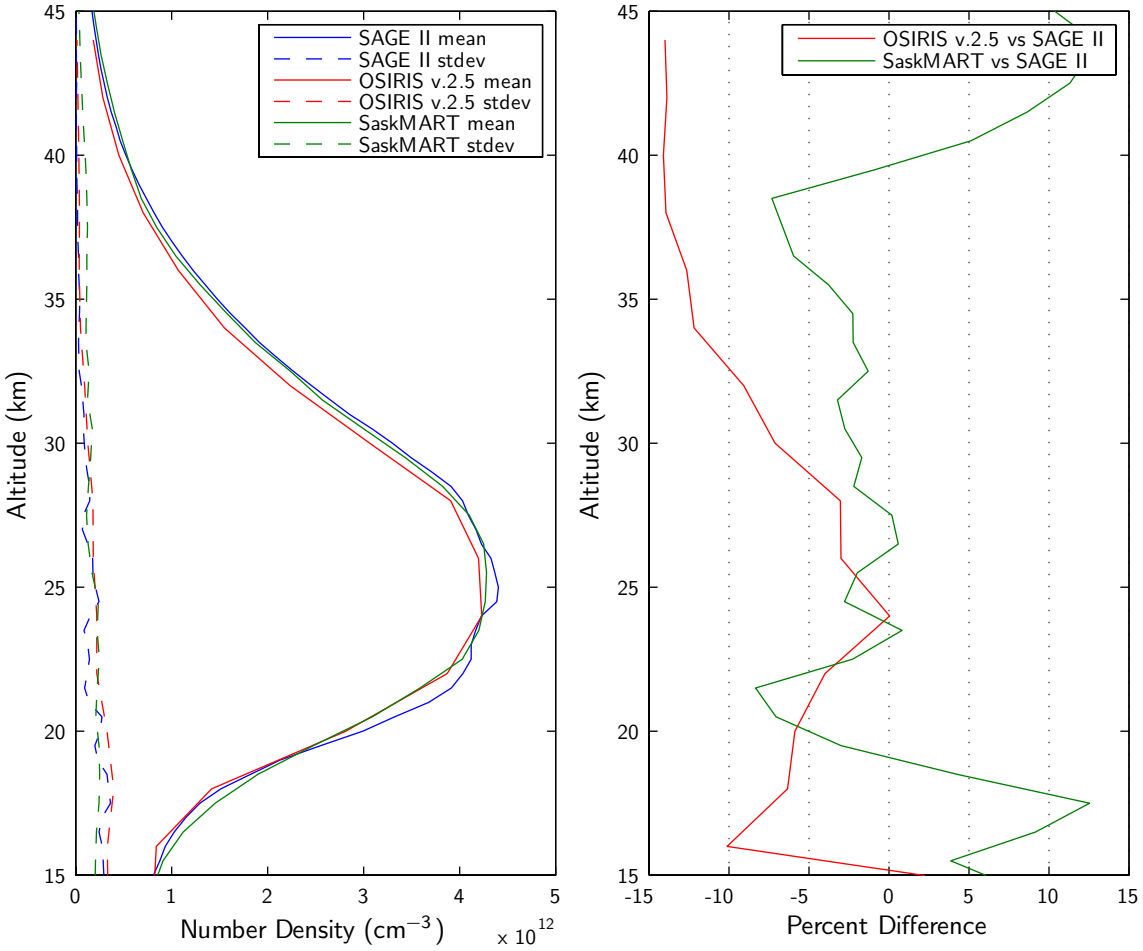

Figure 2.13: A comparison of SAGE II, OSIRIS Version 2.5, and SaskMART retrieved ozone profiles. This SaskMART retrieval uses the same CVT as in the OSIRIS Version 2.5 retrieval. The SaskMART retrieval does not share the systematic low above the ozone peak that is present in the OSIRIS Version 2.5 retrieval.

2.4 Varying Triplet Wavelengths

Using the OSIRIS Version 2.5 CVT in the SaskMART retrieval technique resulted in a mean profile that compared favourably with the SAGE II mean profile. However, any carefully selected triplet comprised of a reference wavelength on either side of the O_3 absorption cross section peak and one at the peak should also yield results in good agreement with the OSIRIS Version 2.5 triplet. However, it is of value to search different CVTs in order to find a triplet that performs well when compared with the validated SAGE II ozone product. The objective is to identify wavelengths in the CVT that give results that vary the least when compared to the results of other wavelengths, *i.e.*, the most consistent wavelengths.

In the results presented in the following three sections, each of the three wavelengths in the CVT have been varied while keeping the other two constant. The results of these sections are used to form new triplets that can be used to compare with the OSIRIS Version 2.5 CVT retrievals.

2.4.1 Varying the Short Wavelength Component

There are two limits to the range over which the short reference wavelength can be varied. The lower limit comes from the fact that there is no radiance information below 531 nm due to the spectral order sorter in the OSIRIS optical system (see §1.6.1). The upper limit is imposed by the cross section itself. A reference wavelength must not have significant ozone absorption if it is to be useful as a reference.

Within these constraints, several wavelengths recorded by OSIRIS are highlighted by red circles in Figure 2.14; there are 14 selected wavelengths between 540 and 546 nm. Each of these wavelengths has been tested and the results are presented.

Figure 2.15 plots these 14 wavelengths on the 15 km OSIRIS Spectrum. The Fraunhofer structure in this region is responsible for the small scale structure in the radiance. The structure in this region makes modelling at these wavelengths difficult. For this reason, it is to be expected that some pixels in this region are more effective than others.

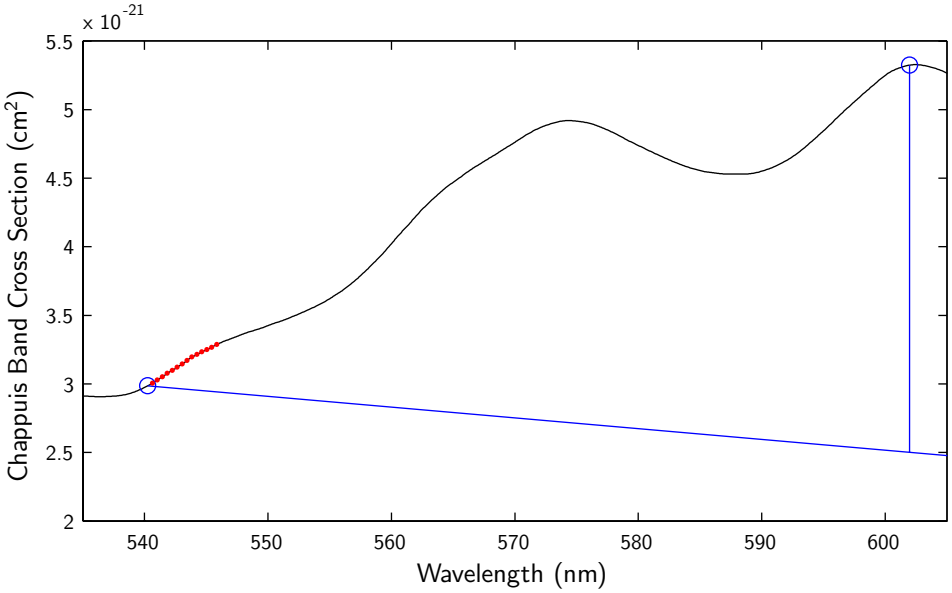

Figure 2.14: Selected short reference wavelengths superimposed on the O_3 cross section. Each red dot represents a wavelength that has been tested for use as the short reference wavelength in the CVT. The two blue circles are the short reference and peak wavelengths used in the OSIRIS Version 2.5 CVT.

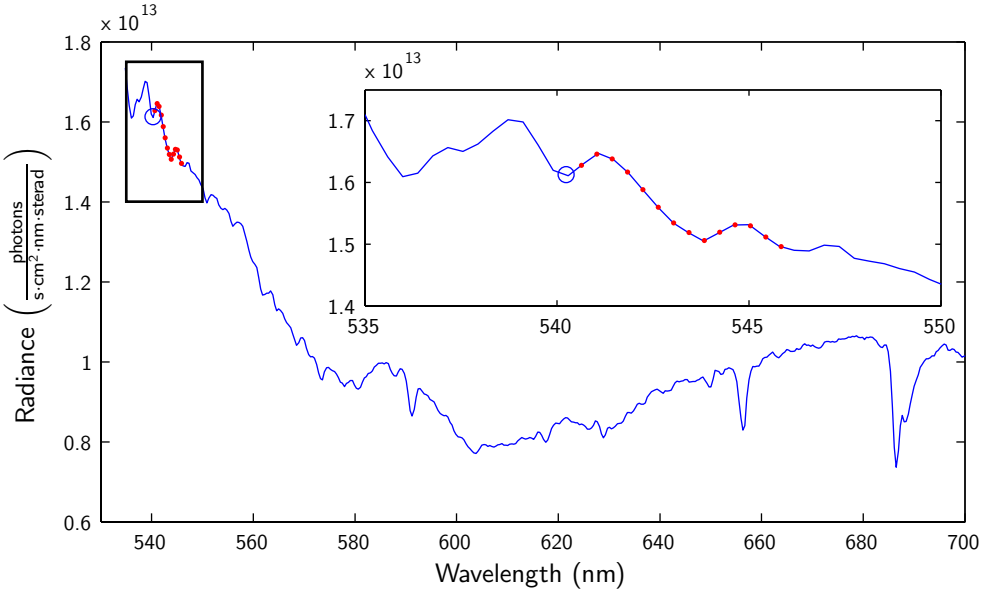

Figure 2.15: Selected short reference wavelengths on the 15 km OSIRIS Spectrum. Each red dot represents a wavelength that will be tested for use as the short reference wavelength in the CVT. The blue circle is the short reference wavelength used in the OSIRIS Version 2.5 CVT. The inner plot is a magnification of the marked area. In this wavelength region, the change in radiance with respect to a change in wavelength is high.

2.4.2 Results of Varying the Short Wavelength Component

Figure 2.16 shows the results of varying the short reference wavelength in the CVT retrieval. Using the same data set as that used to produce Figures 2.12 and 2.13; the mean ozone density profile has been calculated for each of the 14 wavelengths shown in Figure 2.15 and is shown in Figure 2.16(a). The 14 green lines in Panel (b) are the percent differences between these 14 profiles and the mean SaskMART retrieval using the OSIRIS Version 2.5 CVT in Panel (a). The mean SAGE II profile is also given for reference.

There is almost no difference in the mean retrieved profile depending on which short reference wavelength is selected. The differences between the OSIRIS Version 2.5 short reference wavelength and the ones tested in this section lead to a maximum change in the mean retrieved profile of about two percent between 20 and 35 km.

The similarity of the mean profiles means that any of these wavelengths is a valid choice for use as the short reference wavelength in the CVT. In order to rate the trial wavelengths for use as the short reference wavelength, the results of each trial have been compared to the results of the other trial wavelengths to find the profiles that varied the least from the other profiles. The most consistent wavelengths, using a least squares difference, are 540.24 nm, which is the short reference wavelength in the OSIRIS Version 2.5 CVT, and 541.44 nm.

2.4.3 Varying the Peak Wavelength Component

The central wavelength in the retrieval triplet corresponds to the peak of the O_3 absorption cross section, which occurs near 601 nm. There is another smaller peak at 571 nm. It is expected that central wavelengths from either peak should result in similar answers, although the larger absorption at 601 nm should make it the better of the two peaks. Four wavelengths from around the minor peak at 571 nm and five wavelengths (in addition to the central OSIRIS Version 2.5 CVT wavelength) near the major peak at 601 nm have been tested. The selected wavelengths are shown in Figure 2.17.

Figure 2.18 shows the tested peak wavelengths on the the 15 km OSIRIS spectrum. The radiance at 601 nm is noticeably less than at 571 nm due to the difference in the absorption cross section. The increased radiance at 585 nm corresponds to the

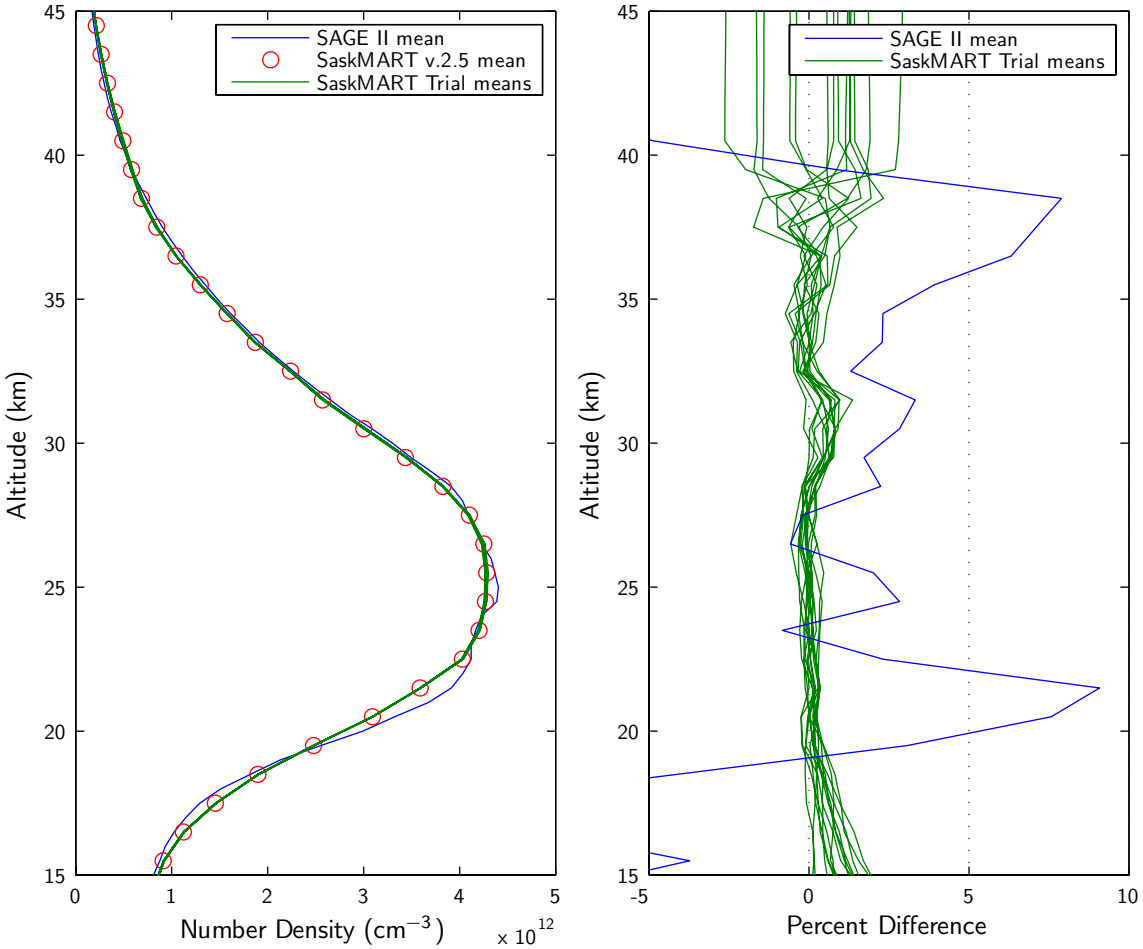

(a) Mean retrieved profile comparison.

(b) Percent difference.

Figure 2.16: Comparison of retrievals using the peak and long reference wavelengths of the OSIRIS Version 2.5 CVT with variable short reference wavelengths. The various short reference wavelengths produced similar profiles, to within two percent of the baseline OSIRIS Version 2.5 CVT between 20 and 35 km.

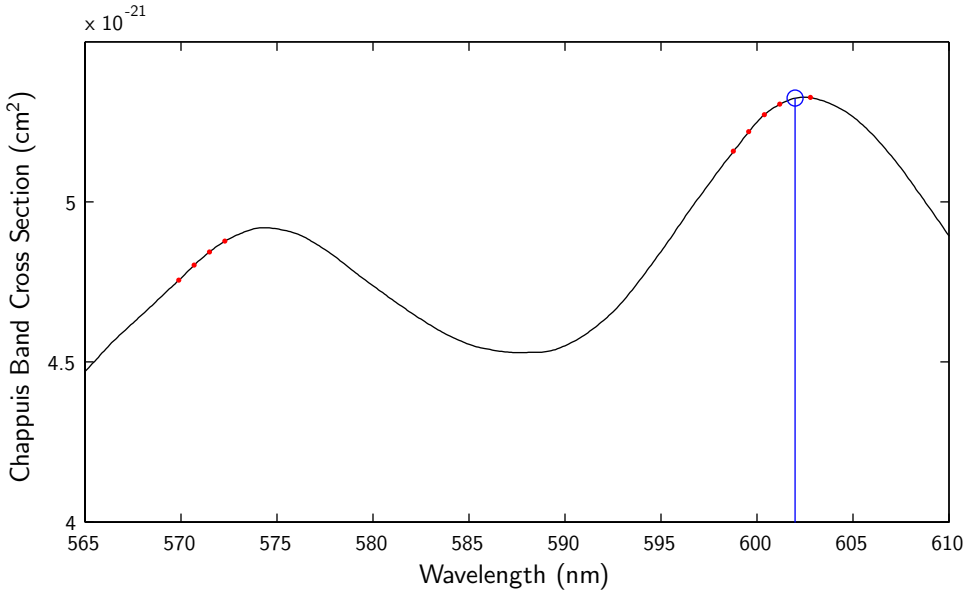

Figure 2.17: Selected peak wavelengths on the O_3 cross section. Each red dot represents a wavelength that has been tested for use as the peak wavelength in the CVT. The blue circle is the peak wavelength used in the OSIRIS Version 2.5 triplet.

trough between the two peaks in the absorption cross section that is apparent in Figure 2.17. Some possible wavelength choices were avoided because there is small scale structure on the radiance spectrum at these wavelengths (*e.g.,* 574 nm).

2.4.4 Results of Varying the Peak Wavelength Component

Figure 2.19 shows the results from varying the peak wavelength of the retrieval CVT. The nine green lines in Panel (a) correspond to the nine green percent difference lines in Panel (b). The mean SAGE II profile is again given as a reference. While there were almost no differences associated with the choice of short reference wavelength, the differences associated with different peak wavelength choices are obvious.

The first difference between the mean retrieved profiles occurs at the peak of the ozone density profile (25 km). Here, six of the nine wavelengths retrieve higher values than the OSIRIS Version 2.5 mean profile and are more consistent with the SAGE II peak. Two of these profiles correspond to wavelengths near the major absorption peak, the other four are from the minor peak.

Below 20 km, the sets of lines in Figure 2.19(b) diverge again. The set of five to the left correspond to the five wavelengths chosen from the major absorption peak; the four to the right are from the minor absorption peak. The reason for this splitting

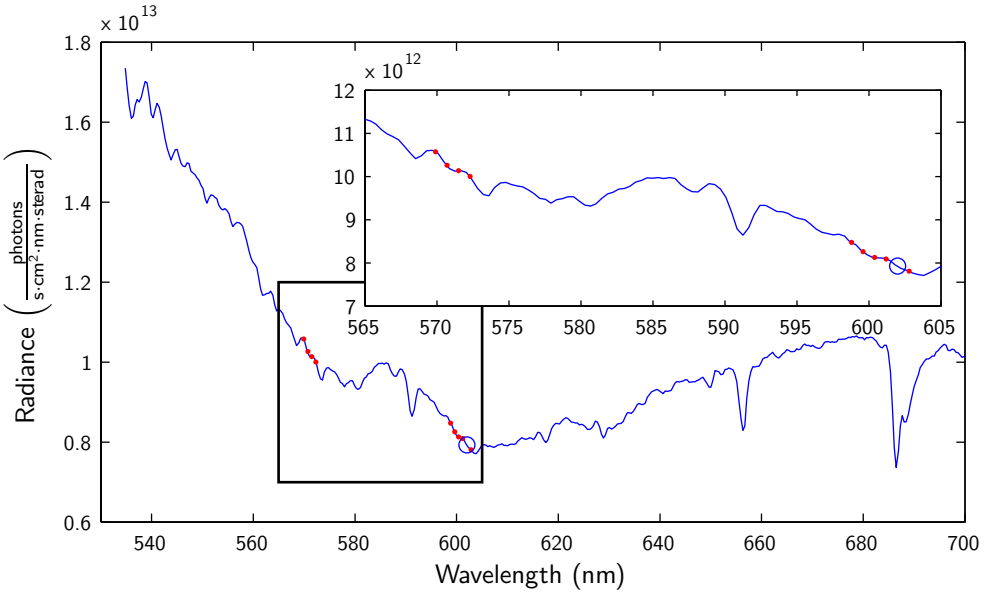

Figure 2.18: Selected peak wavelengths on the 15 km OSIRIS Spectrum. Each red dot represents a wavelength that has been tested for use as the peak wavelength in the CVT. The blue circle is the peak wavelength used in the OSIRIS Version 2.5 CVT. The inner plot is a magnification of the marked area.

is unknown although it is possible that there is contamination from other absorption or emission lines.

The differences between the OSIRIS Version 2.5 CVT peak wavelength and the ones tested here lead to a maximum change in the mean retrieved profile of four percent between 20 and 35 km.

The two peak wavelengths that are most consistent with the other wavelengths and SAGE II are among the group of six that yield a higher ozone density value at 25 km and then transition to follow the majority of the retrievals below 20 km. These peak wavelengths are 598.78 nm and 599.58 nm, both are from the major ozone cross section peak near 601 nm.

2.4.5 Varying the Long Wavelength Component

The wavelength with the most freedom is the long reference wavelength. It must be far enough away from the peak absorption region in order to serve as a reference and yet close enough that the effect of other variables, such as albedo and aerosol loading, is minimal.

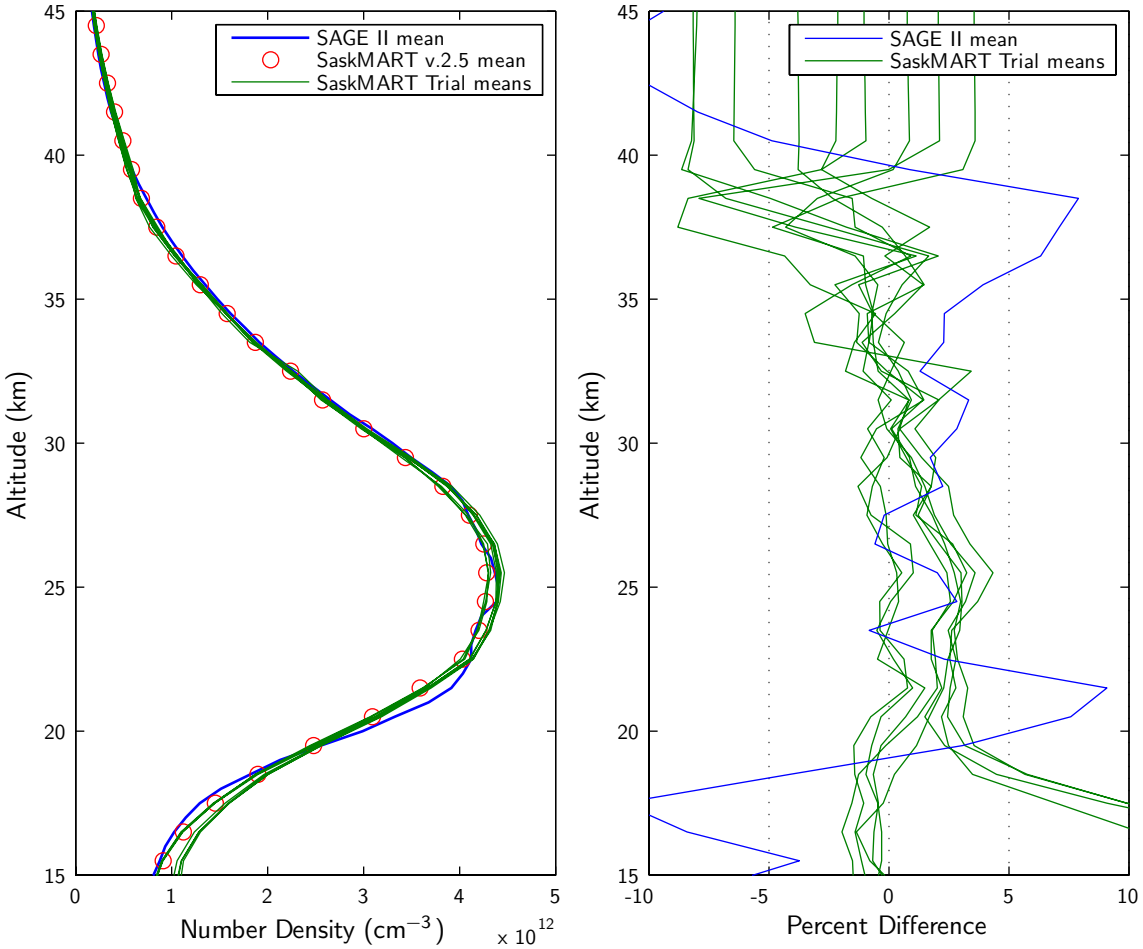

(a) Mean retrieved profile comparison.

(b) Percent difference.

Figure 2.19: Comparison of retrievals using the short reference and long reference wavelengths of the OSIRIS Version 2.5 CVT with variable peak wavelengths. The various peak wavelengths produced similar profiles, to within four percent of the baseline OSIRIS Version 2.5 CVT between 20 and 35 km.

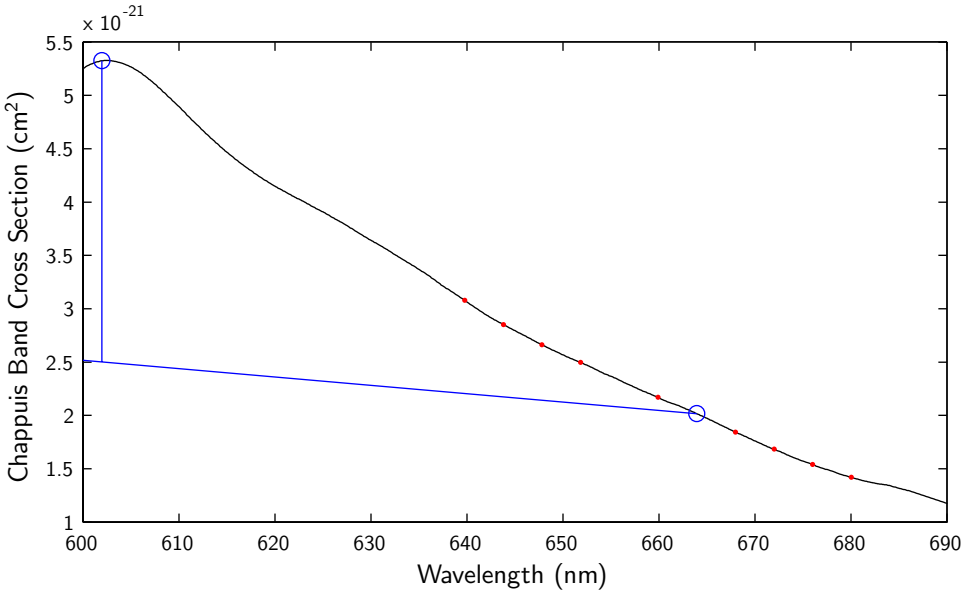

Figure 2.20: Selected long wavelength references on the O_3 cross section. Each red dot represents a wavelength that has been tested for use as the long wavelength in the CVT. The two blue circles are the peak and long reference wavelengths used in the OSIRIS Version 2.5 CVT.

The tested wavelengths recorded by OSIRIS are shown in Figure 2.20. There are nine wavelengths between 640 and 680 nm.

Figure 2.21 plots the nine long reference wavelengths on the 15 km OSIRIS spectrum. Wavelength regions to avoid in this region are the Fraunhofer feature at 658 nm and the oxygen B-band at 690 nm.

2.4.6 Results of Varying the Long Wavelength Component

Figure 2.22 shows the result of varying the long reference wavelength in the retrieval CVT. The nine green lines in Panel (a) correspond to the nine green lines in Panel (b). As for the evaluation of the short reference wavelength, the differences between long reference wavelengths is minor.

The differences between the OSIRIS Version 2.5 long wavelength and the ones tested lead to a maximum change in the mean retrieved profile of four percent between 20 and 35 km. The long reference wavelength trials were tested for consistency in the same manner as the short reference wavelengths. The most consistent long reference wavelengths are 667.97 nm and 680.06 nm.

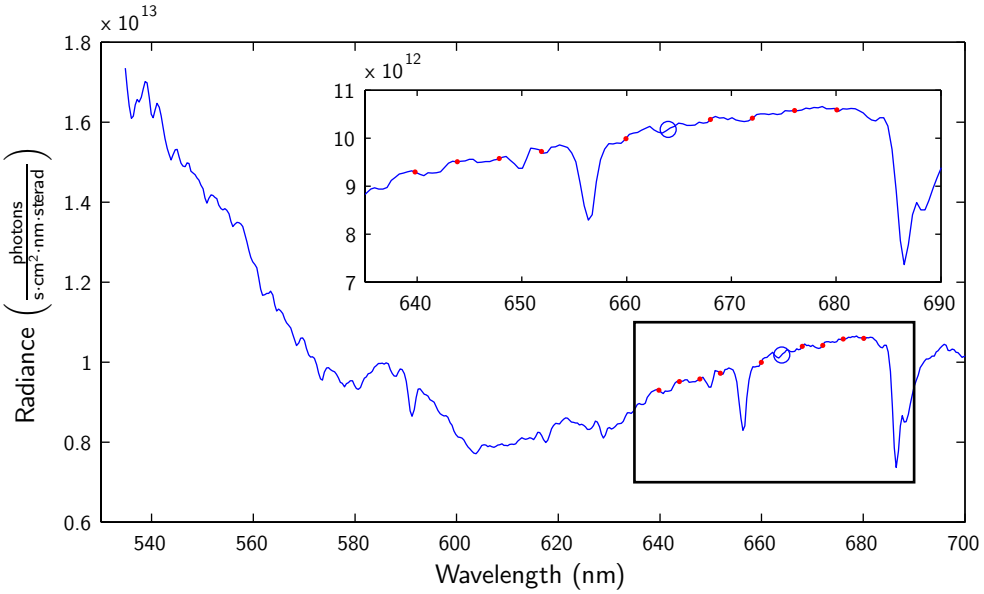

Figure 2.21: Selected long wavelength references on the 15 km OSIRIS Spectrum. Each red dot represents a wavelength that will be tested for use as the long wavelength in the CVT. The blue circle is the peak wavelength used in the OSIRIS Version 2.5 CVT. The inner plot is a magnification of the marked area.

2.5 New Triplets

Two new triplets that are formed from the most consistent short reference, peak, and long reference wavelengths determined previously have been investigated for use as a CVT. These triplets are given in Table 2.1 and are shown together with the original OSIRIS Version 2.5 CVT in Figure 2.23. The first triplet has the same short reference wavelength as the OSIRIS Version 2.5 CVT.

The average retrieved profile calculated using the two new triplets (Figure 2.23) is shown in Figure 2.24 together with the SAGE II average profile for comparison. Panel (b) shows that both of the new triplets produces an average profile that is as good as the average profile produced by the SaskMART algorithm using the OSIRIS

Table 2.1: Chappuis Vector Triplet Wavelengths.

	Triplet 1	**Triplet 2**
Short Reference Wavelength	540.24 nm	541.44 nm
Peak Wavelength	598.78 nm	599.58 nm
Long Reference Wavelength	667.97 nm	680.06 nm

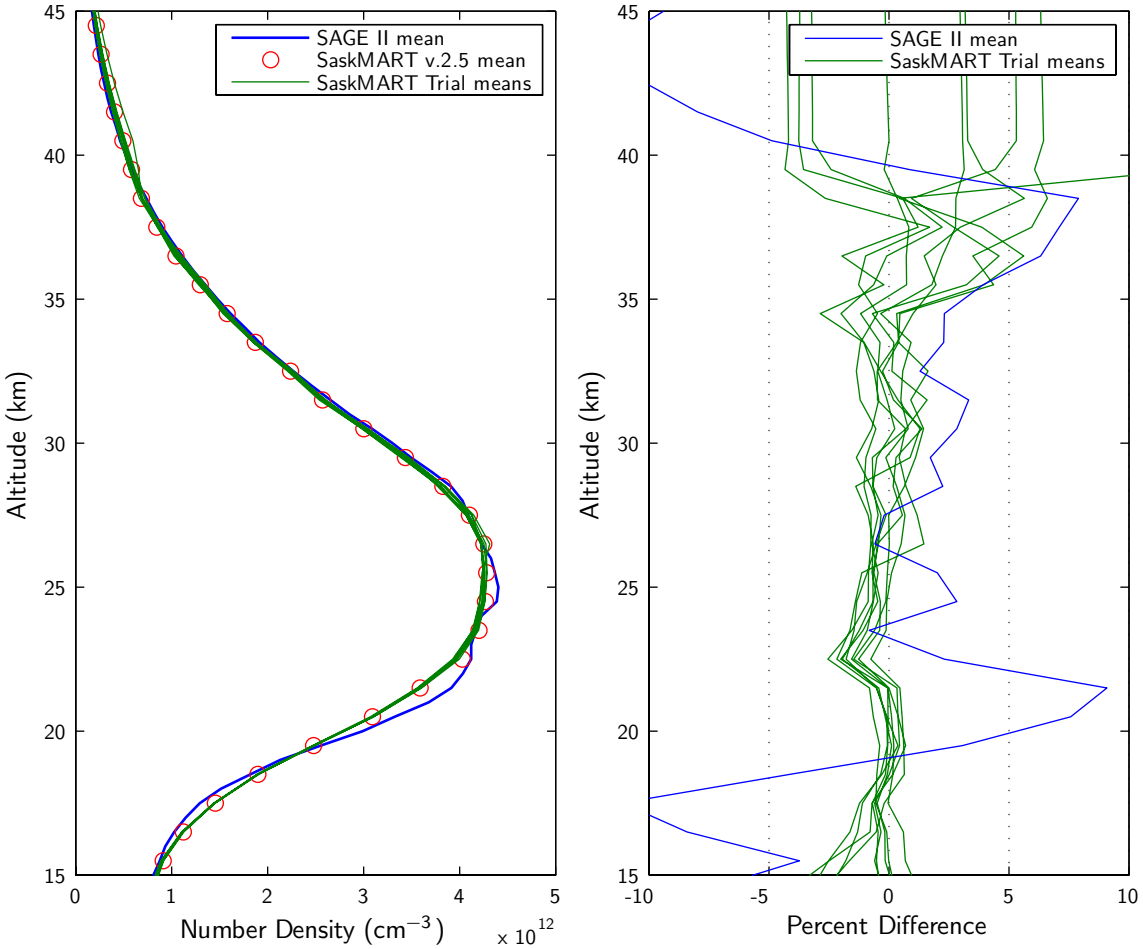

(a) Mean retrieved profile comparison.

(b) Percent difference.

Figure 2.22: Comparison of retrievals using the short reference and peak wavelengths of the OSIRIS Version 2.5 CVT with variable long reference wavelengths. The various long reference wavelengths produced similar profiles, to within four percent of the baseline OSIRIS Version 2.5 CVT between 20 and 35 km.

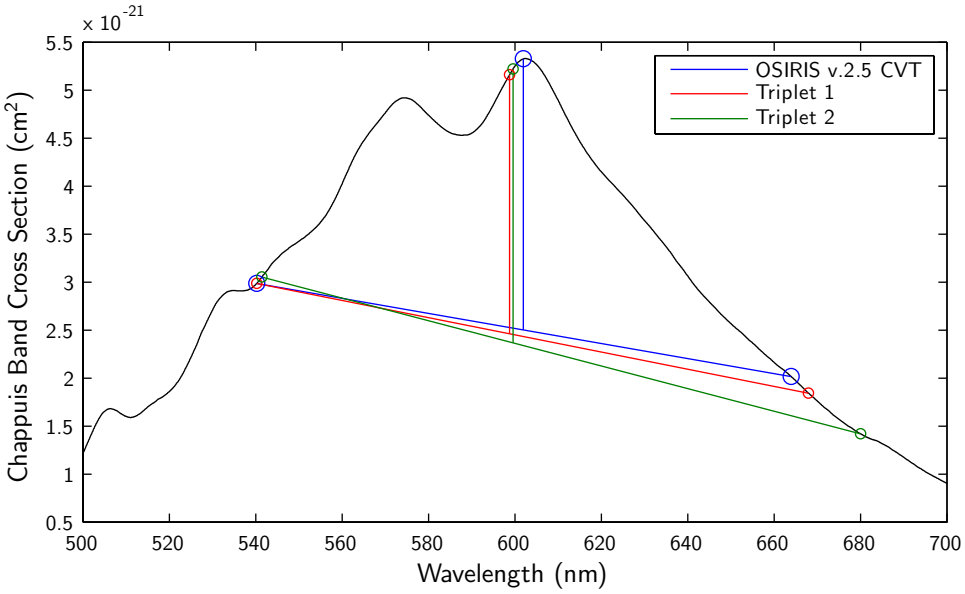

Figure 2.23: Two triplet combinations formed from the best short reference, peak, and long reference wavelengths identified in Section 2.4 compared with the original OSIRIS Version 2.5 CVT. The wavelength values are given in Table 2.1.

Version 2.5 CVT (compare Figure 2.24(b) with Figure 2.13(b)). There are two minor improvements in the mean retrieved profile. The first is that the retrieved ozone density at 21 km is not as low using the two new triplets as it is using the OSIRIS Version 2.5 CVT. The second is that the ozone density retrieved between 25 and 35 km is closer to SAGE II using the two new triplets than it is using the OSIRIS Version 2.5 CVT.

Figure 2.25 shows retrievals made from two of the scans. In both panels the general shape of the profiles is similar, although the retrievals from the different triplets show small scale structure superimposed on the profiles. This structure is not consistent between triplets, or scans, and represents noise in the vector retrieval. The differences are particularly noticeable at and above the ozone peak.

Practically every scan processed by the Chappuis-only SaskMART retrieval contains noise generated structure between 25 and 38 km. When the SaskMART retrieval reaches this altitude range, the trough in the Chappuis wavelengths, and therefore the Chappuis vector, has almost reduced to zero (see Figure 1.8). Because of this loss of information, the retrieved concentration contains larger errors.

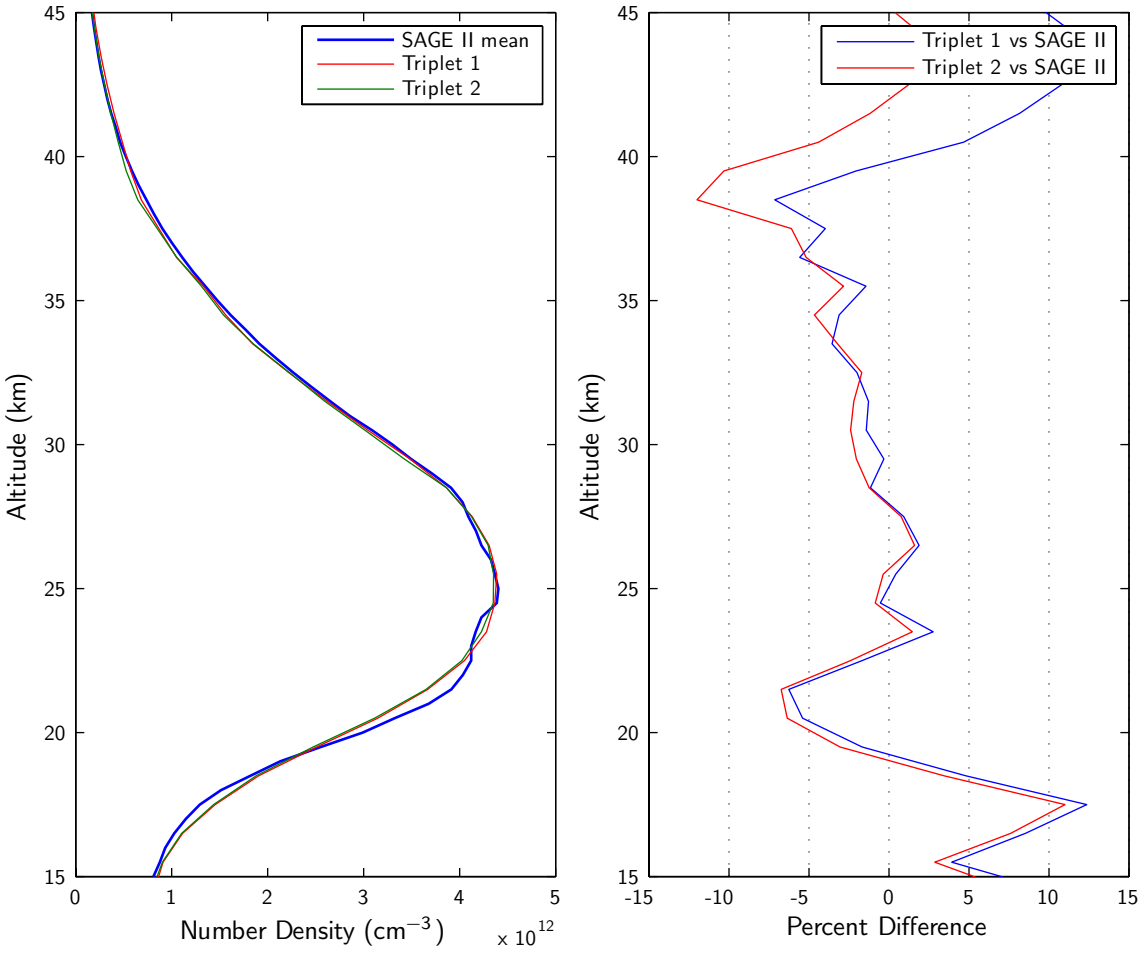

(a) Mean retrieved profile comparison.

(b) Percent difference.

Figure 2.24: The average retrieved profile found using the two new triplets compared with the SAGE II average profile.

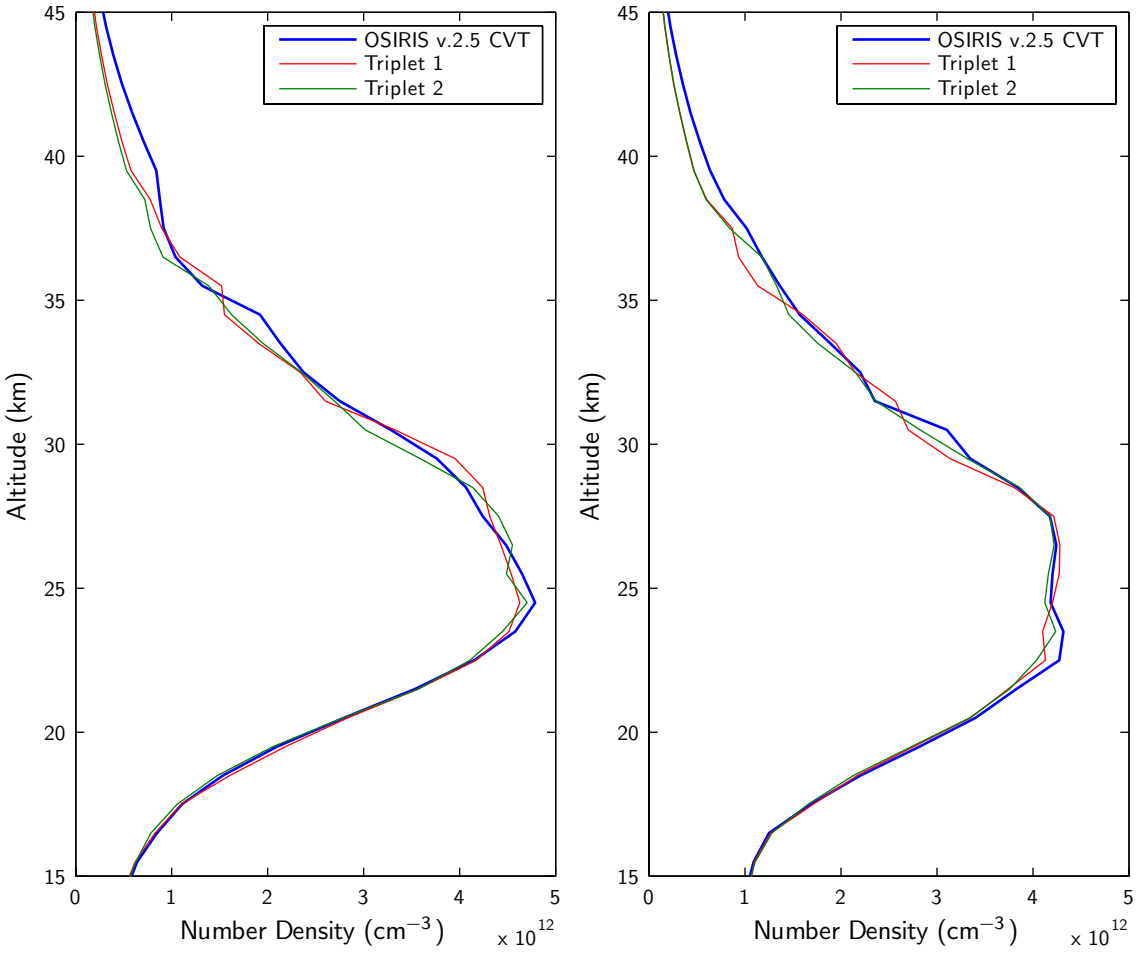

(a) Sample scan #1.

(b) Sample scan #2.

Figure 2.25: Sample single retrievals using the most consistent CVTs.

2.6 Using More Than One Triplet

Figure 2.26 shows the same two scans as Figure 2.25, except that in this case the triplets have been combined. Within the SaskMART retrieval, each triplet is weighted equally, *i.e.*, $W_{ik} = \frac{1}{2}$ for all i and k. This is not the same as retrieving two separate ozone density profiles and averaging them; although the results of equal weighting appear to be the same as averaging of the two profiles. Rather the two triplets are competing against and balancing the random noise contained in each other. The result is that the small scale structure is much less apparent. The combined triplet (blue curve) in Figure 2.26 is much smoother than either of the individual triplet retrievals (red and green curves).

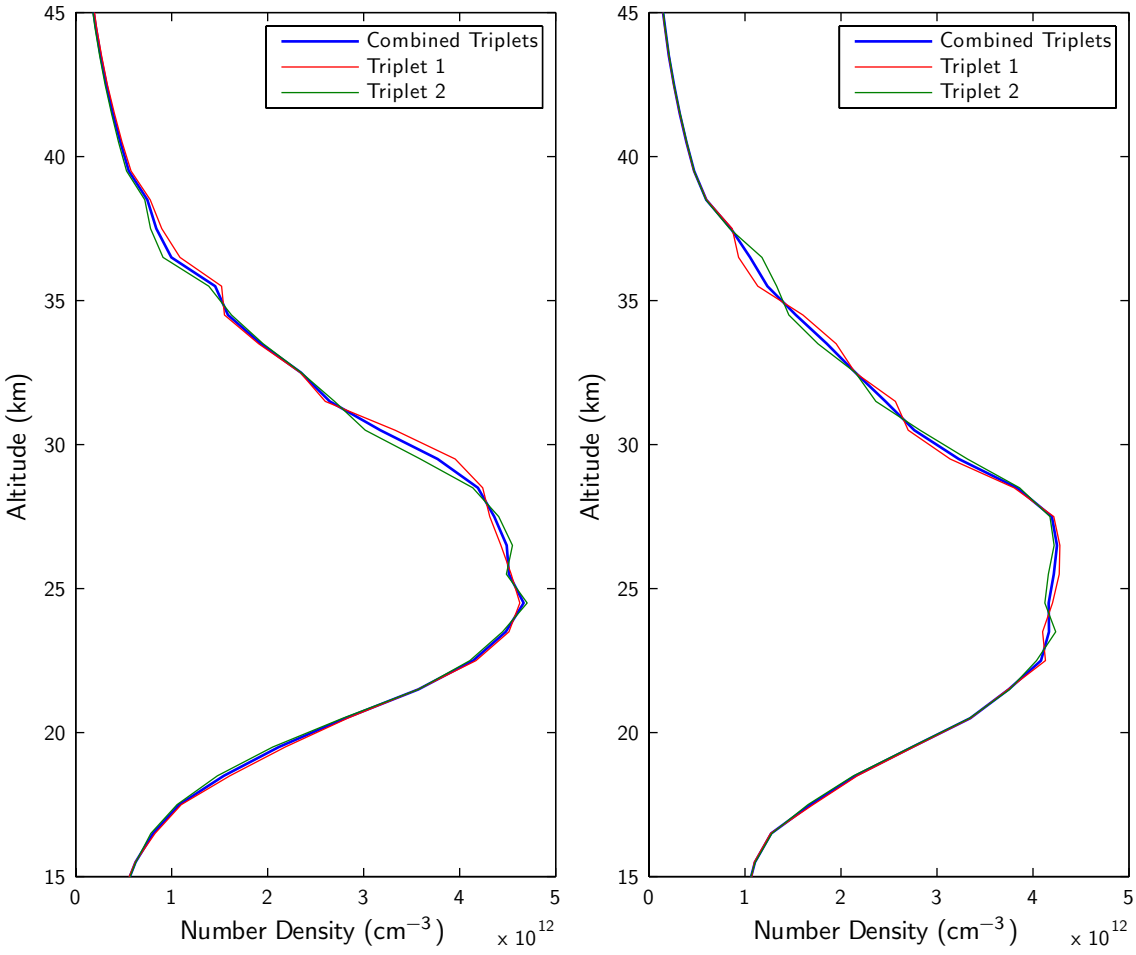

(a) Sample scan #1.

(b) Sample scan #2.

Figure 2.26: Sample single retrievals found using the two CVTs of Figure 2.23. The small scale structure seen in Figure 2.25 is almost eliminated.

Figure 2.27 is the mean retrieved profile using both CVTs in the SaskMART retrieval. In comparison with the mean profiles of the individual CVTs, the combined CVT mean profile is the average of the two. The results demonstrate that it is possible to weight multiple vectors and retrieve a meaningful ozone profile.

Using more than one triplet substantially reduces the noise introduced into the retrieval due to a single vector. In other words, structure that is real should be present in both vectors and so appear in the final retrieval; structure related to vector noise is likely to be reduced by the combination of vectors.

2.7 Additional Comparison Sets

Two other mean profile comparison sets are presented in this section, two seasonal comparison sets are also presented. These comparisons demonstrate that using the combined triplet method, the SaskMART retrieval technique compares well with SAGE II data for similar times and latitudes.

2.7.1 Second Comparison Set

The second comparison set uses data from summer in the northern hemisphere and is shown in Figure 2.28; specifically it is a two day, two degree bin centered at June 27, 2004, and 50°N latitude.

The result of the second comparison is shown in Figure 2.29. There are fewer scans in the SAGE II dataset than was used in the first comparison, this could account for the increase in small scale structure in the mean SAGE II profile. Despite this, the general agreement between the two mean profiles is obvious; the profiles agree to within seven percent from 16 to 36 km.

2.7.2 Third Comparison Set

The third comparison (Figure 2.30) also uses data from the northern hemisphere summer, but at a lower latitude than for the second comparison set. This comparison covers a two day, two degree bin centered at April 30, 2005, and 30°N latitude.

The results of the third comparison are shown in Figure 2.31. As for the second comparison set, the third set is also smaller than the first. The large standard deviation in ozone concentration below 20 km is not unusual; the variation of ozone

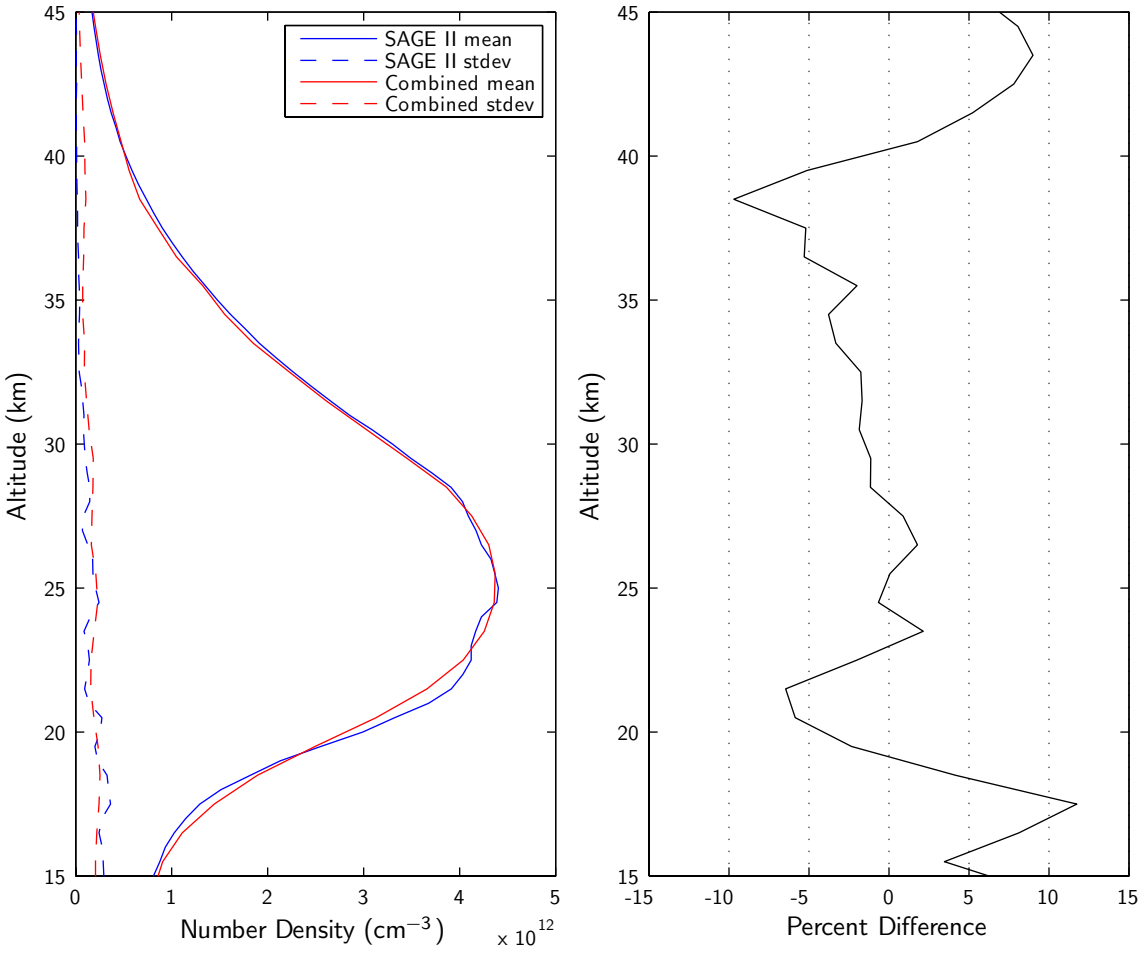

(a) Mean retrieved profile comparison.

(b) Percent difference.

Figure 2.27: Mean retrieval found by combining the two CVTs of Figure 2.23. The mean profile lies between the two individual profiles. Due to averaging, each of the mean profiles is devoid of small scale structure; although for individual scans, a combination of vectors yields a better result.

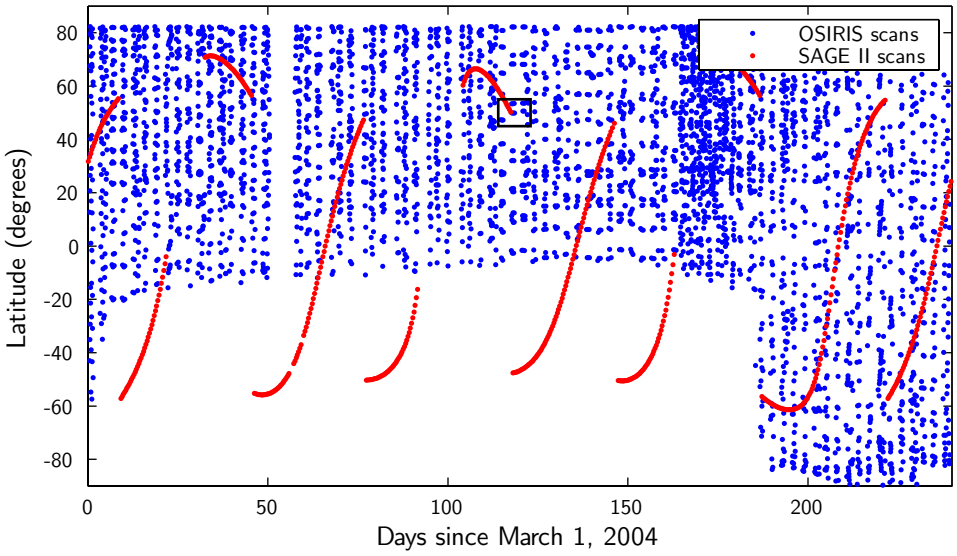

(a) OSIRIS and SAGE II scans for an eight month period starting March 1, 2004. The coincidence scans were taken from the area marked by the rectangle and enlarged in Panel (b).

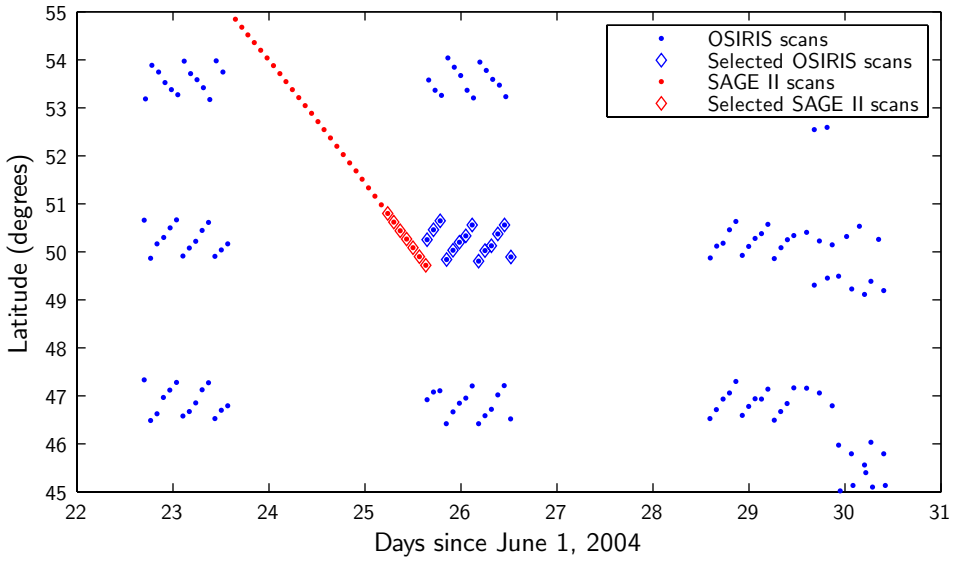

(b) Coincident OSIRIS and SAGE II scans used to compare and validate the retrieved ozone profiles. There are fourteen OSIRIS scans and seven SAGE II scans.

Figure 2.28: The second comparison set.

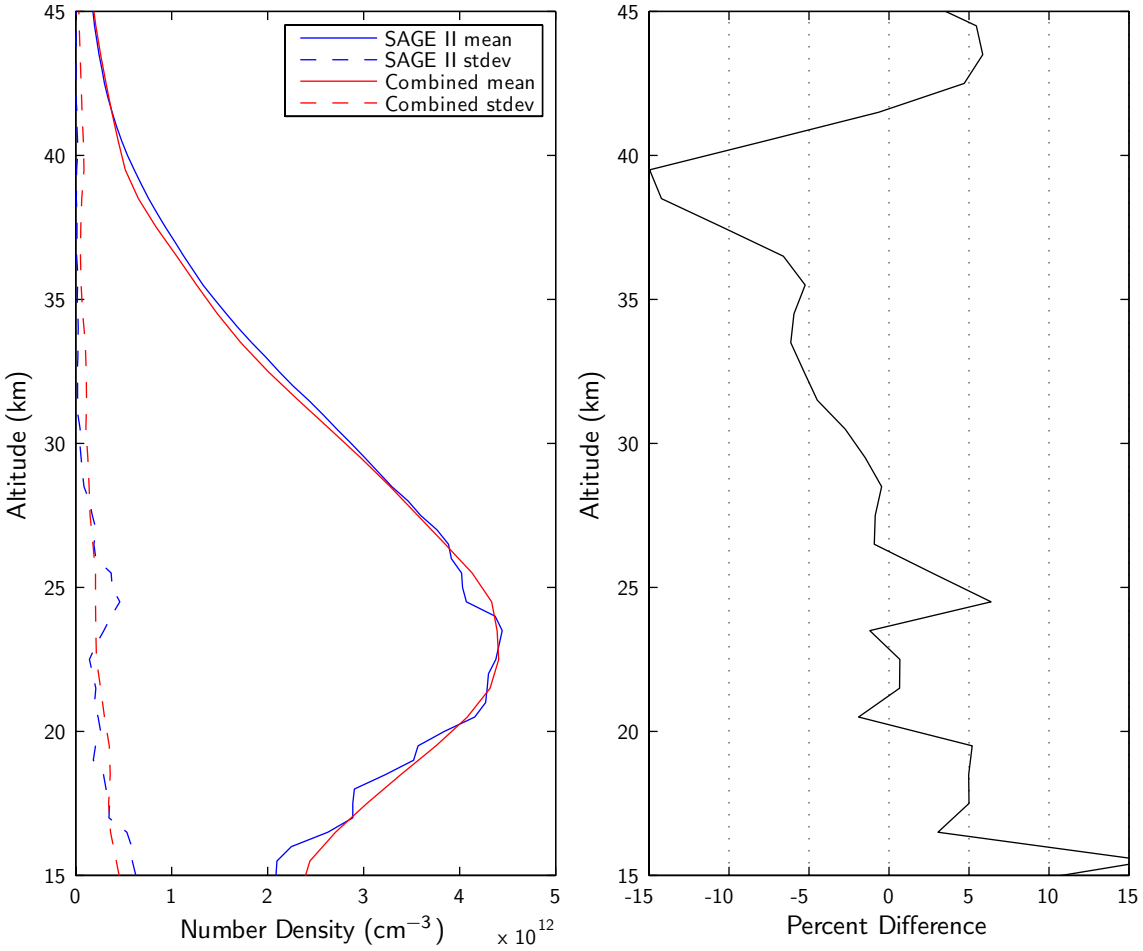

(a) Mean retrieved profile comparison.

(b) Percent difference.

Figure 2.29: Mean retrieval found from using both Chappuis triplets. The SaskMART mean profile agrees with the SAGE II mean profile to within seven percent between 16–36 km.

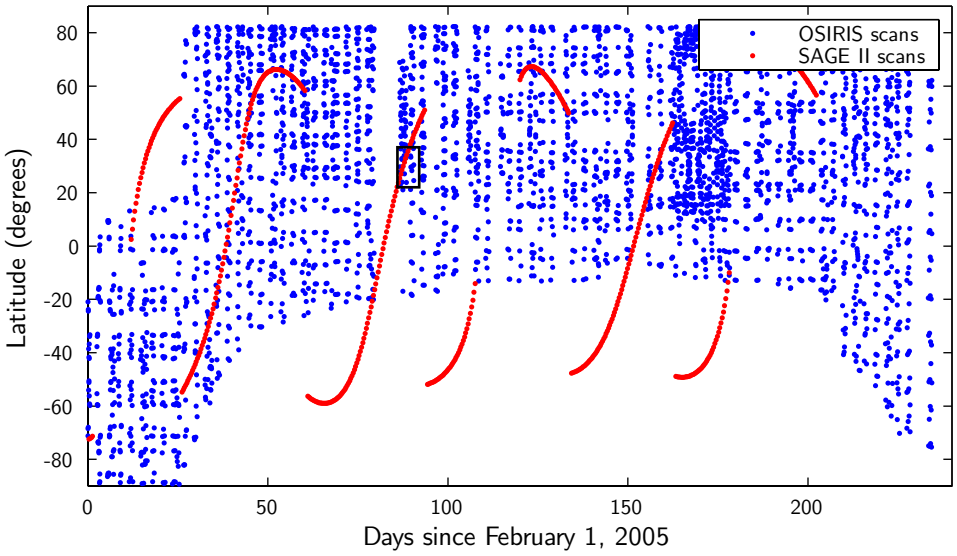

(a) OSIRIS and SAGE II scans for an eight month period starting February 1, 2004. The coincidence scans were taken from the area marked by the rectangle and enlarged in Panel (b).

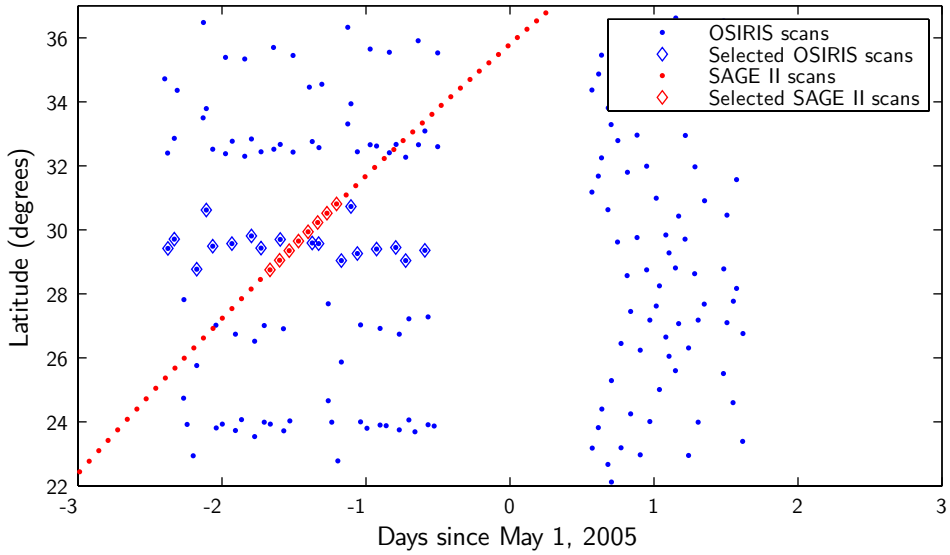

(b) Coincident OSIRIS and SAGE II scans used to compare and validate the retrieved ozone profiles. There are eighteen OSIRIS scans and eight SAGE II scans.

Figure 2.30: The third comparison set.

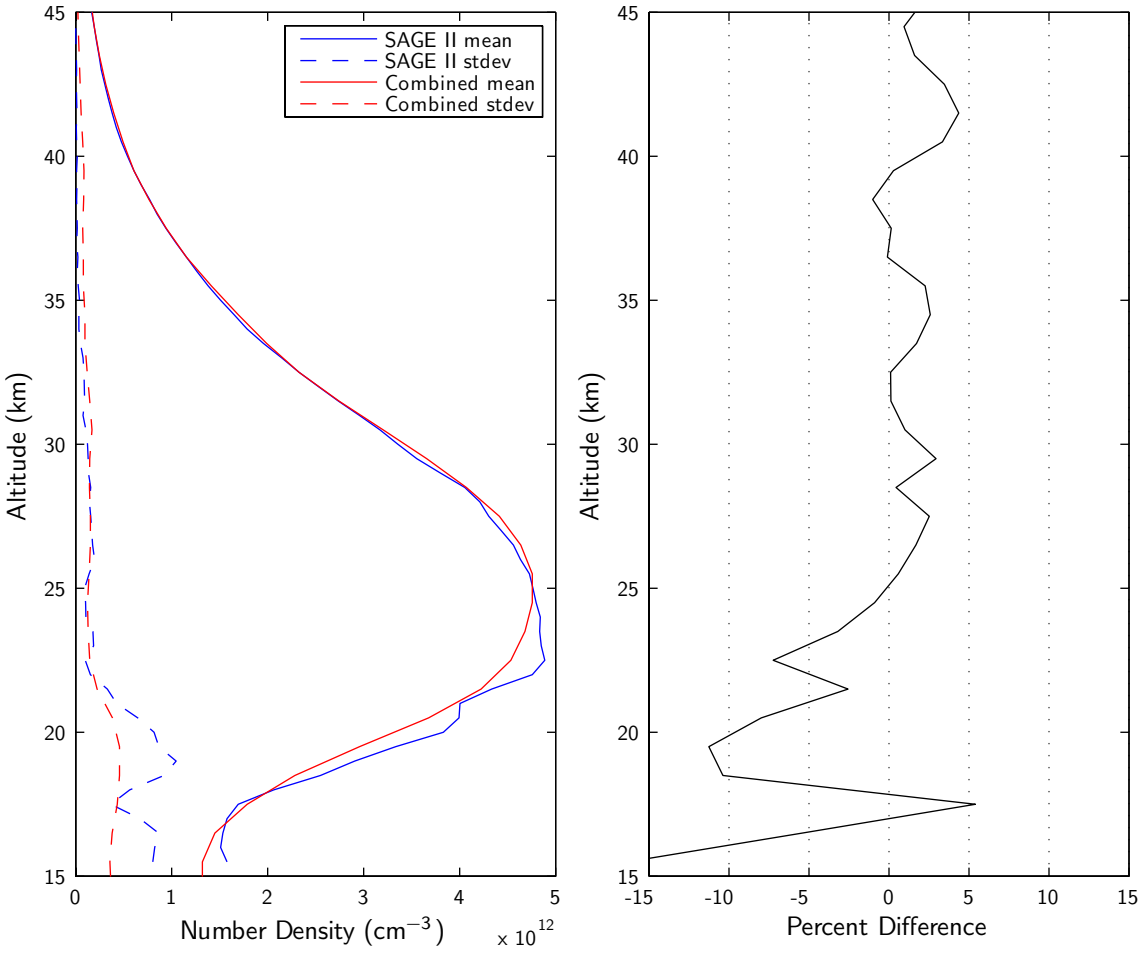

(a) Mean retrieved profile comparison.

(b) Percent difference.

Figure 2.31: Mean retrieval from by using both CVTs. The SaskMART mean profile agrees with the SAGE II mean profile to about five percent between 23 and 45 km.

density in the upper troposphere/lower stratosphere is larger than the variation in the middle and upper stratosphere. However, if the small scale features in the mean SAGE II profile at 20 and 22.5 km are ignored, the general agreement is again quite apparent. The profiles agree to about five percent from 23 to 45 km.

2.7.3 Seasonal Comparison Sets

In addition to the profile comparisons presented above, the ozone density calculated by SaskMART using the combined CVTs at a specific latitude and altitude have been tracked over time and compared with SAGE II at the same latitude and altitude. Each blue dot in Figures 2.32 and 2.33 represents the ozone density at 24.5

or 29.5 km (Panels (a) and (b), respectively) for a SAGE II scan; each red dot is an OSIRIS scan. Figure 2.32 shows a comparison of the two ozone products for a four-year period beginning in 2002 for 45°N. Figure 2.32 is a second comparison at 20°S. Both comparisons show that the ozone abundance at any given time agrees within the spread of the abundances. The seasonal trends in abundance mapped by both SAGE II and SaskMART agree at both latitudes and altitudes.

2.8 Retrieval Error

The last section in this chapter is concerned with an estimate of the error in the profiles retrieved by the SaskMART technique. The derivation of the error estimate follows the work of *Rodgers* (2000) and *Puliafito et al.* (1995). The retrieval of an ozone profile, $\hat{\mathbf{x}}$, can be regarded as a function of retrieval vectors, $\mathbf{y}$, an initial guess ozone profile, $\mathbf{x}_0$, and other factors, $\hat{b}$, such as Earth albedo and aerosol loading:

$$\hat{\mathbf{x}} = R(\mathbf{y}, \hat{b}, \mathbf{x}_0). \tag{2.4}$$

In this section, $\hat{\mathbf{x}}$ is used to denote the retrieved ozone profile and $\mathbf{x}$ is the true ozone profile that gives rise to the measurements $\mathbf{y}$. Similarly, $\hat{b}$ represents the best guess of other physical parameters used in the retrieval precess (Earth albedo, aerosol loading, *etc.*).

The retrieval vectors are a function of the physical ozone profile as well as other factors, b, and instrument error, ϵ:

$$\mathbf{y} = f(\mathbf{x}, b) + \epsilon. \tag{2.5}$$

In the above equation, f, represents the physics of the real atmosphere and b, the real atmospheric parameters (as opposed to $\hat{b}$).

Combining Equations 2.4 and 2.5 yields the transfer equation,

$$\hat{\mathbf{x}} = R\big(f(\mathbf{x}, b) + \epsilon, \hat{b}, \mathbf{x}_0\big). \tag{2.6}$$

Thus the retrieved ozone profile, $\hat{\mathbf{x}}$, relates to the actual (true) ozone profile, $\mathbf{x}$, through two separate processes, one computational, R, and one physical, f.

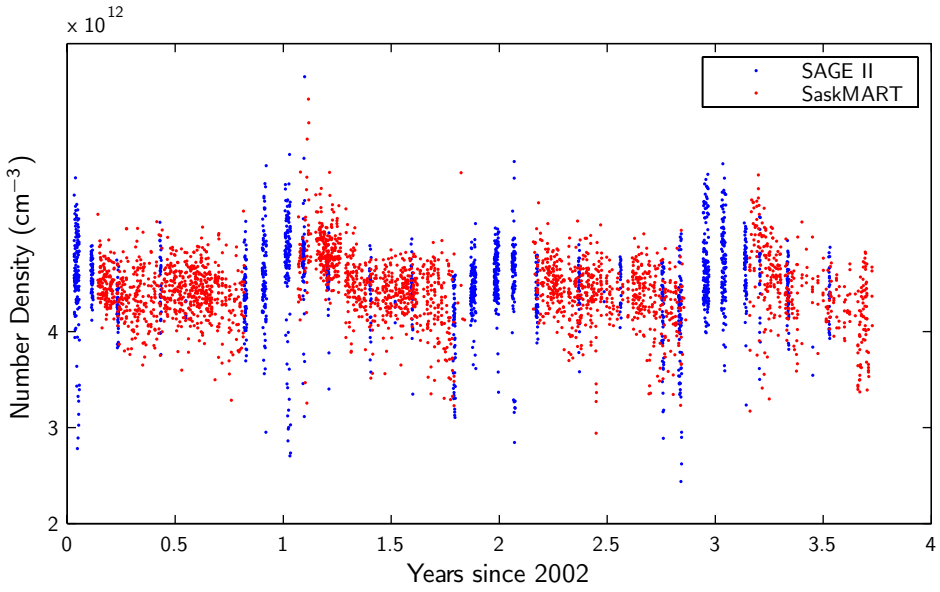

(a) Density of ozone at 24.5 km.

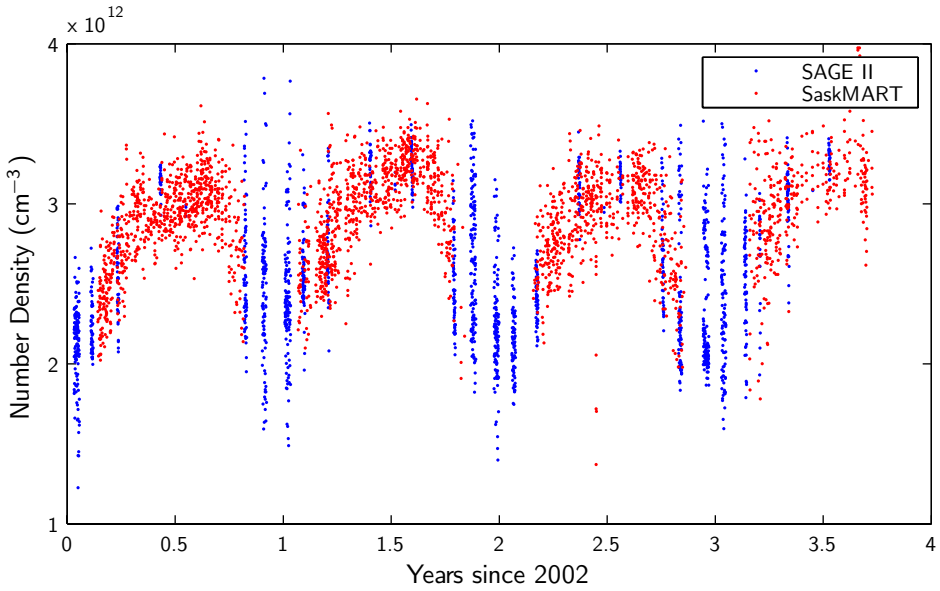

(b) Density of ozone at 29.5 km.

Figure 2.32: SaskMART and SAGE II ozone number densities at 45°N, all longitudes, over a four-year period at two different altitudes. There is general agreement in the variability and seasonal trends.

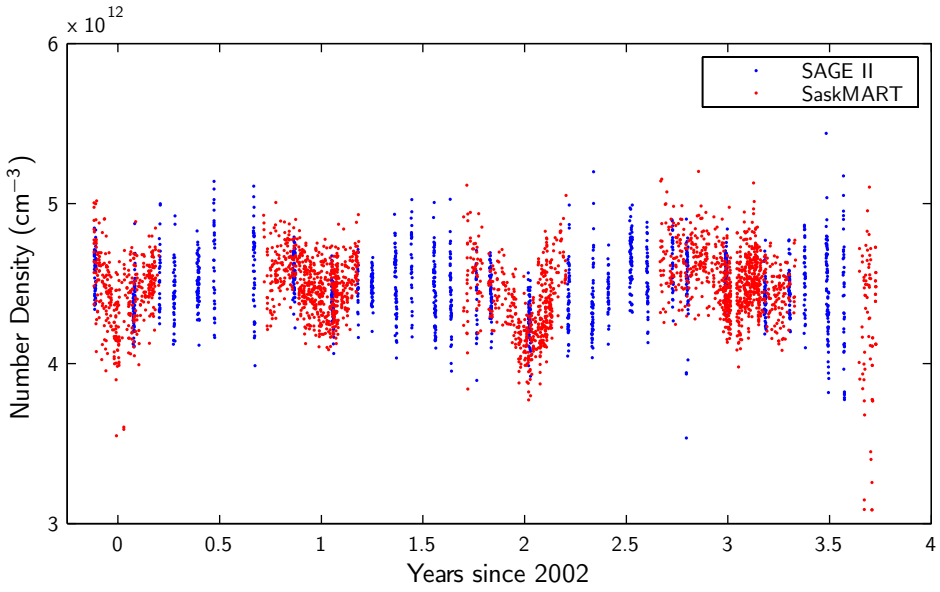

(a) Density of ozone at 24.5 km.

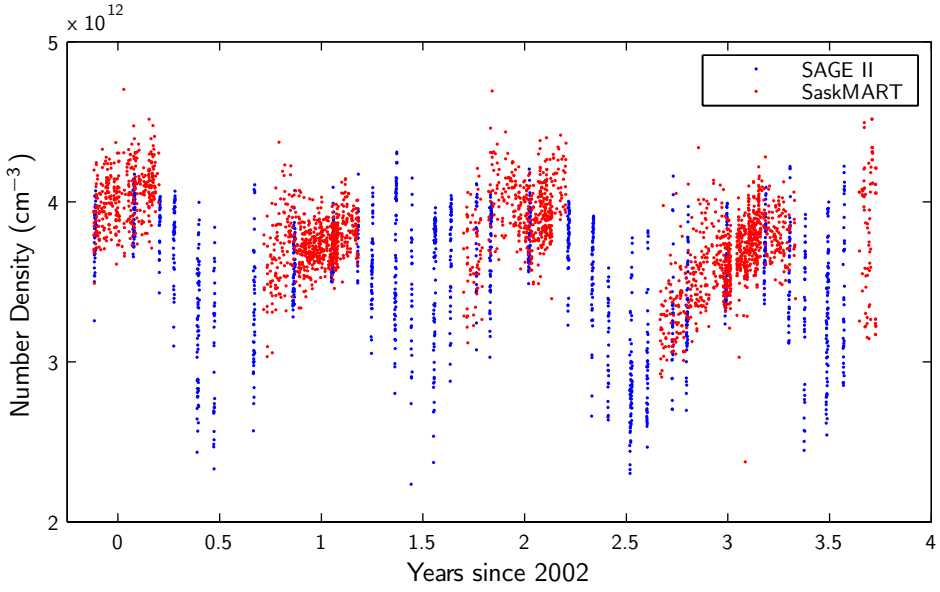

(b) Density of ozone at 29.5 km.

Figure 2.33: SaskMART and SAGE II ozone number densities at 20°S, all longitudes, over a four-year period at two different altitudes. There is general agreement in variability and seasonal trends.

2.8.1 Linearization of the Transfer Equation

Because f and b can not be known exactly, they are replaced by a model atmosphere, F, and best guess physical parameters, $\hat{b}$. That is,

$$F(\mathbf{x}, \hat{b}) \cong f(\mathbf{x}, b). \tag{2.7}$$

Combining Equations 2.4 and 2.7 shows that the computed profile, $\hat{\mathbf{x}}$, in terms of a simulated physical profile, $\mathbf{x}$, the *a priori*, and other parameters, $\hat{b}$.

$$\hat{\mathbf{x}} = R\big(F(\mathbf{x}, \hat{b}) + \epsilon, \hat{b}, \mathbf{x}_0\big) \tag{2.8}$$

The next step is to linearize the forward model represented by Equation 2.8 with $\mathbf{x}$ centered at the *a priori* ozone profile, $\mathbf{x}_0$, and the other parameters, b, centered at the best guess, $\hat{b}$. This expansion yields:

$$\hat{\mathbf{x}} = R\Big(F(\mathbf{x}_0, \hat{b}) + \frac{\partial F(\mathbf{x} - \mathbf{x}_0)}{\partial \mathbf{x}} + \frac{\partial F(b - \hat{b})}{\partial b} + \epsilon, \hat{b}, \mathbf{x}_0\Big) \tag{2.9}$$

where $\frac{\partial F}{\partial \mathbf{x}}$ relates changes in the ozone profile, $\mathbf{x}$, to changes in the forward model and $\frac{\partial F}{\partial b}$ relates changes in the other modelled parameters, b, to changes in the forward model; quantities that Rodgers refers to as $\mathbf{K}_x$ and $\mathbf{K}_b$, respectively. Thus, Equation 2.9 becomes:

$$\hat{\mathbf{x}} = R\big(F(\mathbf{x}_0, \hat{b}) + \mathbf{K}_x(\mathbf{x} - \mathbf{x}_0) + \mathbf{K}_b(b - \hat{b}) + \boldsymbol{\epsilon}, \hat{b}, \mathbf{x}_0\big). \tag{2.10}$$

where,

$$F(\mathbf{x}_0, \hat{b}) + \mathbf{K}_x(\mathbf{x} - \mathbf{x}_0) + \mathbf{K}_b(b - \hat{b}) + \boldsymbol{\epsilon} \tag{2.11}$$

is the modelled retrieval vectors linearized about $\mathbf{x} = \mathbf{x}_0$ (see Equation 2.5). If the inverse function of Equation 2.10 is now linearized about $\mathbf{x}_0$, the transfer function becomes:

$$\hat{\mathbf{x}} = R\big(F(\mathbf{x}_0, \hat{b}), \hat{b}, \mathbf{x}_0\big) + \frac{\partial R}{\partial \mathbf{y}}\Big(\mathbf{K}_x(\mathbf{x} - \mathbf{x}_0) + \mathbf{K}_b(b - \hat{b}) + \boldsymbol{\epsilon}\Big). \tag{2.12}$$

where $\frac{\partial R}{\partial \mathbf{y}}$ relates changes in the radiance vectors, $\mathbf{y}$, to changes in the retrieval; Rodgers refers to this quantity as $\mathbf{G}_y$. Re-arranging Equation 2.12 into groups yields,

$$\hat{\mathbf{x}} = R\big(F(\mathbf{x}_0, \hat{b}), \hat{b}, \mathbf{x}_0\big) \ldots \qquad \text{bias} \tag{2.13a}$$

$$+ \mathbf{G}_y\mathbf{K}_x(\mathbf{x} - \mathbf{x}_0) \ldots \qquad \text{smoothing} \tag{2.13b}$$

$$+ \mathbf{G}_y\mathbf{K}_b(b - \hat{b}) \ldots \qquad \text{parameter error} \tag{2.13c}$$

$$+ \mathbf{G}_y(\boldsymbol{\epsilon}) \qquad \text{retrieval noise error} \tag{2.13d}$$

Each of the error terms of Equation 2.4 are considered below.

2.8.2 Bias

The bias term represents the drift in the ozone profile after it has passed through both the forward and inverse models. Ideally these two functions are simple inverses of each other such that the ozone profile, $\mathbf{x}$, that leads to the radiance vectors, $\mathbf{y}$, through the forward model, is identical to the ozone profile, $\hat{\mathbf{x}}$, retrieved by the radiance vectors, $\mathbf{y}$, through the SaskMART inversion.

Figure 2.34(a) shows three sample ozone profiles that have been operated on by Equation 2.13a. The sample ozone density profiles, $\mathbf{x}$, used to model the radiances are represented by the dashed lines and their corresponding retrieved ozone density profiles, $\hat{\mathbf{x}}$, are given by the solid lines. The same initial guess ozone profile, $\mathbf{x}_0$, is used for all three retrievals. The radiance vectors were calculated for the tangent altitudes shown by the vertical black dashed lines. The altitudes that were taken from OSIRIS data show the vertical resolution of the Optical Spectrograph data. Outside the retrieval altitude extremes (9 km and 38 km), there is no data and the retrieved profiles merge with the initial guess after they have been scaled to the same value as the concentration at the lowermost or uppermost retrieved altitude (see §2.2.5).

The change in the retrieved profile, $\hat{\mathbf{x}}$, from the profile used to generate the radiances, $\mathbf{x}$, at both the lower and higher altitudes depends on the difference in shape between $\mathbf{x}$ and the initial guess profile, $\mathbf{x}_0$. The retrieval process does not change the shape of the retrieved profile outside the retrieval extremes, only its magnitude. When the shapes are identical, as in Profile 1, there is negligible change in the retrieved profile. Profiles 2 and 3 show that the merge can adversely affect the retrieved profile at a couple of retrieval altitudes on both ends of the profile.

After the merging effects have dissipated, the two ozone profiles ($\mathbf{x}$ and $\hat{\mathbf{x}}$) agree to a difference of two percent on average (Panel (b)). The magnitude of the difference, due to a lack of information, is understandable. Thus the bias error can be taken as two percent over the entire altitude range of the retrieval with an additional three percent added to the concentrations at the lowest two altitudes (12 km and below) and highest two altitudes (36 km and above).

2.8.3 Smoothing

Expanding $\mathbf{G}_y\mathbf{K}_x$ gives,

$$\mathbf{G}_y\mathbf{K}_x = \frac{\partial R}{\partial \mathbf{y}} \cdot \frac{\partial F}{\partial \mathbf{x}} = \frac{\partial \hat{\mathbf{x}}}{\partial \mathbf{y}} \cdot \frac{\partial \mathbf{y}}{\partial \mathbf{x}} = \frac{\partial \hat{\mathbf{x}}}{\partial \mathbf{x}} = \mathbf{A} \tag{2.14}$$

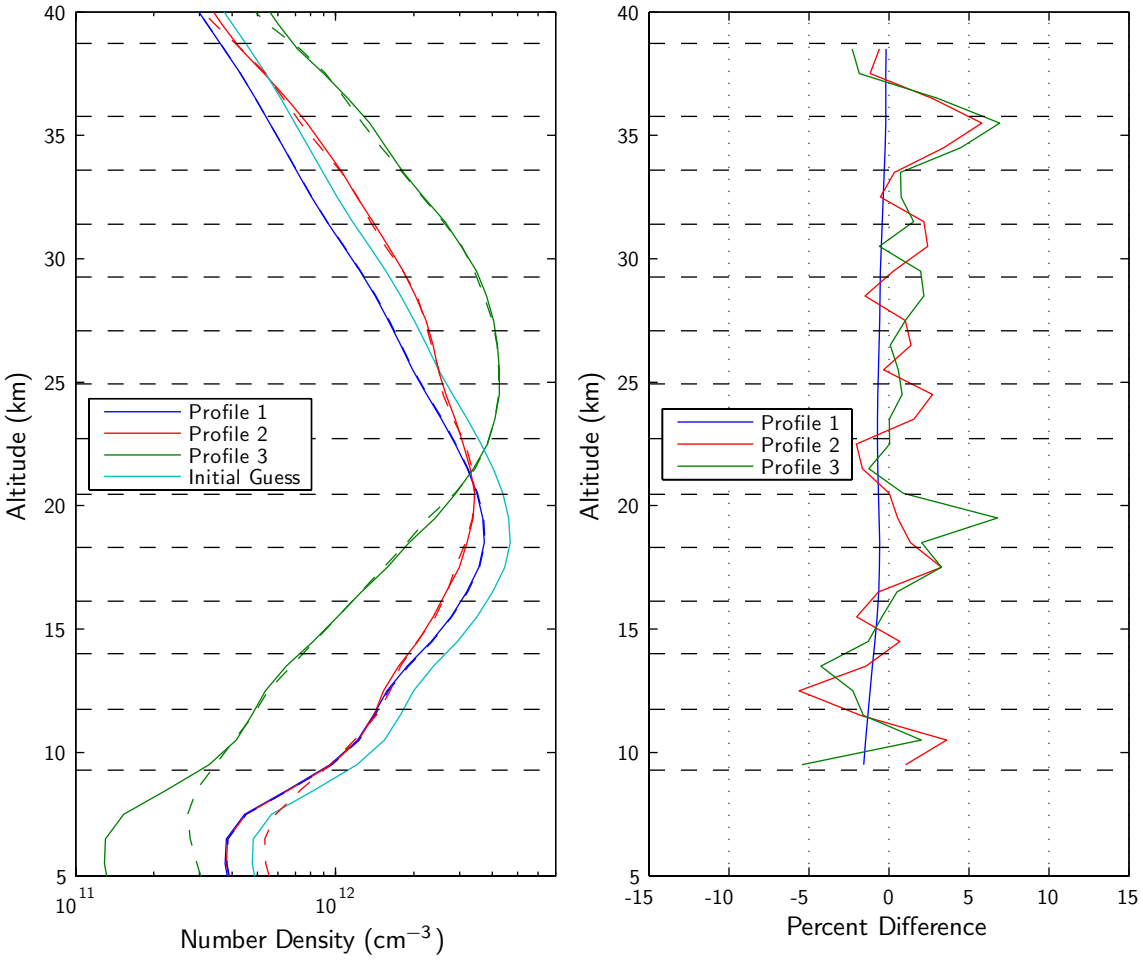

(a) Three sample ozone profiles used to characterize the bias of the SaskMART ozone retrieval. The dashed lines are sample ozone profiles used to generate radiances for the retrieved ozone density profiles (the solid lines). The initial guess profile used in each of the retrievals is also shown. The horizontal black dashed lines show the tangent altitudes used for the retrieval and are typical for the OSIRIS instrument.

(b) The percent difference between the sample profiles used to generate radiances and the retrieved profiles shown in Panel (a). Below the lowest retrieval altitude and above the highest retrieval altitude, the retrieved profile merges with the shape of the initial guess profile.

Figure 2.34: Three ozone density profiles showing the SaskMART retrieval bias.

where $\mathbf{A}$, the averaging kernel, is the change in the retrieved ozone profile with respect to a change in the initial guess ozone profile. Ignoring the bias term and re-arranging Equation 2.13 gives,

$$\hat{\mathbf{x}} = \mathbf{A}\mathbf{x} + (\mathbf{I} - \mathbf{A})\mathbf{x}_0 + \mathbf{G}_y\mathbf{K}_b(b - \hat{b}) + \mathbf{G}_y\boldsymbol{\epsilon}, \tag{2.15}$$

At its core, the SaskMART retrieval technique uses a modified Chahine inversion technique, which, according to *Puliafito et al.* (1995) means that the averaging kernel, $\mathbf{A}$, is negligibly different from the identity matrix given sufficient iterations of the Chahine inversion. Hence, Equation 2.15 becomes,

$$\hat{\mathbf{x}} - \mathbf{x} = \mathbf{G}_y\mathbf{K}_b(b - \hat{b}) + \mathbf{G}_y\boldsymbol{\epsilon}. \tag{2.16}$$

Therefore, the only remaining effects that contribute to the error in the retrival relate to the parameters, b, and the retrieval noise error, ϵ.

2.8.4 Parameter Error

Both the parameter error and the retrieval noise error depend on the determination of the vector/retrieval kernel $\mathbf{G}_y$. This is found by varying the vectors one at a time and computing the corresponding changes in the retrieved ozone profile. Figure 2.35 plots the vector/retrieval kernel. Each line in the plot represents the change in the retrieved ozone density due to a change in the retrieval vectors at a given altitude.

Figure 2.35 shows that when the retrieval vector at a given altitude is increased the ozone concentration at the corresponding altitude also increases. A positive change in the retrieval vector also increases the amount of ozone at higher altitudes and decreases the amount of ozone at lower altitudes although to a lesser extent. The increase at higher altitudes is explained by noting that the line of sight radiances that make up the retrieval vector pass through these higher altitudes; thus their ozone concentrations are also increased. The decrease in ozone concentrations at lower altitudes is reasoned in a similar manner; that is, for the vector at a lower altitude to remain constant while the vector above increases, the ozone concentration at that altitude must decrease.

Once the vector/retrieval kernel calculation is made, the parameter/vector kernels are calculated for the different parameters used in the SaskTRAN model. Specifically, the parameters that are tested are: the Earth albedo and aerosol loading. For simplification purposes a kernel is calculated separately for each parameter.

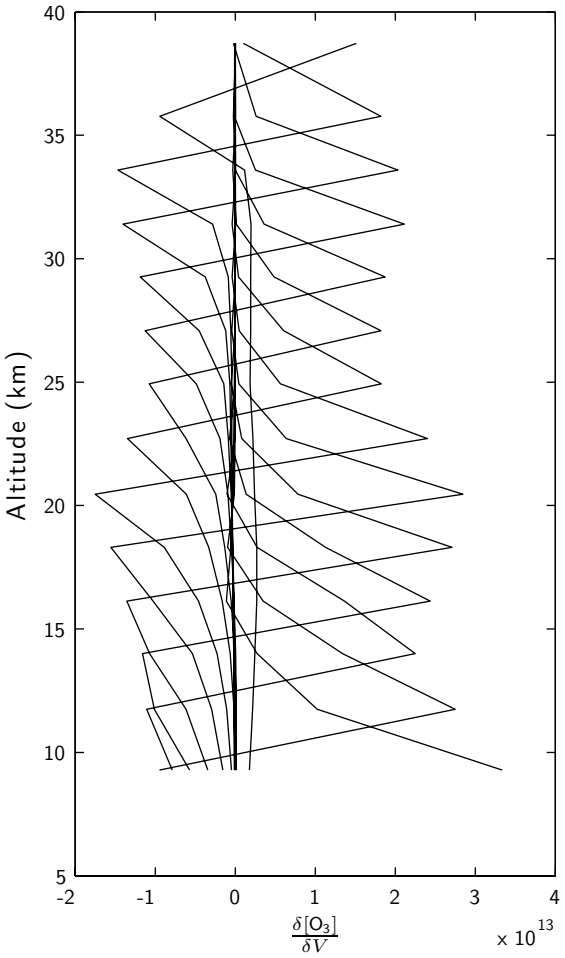

Figure 2.35: The vector/retrieval kernel, $\mathbf{G}_y$, shows the effects in the ozone retrieval caused by making small changes in the retrieval vectors.

Earth Albedo

As indicated in Figure 2.7, the retrieval vector at 15 km exhibits a slight increase with an increase in Earth albedo; this shows that the albedo error propagates an error on to the ozone retrieval. Figure 2.36(b) shows the amount of error present in the ozone retrieval due to an error in the albedo factor. The albedo used in the SaskMART ozone density retrieval is also a retrieved parameter; the error in the albedo is taken as 0.1 (*Bourassa et al.*, 2006).

Figure 2.36(b) shows that the amount of error introduced in the retrieval, due to variation in the albedo, peaks at around 0.10% at 15 km. This is a typical albedo error profile and is negligible compared to the bias error discussed in Section 2.8.2 and the instrument error discussed in Section 2.8.6.

Aerosol Load

According to Figure 2.8, the retrieval vector at 15 km shows a slight increase with an increase in the aerosol loading. The error in the amount of aerosol used in the model propagates an error on to the ozone retrieval. Figure 2.36(b) shows the amount of error in the ozone retrieval that is due to the error in the aerosol load. The aerosol profile is also retrieved in the SaskMART technique and is taken to be accurate to within 30% (*Bourassa et al.*, 2006).

The 30% error attributed to the aerosol load translates into an error of less than half a percent in the retrieved ozone profile according to Figure 2.36(b). The change in the amount of ozone is largest at lower altitudes, where the aerosol loading is the largest. As for the albedo error, this is a typical aerosol error profile. The contribution of this error to the total error is negligible and accounts for less than half a percent to the total error.

2.8.5 Pointing Error

The pointing information of the satellite, *i.e.*, the direction in which the instrument is looking, leads to a maximum error in the tangent altitude registration of 200 m. Although this error is not a parameter error, the effects of the pointing error can be calculated by changing the tangent altitudes of the retrieval and calculating the resultant difference in retrieval vector; this approach is the same as that for a parameter error.

The 200 m pointing error of the Optical Spectrograph results in an error that is always less than one percent and is greatest at the lowest tangent altitudes; this is shown in Figure 2.36(b). Again, this is a typical amount of error and like the albedo and aerosol errors, it is negligible and contributes less than half a percent to the total error.

2.8.6 Retrieval Noise Error

Unlike the other sources of error that affect the retrieval vectors indirectly through the forward model (the K matrices), the retrieval vector noise is measurement error in the measured radiances that make up the retrieval vector, $\mathbf{y}$. The covariance of the retrieval noise is:

$$\mathbf{S}_m = \mathbf{G}_y \mathbf{S}_\epsilon \mathbf{G}_y^T. \tag{2.17}$$

where,

$$\mathbf{S}_\epsilon = \begin{pmatrix} \epsilon_1^2 & 0 & \cdots & 0 \\ 0 & \epsilon_2^2 & \cdots & 0 \\ \vdots & \vdots & \ddots & \vdots \\ 0 & 0 & \cdots & \epsilon_n^2 \end{pmatrix}. \tag{2.18}$$

Each of the constituent errors in $\mathbf{S}_\epsilon$ is the error in the retrieval vector at a specific altitude. These errors are calculated from a differentiation of the error in the vector in terms of the radiances that make up each vector. For example, the Chappuis Vector Triplet formed according to Equation 2.1 has a corresponding error,

$$\sqrt{\left(\frac{1}{2}\cdot\frac{\mathrm{d}I_s}{I_s}\right)^2 + \left(\frac{1}{2}\cdot\frac{\mathrm{d}I_l}{I_l}\right)^2 + \left(\frac{\mathrm{d}I_p}{I_p}\right)^2}, \tag{2.19}$$

Figure 2.36(b) shows the results of using the calculated vector errors in Equation 2.17. The size of the error varies with altitude; it is less than three percent between 0 and 20 km, then increases gradually to about 12% at 35 km.

2.8.7 Total Error

The total variance of the SaskMART retrieval technique is the sum of the individual variances and results in the "total" error plotted in Figure 2.36(b). Figure 2.36(a) shows the error bars on the retrieved ozone concentration for the scan used to compute the typical error profiles.

The resultant error profile is almost completely determined by the retrieval vector noise above 30 km. Between the third retrieval tangent height (14 km) and 30 km, the error profile is a combination of bias error and retrieval vector noise. The lowest two retrieval tangent heights have an error of approximately five percent (the value of the bias error).

The error in the retrieval vector is a simple calculation that can be be made at the same time as the ozone profile calculation. However, the vector/retrieval kernel $\mathbf{G}_y$ is computationally too expensive to calculate for each scan in the OSIRIS dataset. The compromise is to use a generic vector/retrieval kernel with the calculated retrieval vector errors to estimate the retrieval vector error for each scan. This can be added to the bias error to give the total error bar. The other sources of error are so minor compared to these that they are not calculated.

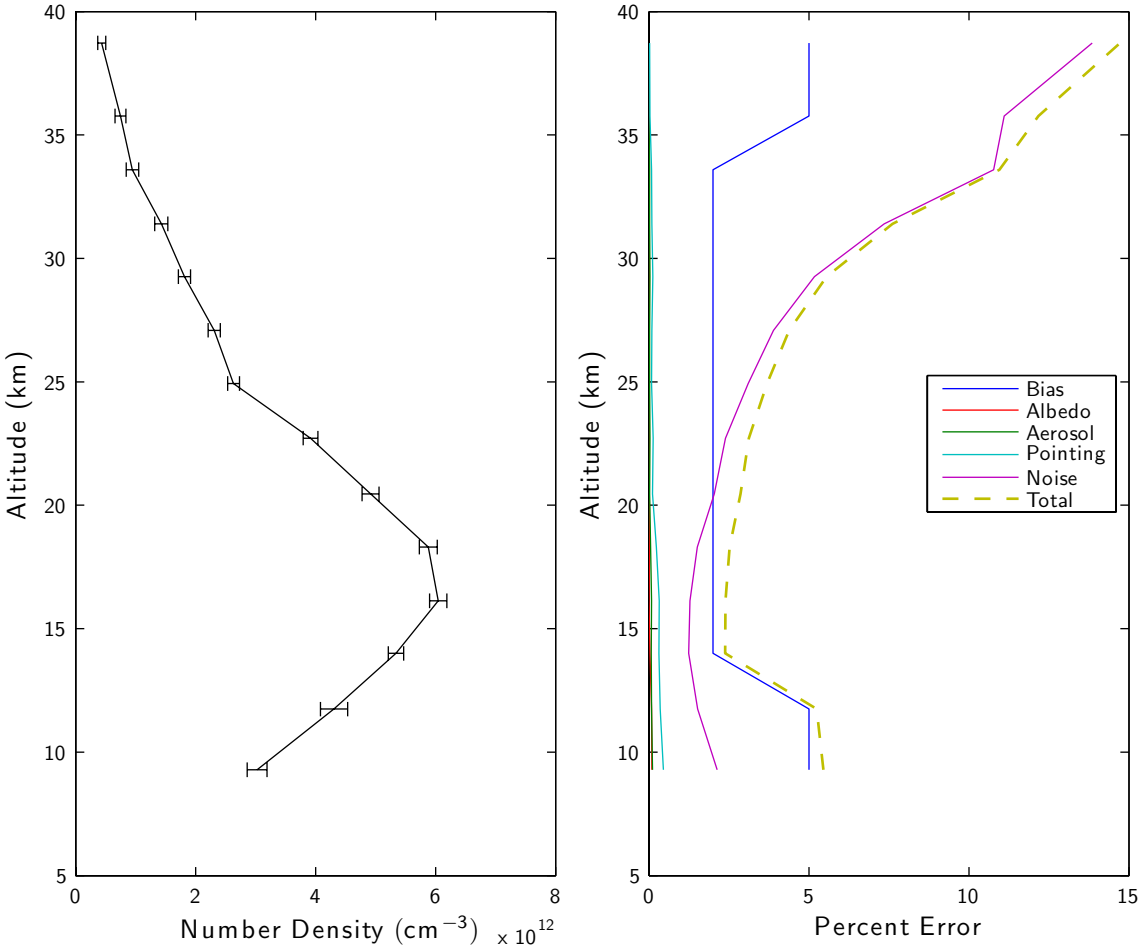

(a) Retrieved profile with error.

(b) Percent difference.

Figure 2.36: A sample OSIRIS scan with error bars denoting the total error and the errors due to the different error sources.

2.9 Conclusion

The MART technique outlined in Section 1.9.4 has been implemented using the SaskTRAN radiative transfer model and vectors from the radiance measurements of the Chappuis absorption feature to produce ozone density profiles. Initially the CVT used in the retrieval algorithm was the same as that used in the OSIRIS Version 2.5 ozone product. The SaskMART ozone density profiles were compared with OSIRIS Version 2.5 and SAGE II profiles using the CVT that showed good results (§ 2.3.3, Figure 2.13). Different radiances were tested for use in the CVTs (Section 2.4). This led to the formation of new triplets as demonstrated in Section 2.5. The wavelengths used to form the new triplets are: 540.24, 598.78 & 667.97 nm and 541.44, 599.58 & 680.06 nm. The SaskMART retrieval was modified in Section 2.6 to use two CVTs instead of one. The result was a retrieval that was more stable and tolerant of noise (Figure 2.27). Other comparison sets were presented in Section 2.7 and an error analysis was performed on the SaskMART ozone density profiles (Section 2.8).

The ability of the SaskMART retrieval technique to retrieve ozone density profiles between 10 and 40 km using only radiance data from the Chappuis band has been demonstrated in this chapter. The ozone density profiles calculated in this manner compare well with the ozone products of OSIRIS Version 2.5 and SAGE II. The Chappuis Vector Triplets investigated in this chapter can be used together with new vectors formed with radiance measurements in the blue end of the spectrum to increase the altitude range of the retrievals. This extension is discussed in Chapter 3.

Chapter 3

Chappuis and Hartley-Huggins Ozone Retrieval

3.1 Introduction

In Chapter 2, a description of ozone profiles retrieved using the SaskMART technique using only information from wavelengths in the Chappuis band was presented. This chapter expands on the retrievals in Chapter 2 by adding radiance information from the Hartley-Huggins band wavelengths, where the absorption cross section is at least two orders of magnitude larger, to the SaskMART retrieval. The result of the addition of Hartley-Huggins information is that it is possible to retrieve ozone profiles above the 40 km barrier imposed by the Chappuis-only technique. This allows the ozone density to be probed from the upper troposphere to the lower mesosphere.

The approach adopted here is similar to that in Chapter 2. There is an explanation of the Hartley-Huggins Vector Pair, which provides the additional data for the SaskMART inversion technique to yield ozone density profiles beyond 40 km, followed by a brief discussion of atmospheric factors that affect the inversion. Results are presented for comparisons of the SaskMART retrievals with the previous OSIRIS ozone product and the ozone density profiles of SAGE II described in sections 1.10.1 and 1.10.2. The data used with the SaskMART technique to produce the ozone retrievals is varied in order to choose optimal input data. Finally, there is a discussion of the uncertainty of the SaskMART retrieval technique.

3.2 Hartley-Huggins Vector Pair

3.2.1 Introduction

In addition to the CVT value discussed in Chapter 2, the *Hartley-Huggins Vector Pair* (HVP) is used as an input to the MART in order to match the measured and modelled radiances. As with the CVT the value of the HVP increases with increasing ozone concentration.

The CVT is formed according to Equation 2.1, repeated here as Equation 3.1:

$$\log\left(\frac{\sqrt{I_s \cdot I_l}}{I_p}\right), \tag{3.1}$$

where I_s, I_l, and I_p are the normalized radiance of a short reference wavelength, a long reference wavelength, and a peak wavelength, respectively. Conversely, a Hartley-Huggins Vector Pair is formed with just one reference wavelength. Both of the wavelengths used to form the HVP are taken from the Hartley-Huggins band region. The HVP is thus given by:

$$\log\left(\frac{I_r}{I_a}\right), \tag{3.2}$$

where I_r is the normalized radiance of a reference wavelength (taken just to the long wavelength side of the Hartley-Huggins ozone absorption band, see Figure 1.3) and I_a is the normalized radiance of an absorbed wavelength (within the Hartley-Huggins ozone absorption band). Like the CVT, the HVP increases when the ozone density along the satellite line of sight increases.

The absorbed and reference wavelengths that form the HVP are normalized to a high altitude where the effect of ozone absorption is small (see Equation 2.2). This has the effect of minimizing the effects of Earth albedo and instrument calibration on the measurements. The normalization altitude is chosen to be just above the highest altitude the given HVP is considered important in the retrieval (see Section 2.2.2 for a discussion of the normalization altitude for the CVT).

3.2.2 The HVP and Ozone Absorption

The Hartley-Huggins absorption band is between 200 and 300 nm. The shorter wavelength part of the band overlaps with the absorption band of molecular oxygen. Because of this overlap only one reference wavelength is possible in the Hartley-Huggins

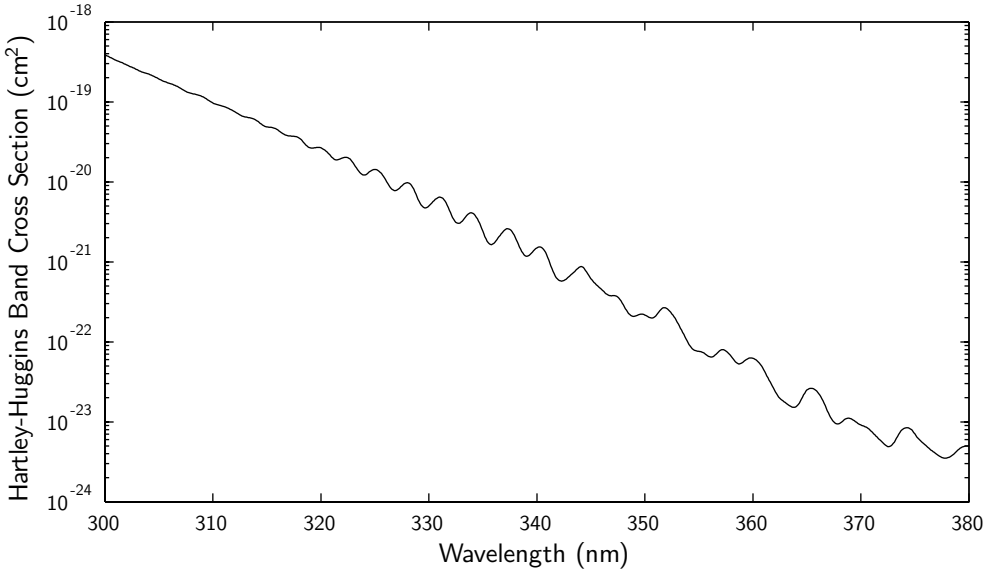

Figure 3.1: Cross Section of Ozone in the Hartley-Huggins region. The small scale structure on the absorption spectrum at these wavelengths is due to the the multitude of possible vibrational transitions in this energy range. The peaks and troughs in this range are suitable for use as reference and absorption wavelengths in the SaskMART retrieval.

Vector Pair. In addition, the Optical Spectrograph does not make measurements in the short wavelength region of the Hartley-Huggins band. In the Hartley-Huggins wavelength range there are a multitude of different possible transitions stemming from the different vibrational mode transitions in O_3. These transitions are responsible for the peaks and troughs in Figure 3.1. The troughs represent wavelengths where there is relatively less ozone absorption, while the peaks correspond to relatively more ozone absorption. The additional absorption at these local peaks means they serve well as an absorbed wavelengths of an HVP. A reference wavelength, that has a lower ozone cross section, is combined with a peak wavelength to form an HVP.

Figure 3.2 is a plot of the measured and modelled radiances within the Hartley-Huggins wavelength region at 40 km. The OSIRIS measurements and those calculated with the SaskTRAN model, using a retrieved ozone profile, are in good agreement. It may appear that the structure between 330 and 360 nm is due to ozone absorption. However, these features are part of the solar spectrum (they appear in the 40 km radiance data in Figure 1.8) and are not due to ozone absorption. However, because of the radiance variability in this region, caution must be exercised in choosing the HVPs in order to avoid the Fraunhofer structure.

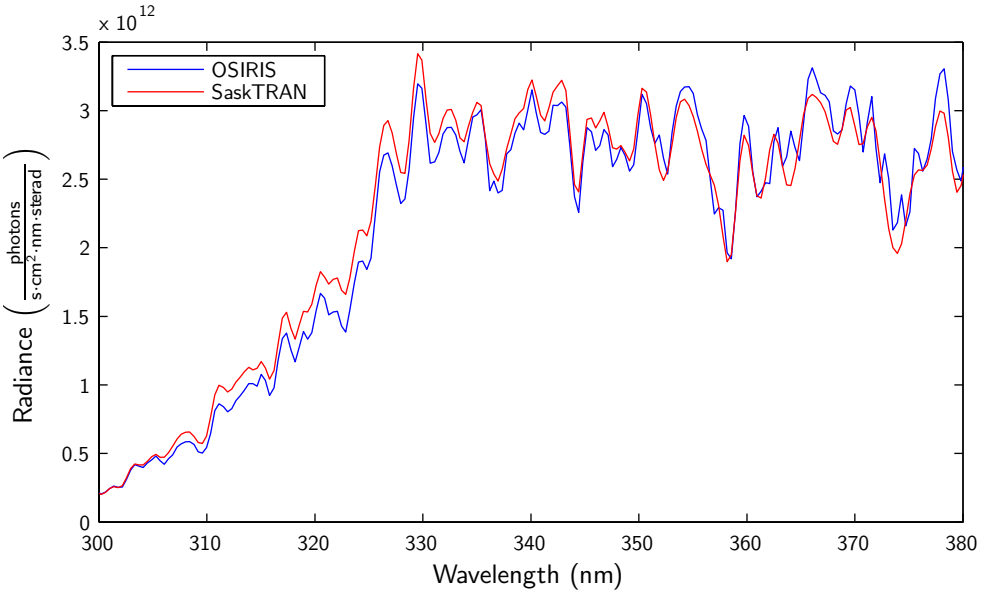

Figure 3.2: Radiance at 40 km in the Hartley-Huggins wavelength region. Fraunhofer structure, not ozone absorption, is responsible for the highly variable radiance values. The photons at each wavelength are absorbed at different rates as they pass through the ozone in the atmosphere. The measured OSIRIS radiances and those calculated with SaskTRAN are in good agreement.

To demonstrate that the ozone absorption signature is passed on to the radiance information, the radiance at 30 km is normalized to the radiance at 40 km for a sample scan. Because the radiance from 30 km has passed through a greater amount of ozone the ozone signature should be apparent. Figure 3.3 shows this to be the case. The two curves, measured and modelled, match well — especially at the positions of the peaks and troughs.

Three sets of modelled radiances have been compared with each other using three different ozone profiles. This comparison is shown in Figure 3.4. As the concentration of ozone increases so the normalized radiance decreases. The blue curve in the figure is the normalized radiance profile in the Hartley-Huggins band when no ozone is present. In comparison, the normalized radiance for the other two curves drops significantly in the high absorption region of the Hartley-Huggins ozone cross section. The vertical lines correlate to the difference in the normalized radiance between the reference wavelength (the black circle at 350 nm) and the absorbed wavelengths (coloured circles at 315 nm). The length of this line represents the HVP value of Equation 3.2.

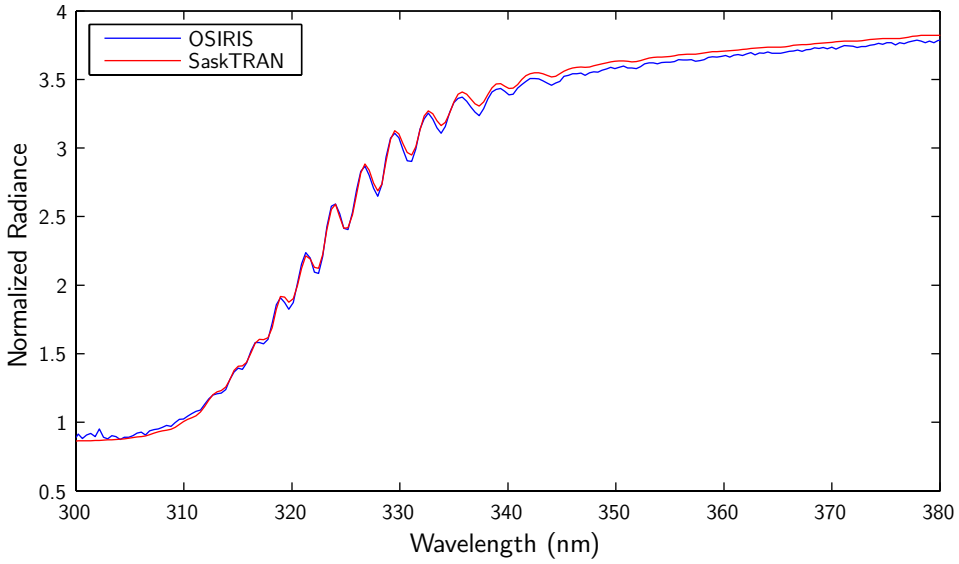

Figure 3.3: Radiance at 30 km normalized to the radiance at 40 km shown in the Hartley-Huggins wavelength absorption region. The peaks in this figure clearly correlate to the troughs in Figure 3.1. SaskTRAN produces the same normalized curve as the OSIRIS radiances; the troughs due to ozone absorption overlap with one another.

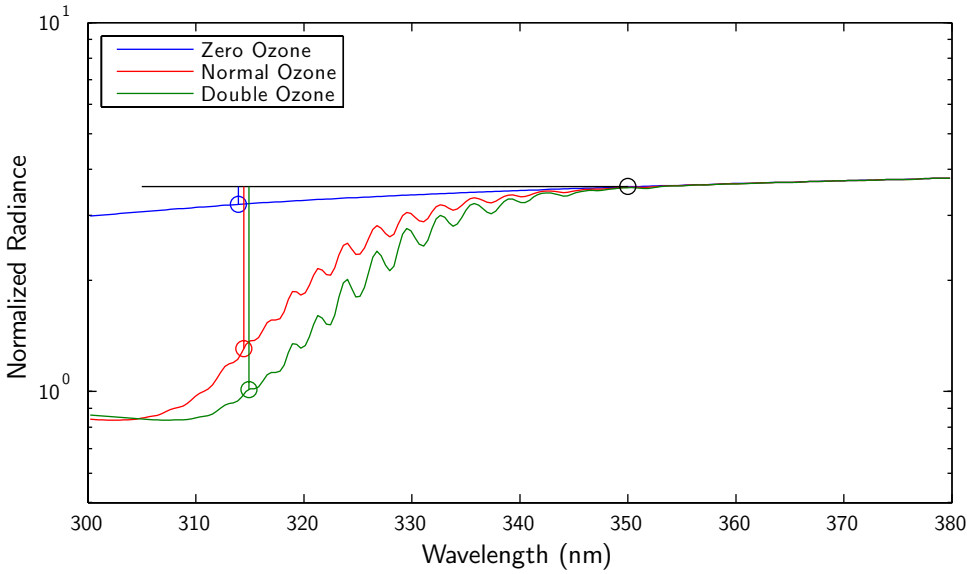

Figure 3.4: Three different ozone profiles were used to produce the three radiances shown above (30 km normalized at 40 km). The measurement represented by Equation 3.2 is correlated to the depth of the vertical lines.

3.3 HVP Wavelength Selection

Each HVP requires two wavelengths, a reference and an absorbed wavelength, as feedback for the SaskMART retrieval. In the Hartley-Huggins region, the ozone absorption and Rayleigh scattering cross sections vary rapidly so that wavelength selection is critical. Results from an examination of the wavelength section is presented in the following sections.

3.3.1 Optical Depth

As the wavelength of the incident light decreases from 400 to 300 nm, the probability of atmospheric scattering increases at an exponential rate ($\propto \lambda^{-4}$). The ozone cross section also increases over the same range (see Figure 3.1). The scattering and absorption effects combine to make the atmosphere optically thick at these wavelengths, more so at the shorter wavelengths. As the wavelength decreases and the probability of scattering or absorption increases so less light scattered from the lower atmosphere passes directly to the satellite without being scattered again or absorbed. The result is that the satellite only "sees" light from the top of the atmosphere down to some altitude that is determined by the wavelength.

Figure 3.5 is a plot of a selection of Hartley-Huggins band wavelength radiances as a function of altitude. These radiances are normalized to the top altitude and separated so they do not overlap. Starting at the higher altitude and moving down, the radiance of each wavelength increases exponentially. This is due to the fact that the scattering particles (*i.e.,* the neutral density) increases exponentially. The height at which the profile plateaus is called the "knee" in the radiance profile. As the wavelengths increase so the "knee" falls in altitude because the optical thickness has decreased.

3.3.2 Radiance and Vector Jacobians

The next step in choosing the Hartley-Huggins Vector Pair wavelengths is to determine how the radiance at different wavelengths in the Hartley-Huggins region changes with a change in the ozone density. That is, the shape of

$$\frac{\partial I}{\partial [\mathrm{O_3}]}. \tag{3.3}$$

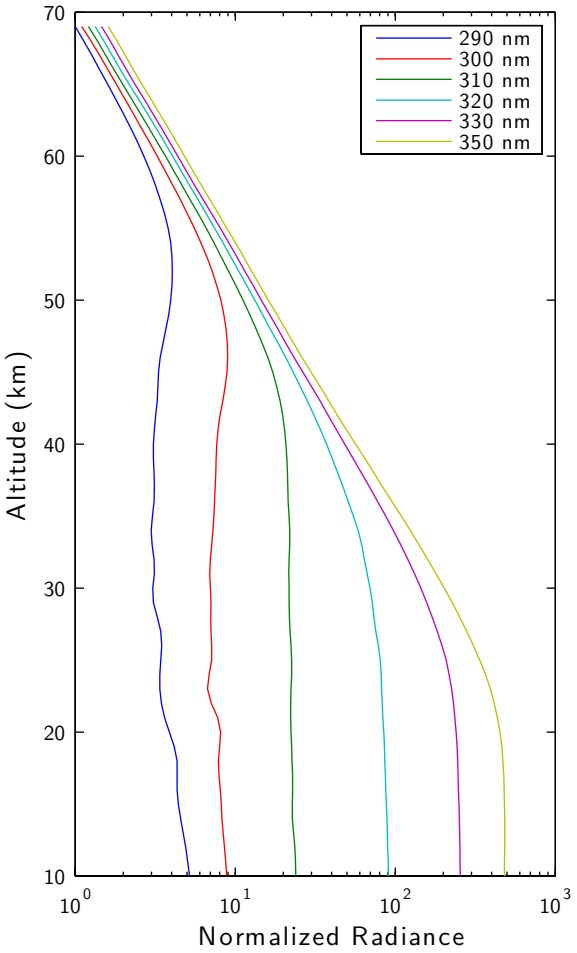

Figure 3.5: Radiance profiles of Hartley-Huggins wavelengths normalized to their radiance at 69 km and shifted to avoid overlap. From high altitude to low altitude each wavelengths radiance profile increases exponentially, according to the exponential increase in background scatterers, and then plateaus. The height at which the profile plateaus in called the "knee" in the radiance profile. As the wavelengths increase so the "knee" altitude decreases.

However, because the log of the radiance is used in Equation 3.2 and not the radiance, the calculated derivatives are:

$$\frac{\partial \ln(I)}{\partial [\mathrm{O_3}]}. \tag{3.4}$$

The derivatives are calculated for all altitudes for a change at a single altitude. This process is repeated for all other altitudes. The resulting matrix of derivatives is called the radiance Jacobian.

The results of the calculations are shown in Figure 3.6. Panels (a)–(e) of the figure show the change in radiance for a ten percent change (increase) in the ozone density. The altitude of the peak (*e.g.,* 52 km for 290 nm) decreases as the wavelength increases. The reason that the peak change moves lower with increasing wavelength is due to the position of the "knee" in Figure 3.5. The "knee" indicates the height below which changes in radiance are difficult to measure from the satellite, *i.e.,* it is optically thick. Thus changes in the ozone density below this height have little effect on the measured radiance. As the wavelength increases so the optical thickness decreases and the peak change altitude descends.

Panel (f) shows that there is a minimal change in the radiance at 350 nm, this means that the radiance is not strongly affected by a change in ozone. For this reason a wavelength in the region of 350 nm is suitable for use as the reference wavelength in the HVPs.

Figure 3.7 is a plot of the Hartley-Huggins Vector Pair Jacobians with 350 nm as the reference wavelength. The Jacobians are formed according to Equation 3.2 with the radiances in Figure 3.6. Each of the HVP Jacobians peaks at a different altitude that corresponds to where the absorbed wavelength peaked (see Figure 3.6). The areas around the peaks form the regions that SaskMART is used to retrieve the ozone profile.

The CVT Jacobian (Figure 3.7(f)) and the last of the HVP Jacobians (Panel (e)) cover approximately the same altitude region. Thus, there is no reason to include this Hartley-Huggins Vector Pair in the SaskMART retrieval as it adds no further information from that already available in the CVT. The first vector in this sample set to cover a different altitude range uses 320 nm as the absorbed wavelength (Panel (d)). Beginning with 320 nm and moving to shorter wavelengths, the peak of the Hartley-Huggins Vector Pair moves higher.

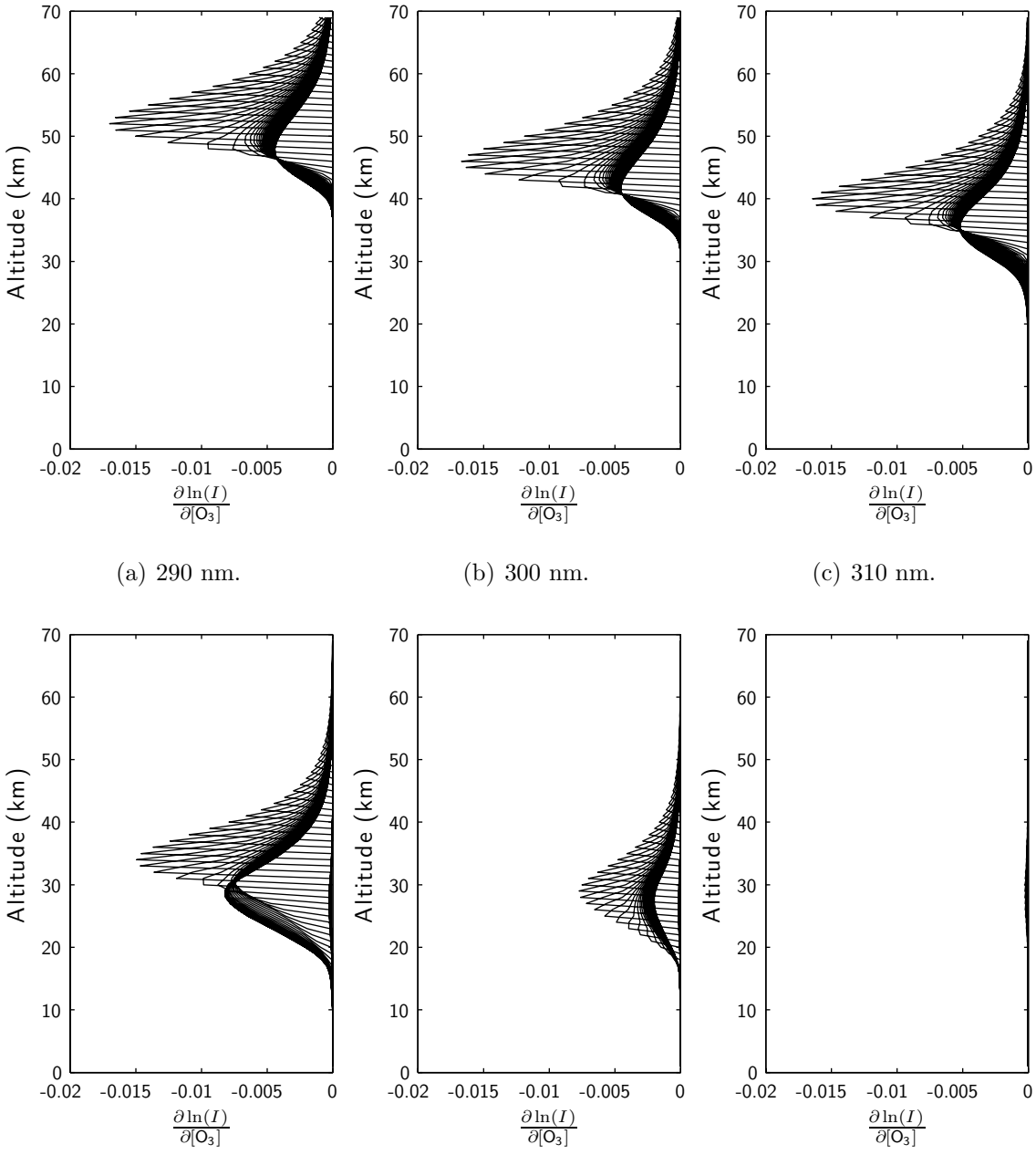

(a) 290 nm. (b) 300 nm. (c) 310 nm.

(d) 320 nm. (e) 330 nm. (f) 350 nm.

Figure 3.6: The rate of change in the radiance at the reference wavelength with respect to change in ozone (Panel (f)) is negligible compared to the rate of change in radiance at the absorbed wavelengths (Panels (a)–(e)).

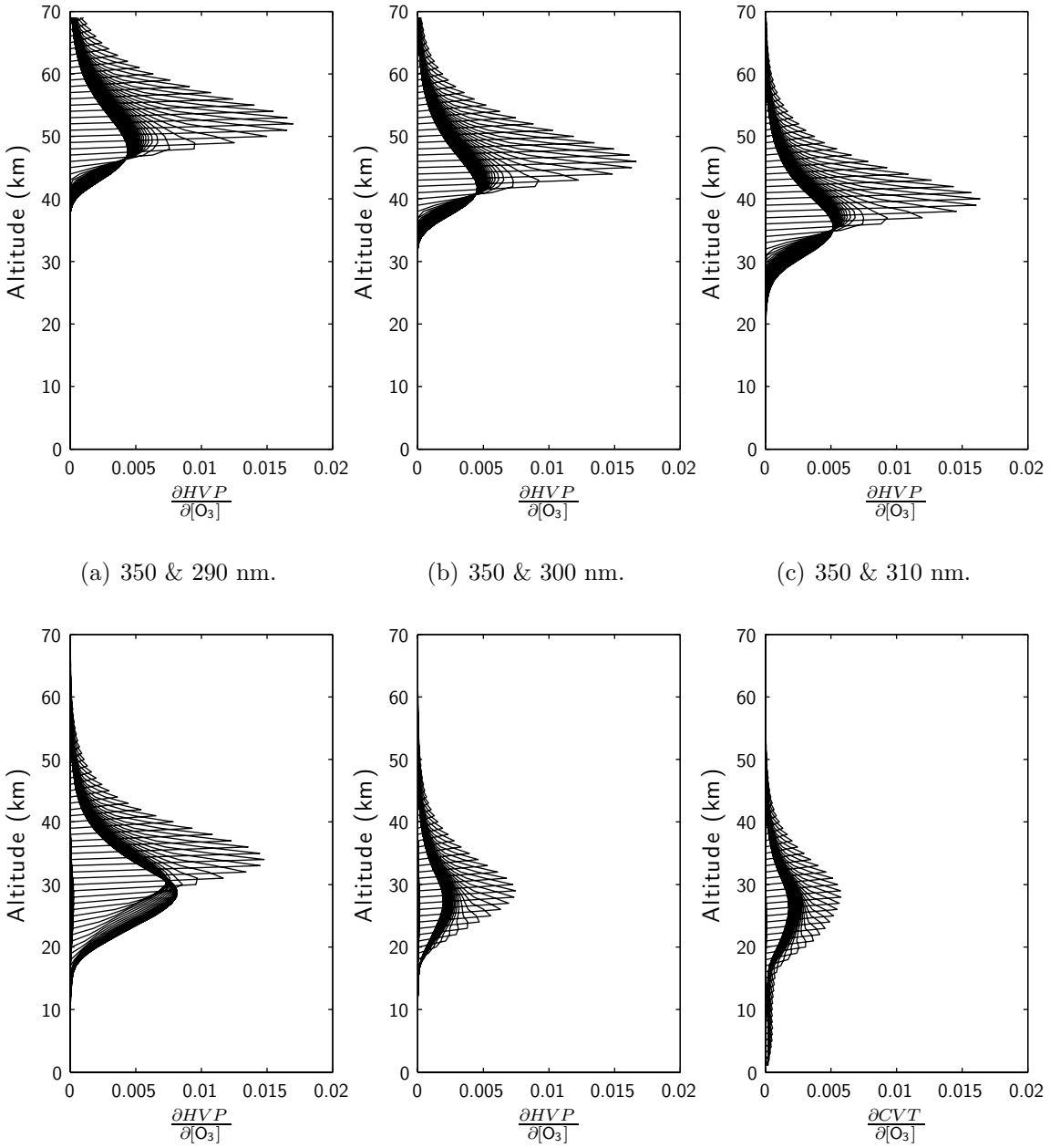

(a) 350 & 290 nm. (b) 350 & 300 nm. (c) 350 & 310 nm.

(d) 350 & 320 nm. (e) 350 & 330 nm. (f) Chappuis Vector Jacobian

Figure 3.7: The HVP Jacobians calculated with the radiance Jacobians shown in Figure 3.6. The CVT Jacobian (Panel (f)) is included for reference.

The valid range for use for each of the HVPs is determined by combining the peak sensitivity regions in Figure 3.7 with the "knee" boundary information from Figure 3.5. Using 310 nm as an example, the green curve in Figure 3.5 has its "knee" at approximately 42 km. Figure 3.7(c) shows that the change in the vector that uses 310 nm is measurable from 28 to 57 km. The "knee" value combines with the ∂V range to give a useable region between 42 and 57 km. Table 3.1 is a summary of the information from the two figures for all five wavelengths included in Figure 3.7.

Table 3.1: Summary of Hartley-Huggins Wavelength Pair Retrieval Altitudes

	Knee Altitude	**Peak Range**	**Useful Region**
350 & 290 nm	53 km	40–69 km	53–69 km
350 & 300 nm	47 km	35–65 km	47–65 km
350 & 310 nm	42 km	28–57 km	42–57 km
350 & 320 nm	32 km	18–50 km	32–50 km
350 & 330 nm	25 km	19–42 km	25–42 km[a]

[a]Overlaps with CVT.

3.3.3 Resultant Wavelength Pairs

In Section 3.3.2 the Hartley-Huggins Vector Pairs were formed and their Jacobians analyzed to find the range of wavelengths needed in the Hartley-Huggins region that can provide ozone sensitivity from the Chappuis region up to 60 km. The range of absorbed wavelengths that do not overlap with the CVT ends between 320 and 330 nm. HVPs whose absorbed wavelength is greater than 290 nm and less than 330 nm are used in the SaskMART retrieval. Within this region, there is freedom in the choice of absorbed wavelengths; the five used in Section 3.3.2 are illustrative of the entire region. In order to choose particular absorbed wavelength values in this region preference is given to those wavelengths where the ozone absorption cross section is relatively large (the peaks in Figure 3.1). The resultant absorbed wavelengths have been paired with the reference wavelength at 350 nm and the results are tabulated in Table 3.2.

Table 3.2: Retrieval Altitudes of Chosen Hartley-Huggins Wavelength Pairs

	Knee Altitude	**Peak Range**	**Useful Region**	**Notation**
350 & 290 nm	53 km	40–69 km	53–69 km	HVP 6
350 & 300 nm	47 km	35–65 km	47–65 km	HVP 5
350 & 309 nm	42 km	28–57 km	42–57 km	HVP 4
350 & 315 nm	37 km	23–54 km	37–54 km	HVP 3
350 & 320 nm	32 km	18–50 km	32–50 km	HVP 2
350 & 322 nm	25 km	18–50 km	25–50 km	HVP 1

3.4 Weighting Filter Function

Once the wavelength pairs have been formed according to their Jacobians and ozone absorption characteristics, they must be weighted with respect to their useful regions (Table 3.2) so that they provide accurate input information for SaskMART. This means that a table of W_{ik} terms must be formulated (see § 1.9.4), for the k observations that will be used.

The weighting filter function determines the contribution of each CVT/HVP to each altitude in the retrieved ozone profile. For example, the amount of retrieved ozone at 40 km should depend on the HVPs that are useful in that region (*i.e.*, 350 nm & 322 nm, 350 nm & 320 nm, and 350 nm & 315 nm). Using Table 3.2, a weighting filter function was formed, see Figure 3.8. Each of the HVPs gradually transition in and out over the region given in Table 3.2. A gradual transition rather than a step function is used in order to prevent oscillations in the retrieval that could be caused by slight differences in the vectors. To avoid single vector noise all altitudes depend on more than one vector. However, the sum of the weights at any altitude is equal to unity.

Below 33 km, only the two CVTs discussed in Section 2.6 have a contribution to the weighting filter function. The dashed line in Figure 3.8 is the sum of their weights and is included as it shows the transition and the relative weighting of the CVTs in comparison with the HVPs. At 33 km, the transition from CVTs to HVPs begins. The weighting of the CVTs decreases according to the shape of the error function as this allows for a smooth transition between vectors. By 38 km the CVTs no longer contributes to the combined vector used by SaskMART.

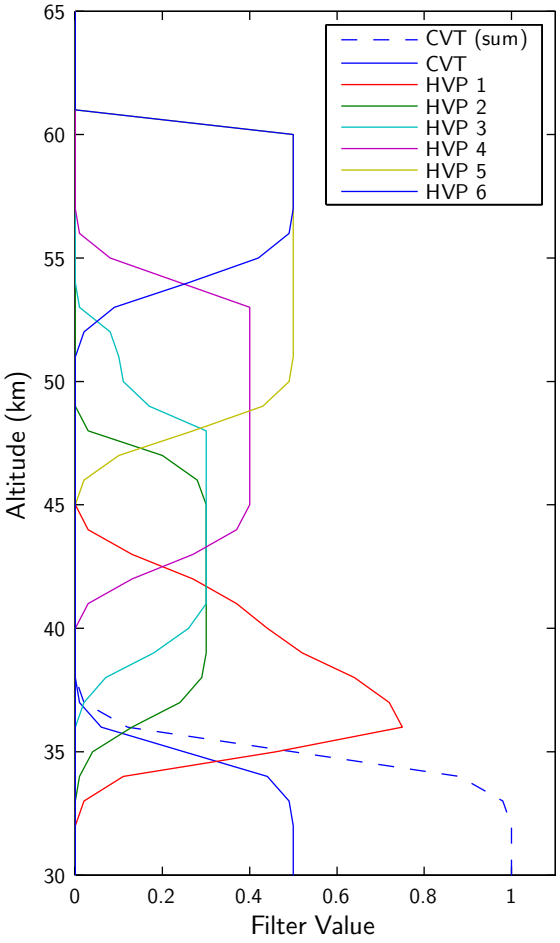

Figure 3.8: The weighting filter function that determines how the vectors contribute information for a given altitude. The text in the legend corresponds to the lines in the plot from bottom to top, where "HVP n" stands for the n^{th} Hartley-Huggins vector given in Table 3.2. The solid Chappuis lines represent the two individual CVT contributions; the dashed line is the sum of both CVT contributions.

The weighting filter function begins at the upper altitudes in a similar fashion to that at the lower altitudes; that is, the weight is divided equally between to HVPs. Then as the altitude decreases, the HVPs transition out in the same manner as the CVTs did at 30 km, see Table 3.2. As the next vector is introduced the total of the weighting filter function remains equal to unity and explains the shape of the upper transition portion of the HVPs (*e.g.,* HVP 4 between 53 and 56 km or HVP 3 between 48 and 53 km). The value of HVP 1 ensures that the transition on both sides equals unity.

With the exception of HVP 1, the values of the weighting filter function for the CVTs and HVPs plateau over the range noted in Table 3.2. The height of the plateau region (*e.g.,* 0.3 for HVP 2 and HVP 3) was chosen so that the transitions remained smooth and the weighting filter function included multiple vectors at each altitude. The shapes of some of the weighting filter functions (especially HVP 1) are "different" looking as a result of the attempt to transition vectors in and out smoothly.

The normalization of the HVPs is done with the first line of sight tangent height above the region that is used in the weighting filter function. For example, HVP 4 is normalized to the first line of sight tangent height above 57 km; HVP 5 and HVP 6 are normalized to the first line of sight tangent above 61 km.

As in the Chappuis-only retrieval, the HVP observations used at every tangent altitude retrieved by SaskMART are a combination of the three highest OSIRIS lines of sight that pass through that tangent altitude (see Section 2.2.4). The highest tangent height through the region has a weight of 0.6, the next highest, 0.3, and the lowest, 0.1.

3.5 Comparison Results

In order to validate the SaskMART retrieval technique the results have been compared with those from SAGE II and SAGE III retrievals. The SAGE III ozone product is included in this comparison as it is valid to a higher altitude than the SAGE II ozone product (see §1.10.3).

3.5.1 First Comparison Set

The first comparison data set used data from a three day, two degree bin in early January, 2004 around 37°S latitude, shown in Figure 3.9. The results of the first comparison are shown in Figure 3.10. There is agreement to within five percent between the three mean profiles over the altitude range 22 to 53 km.

Above 53 km the SaskMART mean retrieval departs significantly from both mean SAGE retrievals. There are several possible reasons for these differences. The first, and most probable reason, is that the ozone profiles measured by SAGE II, SAGE III, and OSIRIS are actually different at these high altitudes where diurnal photochemistry plays an important role (see §1.4.2). Both SAGE II and SAGE III measurements are solar occultations at either dawn or dusk, while OSIRIS measurements are made with a line of sight perpendicular to the sun and not at twilight. The combination of different local time conditions, leading to different ozone concentrations, and perpendicular views through the atmosphere can introduce difference in the ozone concentrations. A second possible reason is that the accuracy of the SAGE profiles is lower above 53 km. Individual SAGE III profiles are quite noisy above 53 km, while SAGE II profiles are only valid to 53 km.

3.5.2 Second Comparison Set

The second comparison set used data from a three day, two degree bin in early June, 2005 around 50°N latitude, as shown in Figure 3.11. The results of the second comparison are shown in Figure 3.12. There is agreement to within eight percent between the three mean profiles over the altitude range 20 to 53 km. As within the first comparison the SaskMART mean retrieval disagrees with the mean SAGE retrievals above 53 km. The mean SAGE III profile shows the largest differences from the other two profiles. Between 20 and 40 km, the SAGE II profile is considered to be more accurate than the SAGE III product.

3.5.3 Third Comparison Set

The third comparison set is shown in Figure 3.13. This set used data from a two day, two degree bin in early June, 2004 around 50°N latitude, which is the same time of year and latitude region as for the second comparison set. Figure 3.14 shows the mean retrievals from the third comparison. There is agreement to within ten percent

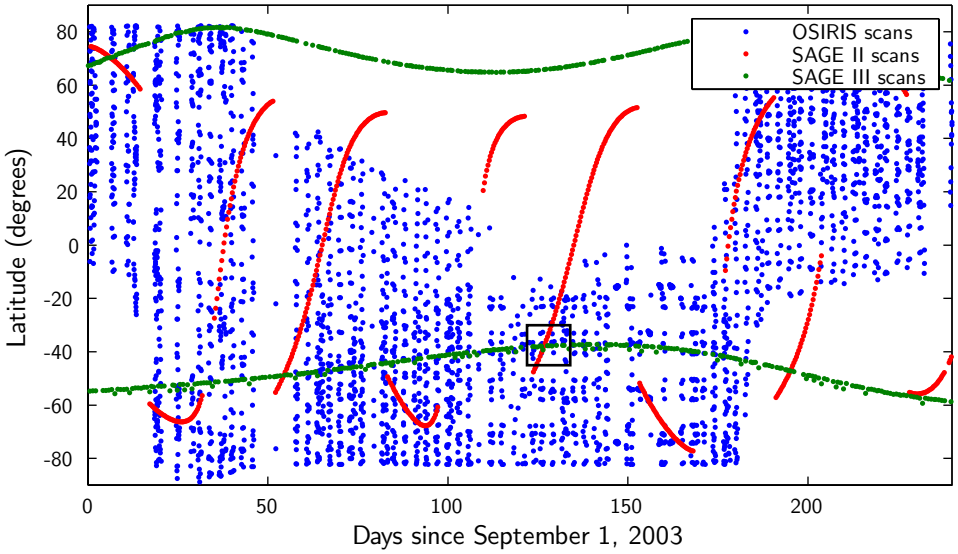

(a) OSIRIS, SAGE II and SAGE III scans for an eight month period starting September 1, 2003. The coincidence scans were taken from the area marked by the rectangle and enlarged in Panel (b).

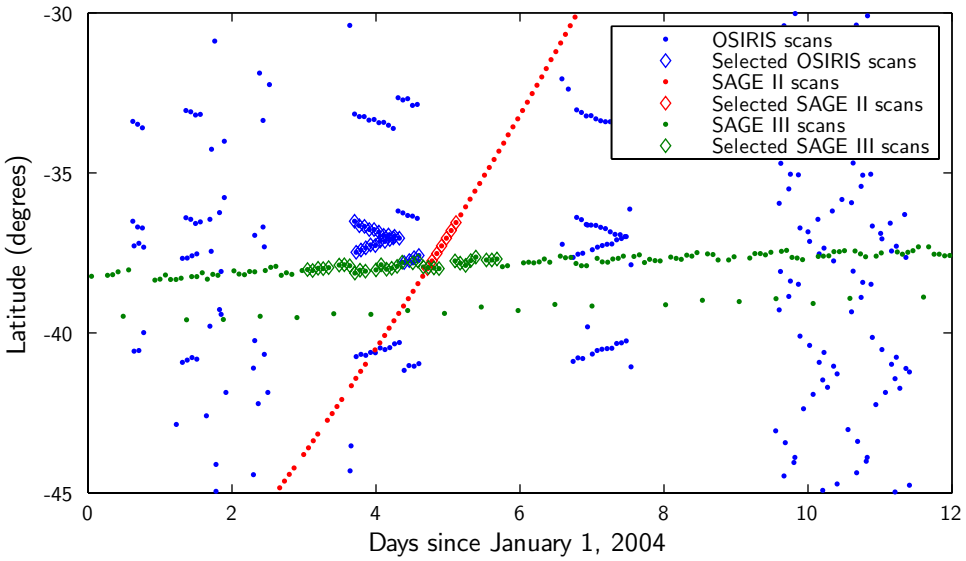

(b) Coincident OSIRIS, SAGE II and SAGE III scans used to compare and validate the retrieved ozone profiles. There are twenty-three OSIRIS scans, seven SAGE II scans, and thirty-one SAGE III scans.

Figure 3.9: The first comparison set.

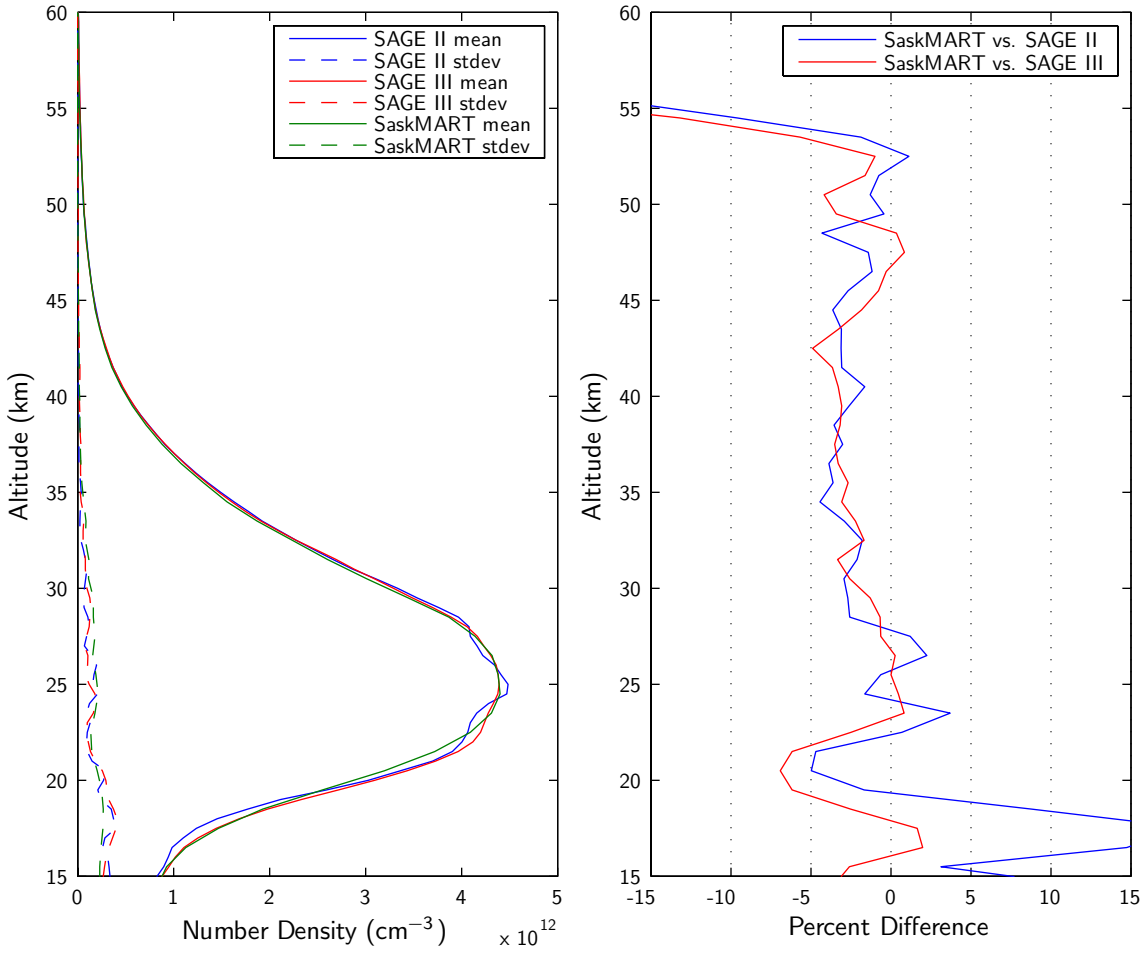

(a) Mean retrieved profile comparison.

(b) Percent difference.

Figure 3.10: Mean retrieved profile obtained using both Chappuis and Hartley-Huggins information. The SaskMART mean retrieved profile agrees with SAGE II and SAGE III to five percent between 22 and 53 km.

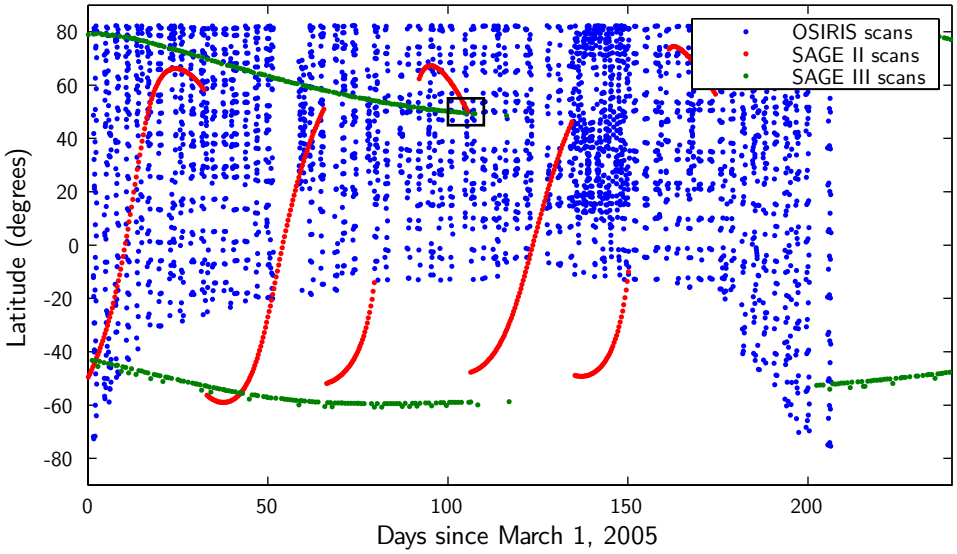

(a) OSIRIS, SAGE II and SAGE III scans for an eight month period starting March 1, 2005. The coincidence scans are taken from the area marked by the rectangle and enlarged in Panel (b).

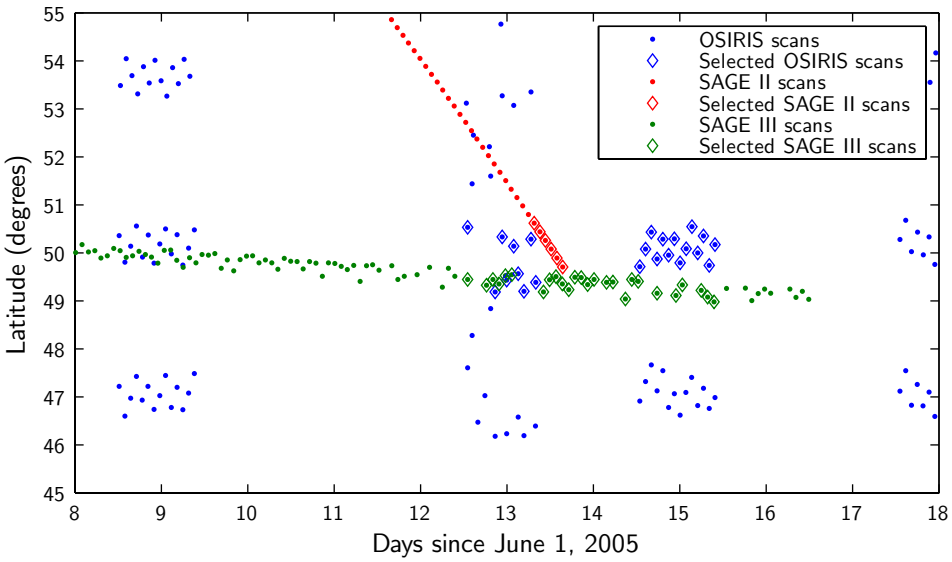

(b) Coincident OSIRIS, SAGE II and SAGE III scans used to compare and validate the retrieved ozone profiles. There are twenty-three OSIRIS scans, six SAGE II scans, and twenty-six SAGE III scans.

Figure 3.11: The second comparison set.

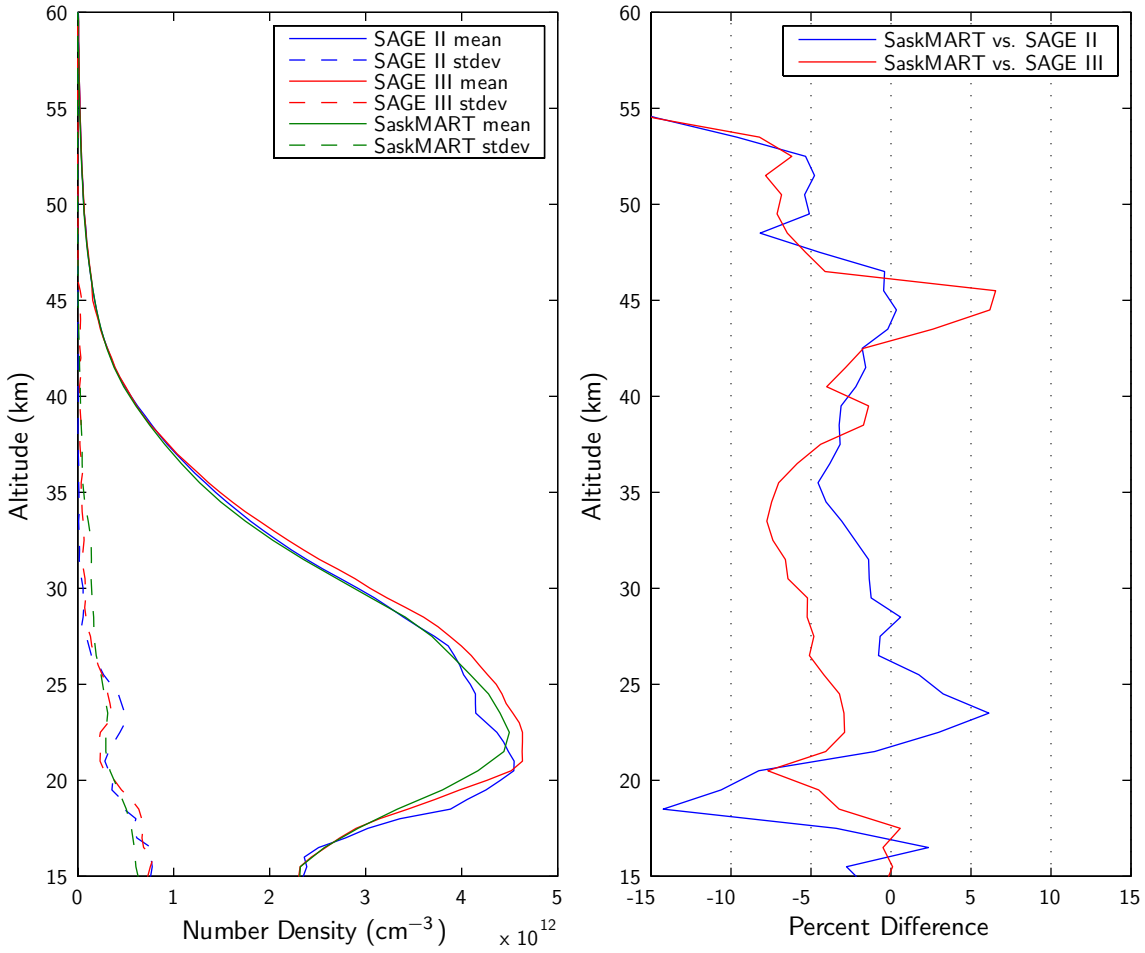

(a) Mean retrieved profile comparison.

(b) Percent difference.

Figure 3.12: Mean retrieved profile obtained by using both Chappuis and Hartley-Huggins information. The SaskMART mean retrieved profile agrees with SAGE II and SAGE III to eight percent between 20 and 53 km.

between the three mean profiles over the altitude range 16 to 54 km. The mean retrieval diverge above 54 km as for the first and second comparisons. The mean profiles that are shown in Figure 3.12(a) and Figure 3.14(a) have approximately the same peak altitude and concentration.

3.5.4 Fourth Comparison Set

The fourth comparison set uses data from a two day, three degree bin in late April, 2003 around 60°N latitude, as shown in Figure 3.11. The results of the fourth comparison are shown in Figure 3.12. There is agreement to within nine percent between the three mean profiles over the altitude range 15 to 53 km. As with the other three mean retrieval comparisons, the SaskMART mean retrieval disagrees with the mean SAGE retrievals above 53 km.

3.5.5 Comparison Summary

The comparison sets show that the SaskMART technique is able to retrieve ozone density profiles accurately between 20 and 55 km. The profiles are in good agreement with those from both SAGE II and SAGE III. The maximum difference for the four comparison sets is ten percent. The average difference is around five percent, which is the error estimate of the SAGE III ozone density profiles (see §1.10.3).

3.6 Retrieval Error

Following the procedure described in Section 2.8, the error profiles due to bias, Earth albedo, aerosol loading, instrument pointing uncertainty, and retrieval vector noise were calculated for the combined retrieval using both Chappuis and Hartley-Huggins vectors.

The sample vector/retrieval kernel shown in Figure 3.17 was calculated using the same scan as that used in the Chappuis-only error section. The transition zone from Chappuis to Hartley-Huggins vectors occurs seamlessly over the 33 to 38 km height range (see Figure 3.8). Like the Chappuis-only vectors, a positive change in a combined vector at a given altitude results in a positive change in the ozone concentration at and above that altitude with a negative change in the ozone concentration below the given altitude.

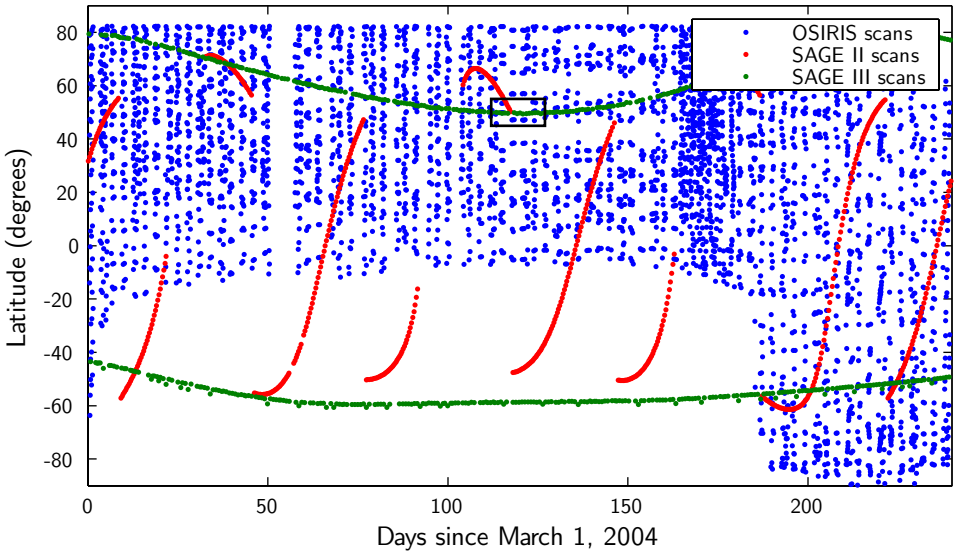

(a) OSIRIS, SAGE II and SAGE III scans for an eight month period starting March 1, 2004. The coincidence scans are taken from the area marked by the rectangle and enlarged in Panel (b).

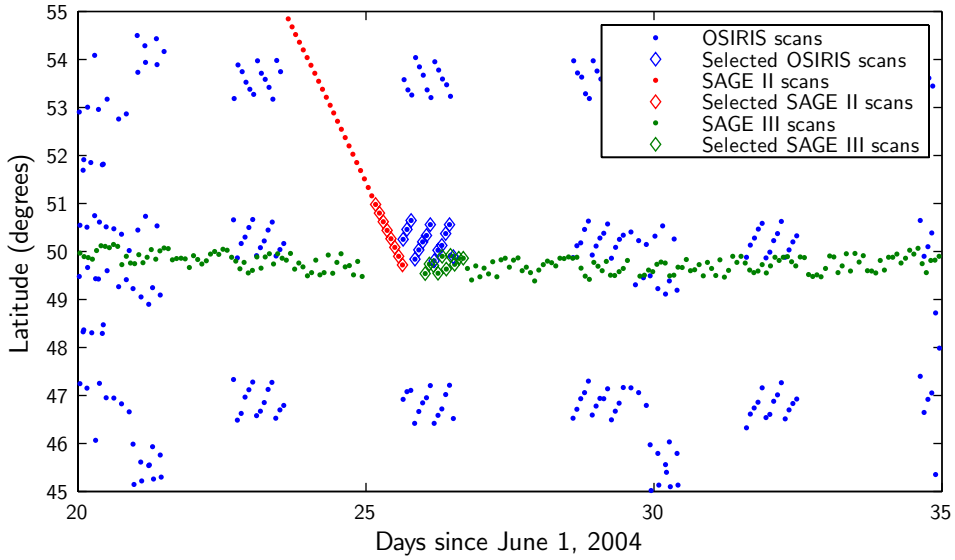

(b) Coincident OSIRIS, SAGE II and SAGE III scans used to compare and validate the retrieved ozone profiles. There are fourteen OSIRIS scans, eight SAGE II scans, and ten SAGE III scans.

Figure 3.13: The third comparison set.

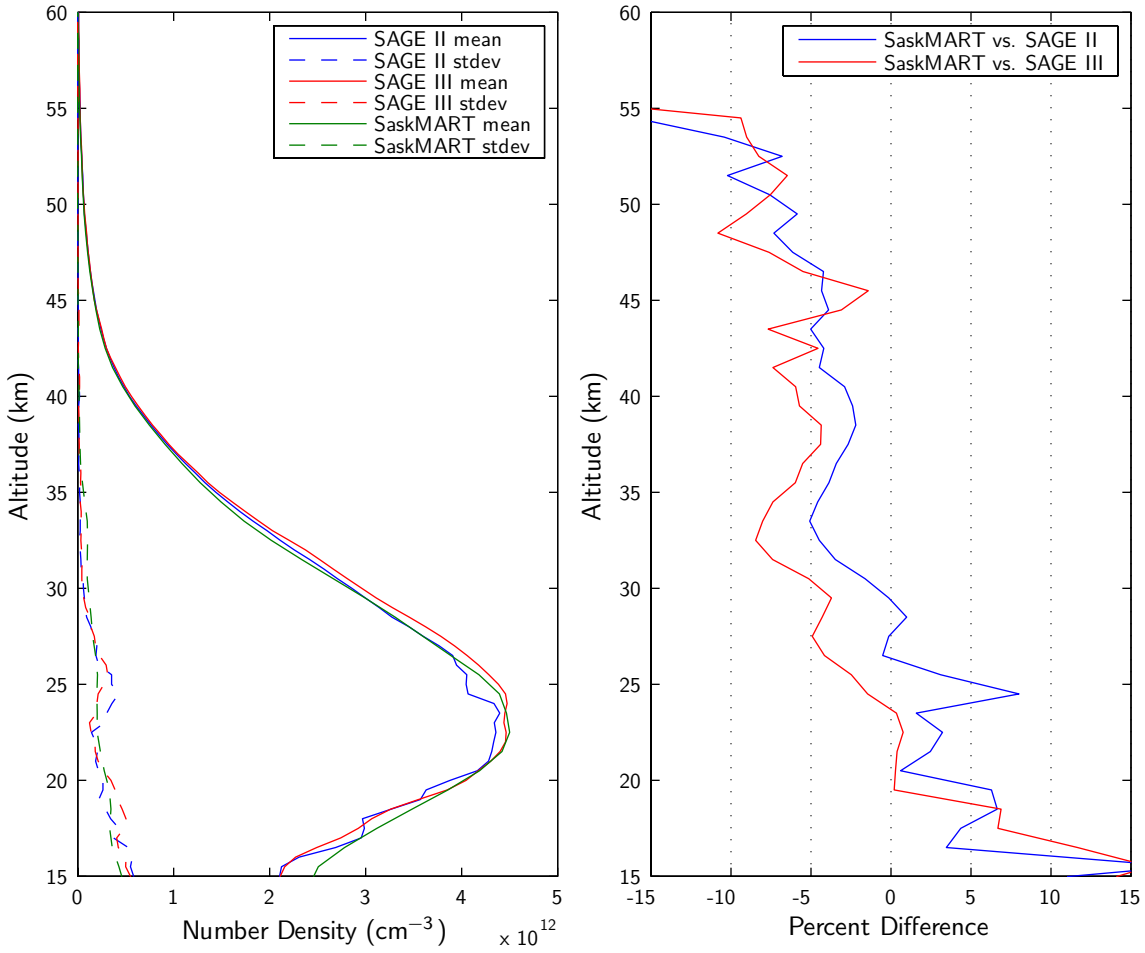

(a) Mean retrieved profile comparison.

(b) Percent difference.

Figure 3.14: Mean retrieved profiles obtained by using both Chappuis and Hartley-Huggins information. The SaskMART mean retrieved profile agrees with SAGE II and SAGE III to ten percent between 16 and 54 km.

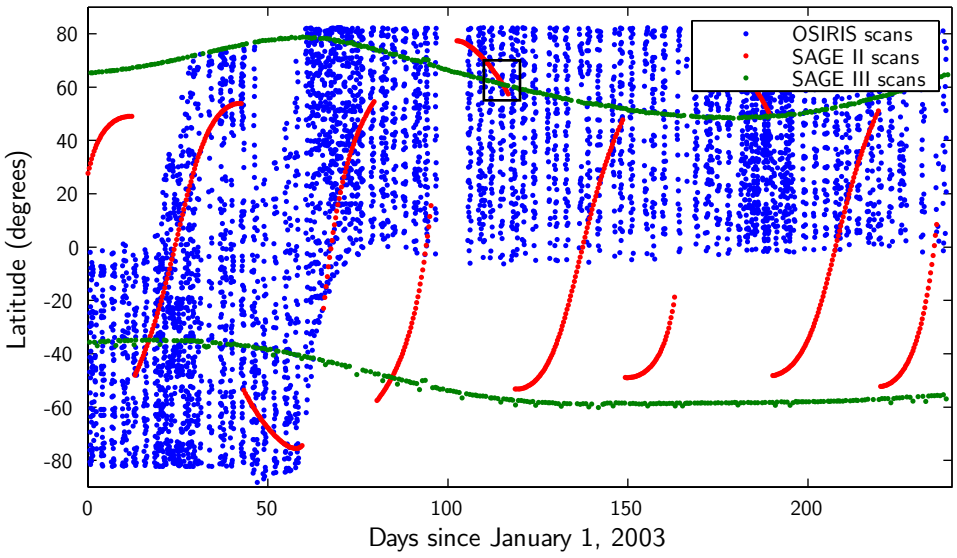

(a) OSIRIS, SAGE II and SAGE III scans for an eight month period starting January 1, 2003. The coincidence scans are taken from the area marked by the rectangle and enlarged in Panel (b).

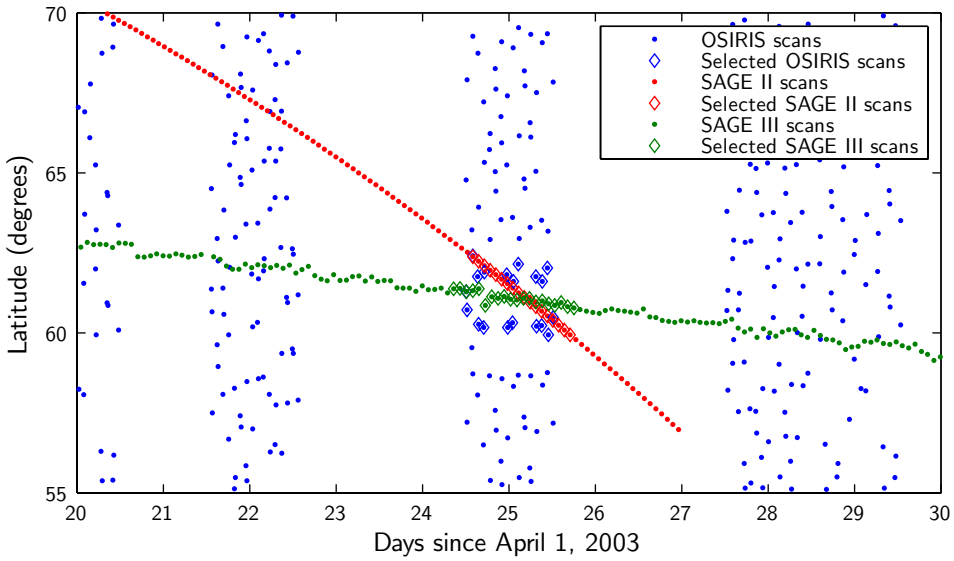

(b) Coincident OSIRIS, SAGE II and SAGE III scans used to compare and validate the retrieved ozone profiles. There are nineteen OSIRIS scans, eighteen SAGE II scans, and twenty SAGE III scans.

Figure 3.15: The fourth comparison set.

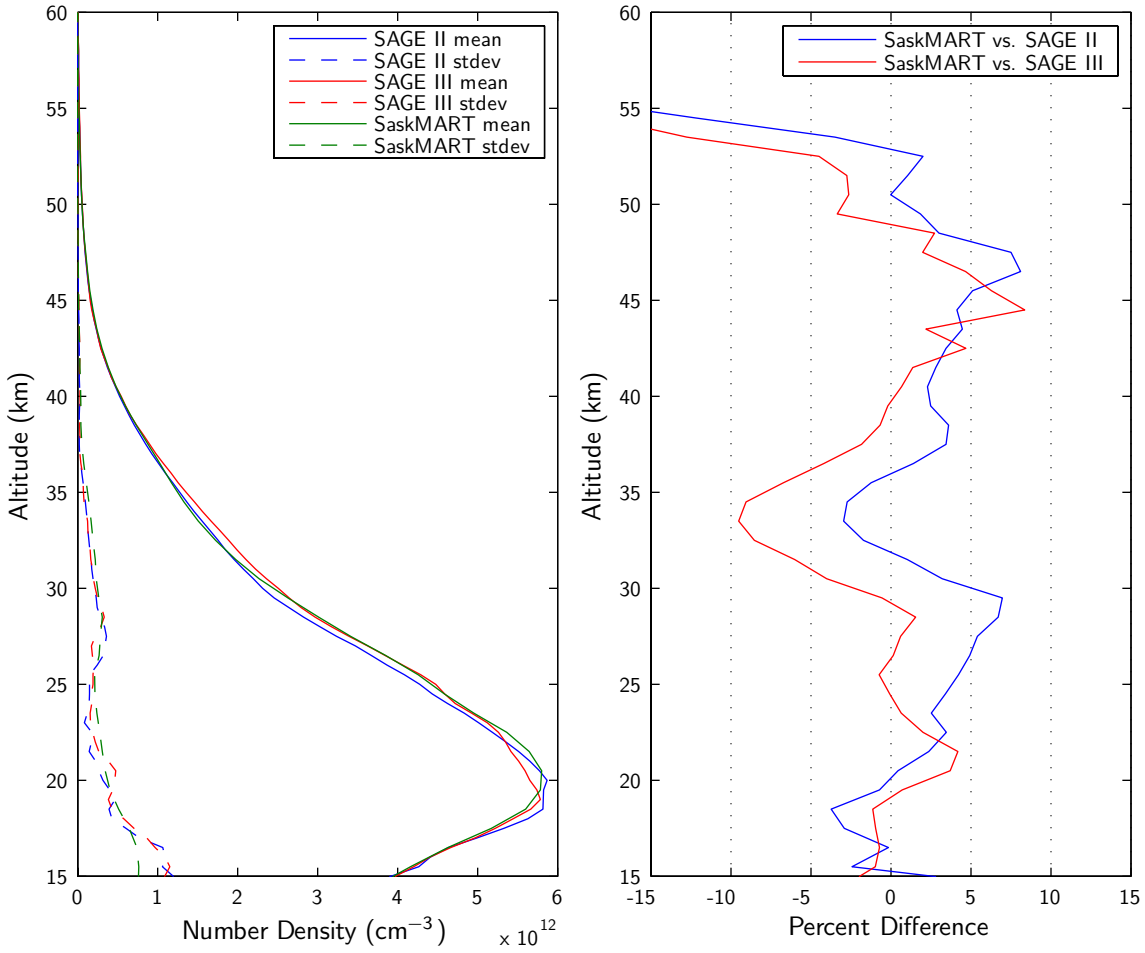

(a) Mean retrieved profile comparison.

(b) Percent difference.

Figure 3.16: Mean retrieved profiles obtained by using both Chappuis and Hartley-Huggins information. The SaskMART mean retrieved profile agrees with SAGE II and SAGE III to nine percent between 15 and 53 km.

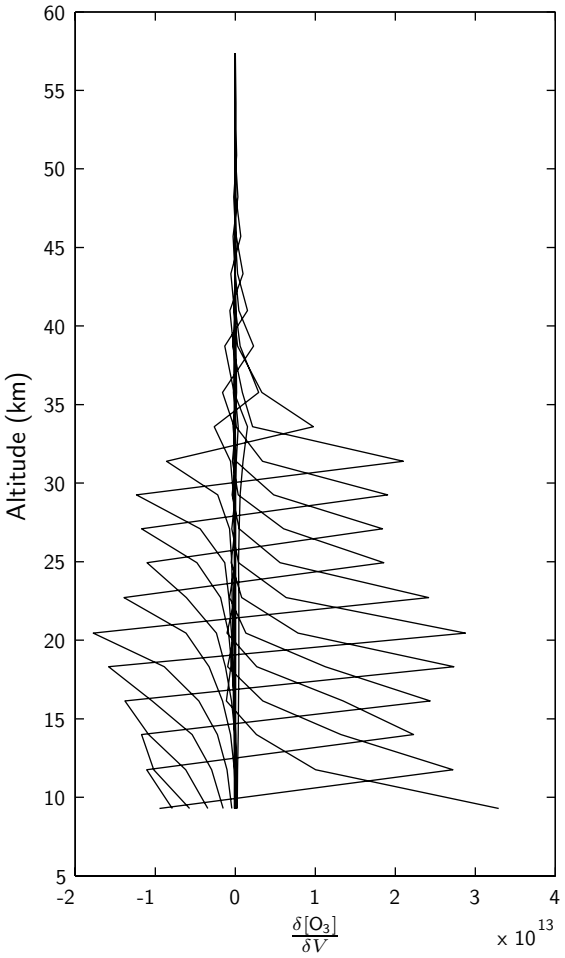

Figure 3.17: The vector/retrieval kernel shows the effects in the ozone retrieval caused by making small changes in the retrieval vectors.

3.6.1 Bias

Figure 3.18(a) shows the same three sample ozone profiles as in Figure 2.34(a). The dashed lines represent sample ozone profiles used to generate radiances. The radiances were then used to retrieve ozone density profiles following the same procedure as Section 2.8.2. All three use the same initial ozone density profile. The radiance vectors were calculated at the tangent altitudes shown by the vertical black dashed lines. The retrieval altitude extremes (where the retrieved profile merges with the initial guess profile) are now 9 km and 58 km.

Figure 3.18(b) shows that the merge of the Chappuis/Hartley-Huggins retrieval with the initial guess ozone profile has the same instabilities as the merge with the Chappuis-only retrieval. At both the lowest and highest altitudes there are differences

between the sample and retrieved profiles. Profile 1, that has an identical shape as the initial guess profile, has the least difference. Profile 3 represents a typical merge, while Profile 2 is an example of an extreme case. The oscillatory pattern at the higher altitudes of Profile 3 has the same distance between peaks as the tangent heights used for the retrieval; this suggests a systematic over-compensation and under-compensation.

The bias error is assumed to be two percent over the entire altitude range of the retrieval with an additional three percent added to the lowest two altitudes (14 km and below) and highest three altitudes (51 km and above).

3.6.2 Earth Albedo and Aerosol Load

Figure 3.19(b) shows the effect of varying the albedo (by 0.1) and the aerosol load (by 30%), the error introduced in the retrieval is less than one percent in both cases. These are much smaller than the bias error discussed in Section 3.6.1 and the instrument error discussed in Section 3.6.4

3.6.3 Pointing Error

If the same pointing error uncertainty of 200 m is assumed as for the CVT retrievals the effect of the pointing error on the Chappuis/Hartley-Huggins retrieval is less than one percent and is largest at the lowest tangent altitudes (see Figure 3.19(b)).

3.6.4 Retrieval Noise Error

While the Chappuis Vector Triplet error was given by Equation 2.19, the Hartley-Huggins Vector Pair error is found by differentiating Equation 3.2:

$$\sqrt{\left(\frac{\mathrm{d}I_r}{I_r}\right)^2 + \left(\frac{\mathrm{d}I_a}{I_a}\right)^2} \tag{3.5}$$

These values were calculated and used to populate the vector error, $\mathbf{S}_\epsilon$, which was then used to calculate the retrieval noise covariance matrix, $\mathbf{S}_m$ via Equation 2.17. The results are shown in Figure 3.19(b). The magnitude of the retrieval noise error increases from two percent to six percent at the lower altitudes following the same shape as the retrieval noise error of the Chappuis-only retrieval (see Figure 2.36(b)) until the introduction of the HVPs. As the weighting of the CVTs is reduced to zero

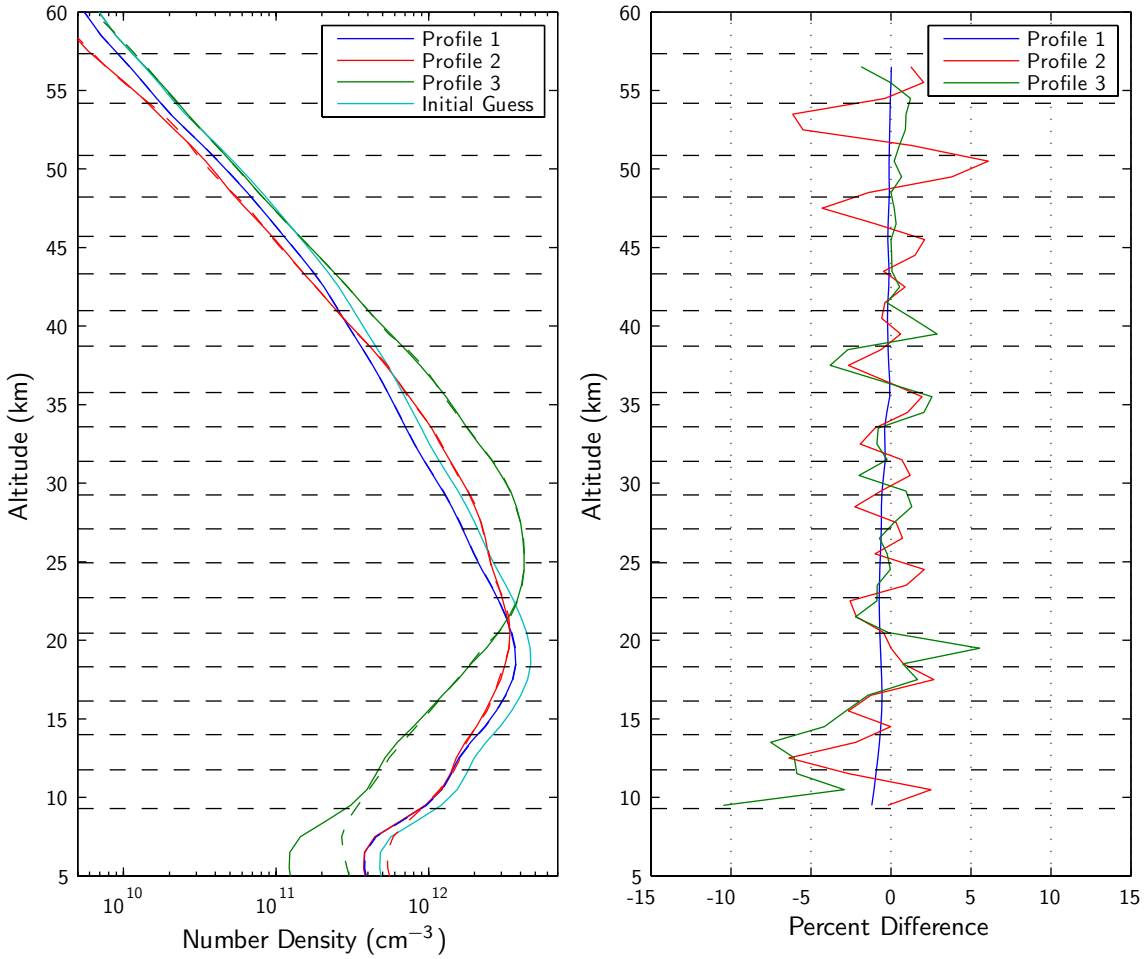

(a) Three sample ozone profiles used to characterize the bias of the SaskMART ozone retrieval. The dashed lines are sample ozone profiles used to generate radiances for the retrieved ozone density profiles (the solid lines). The initial guess profile used in each of the retrievals is also shown. The horizontal black dashed lines show the tangent altitudes used for the retrieval and are typical for the OSIRIS instrument.

(b) The percent difference between the sample profiles used to generate radiances and the retrieved profiles of Panel (a). Below the lowest retrieval altitude and above the highest retrieval altitude, the retrieved profile merges with the shape of the initial guess profile.

Figure 3.18: Three ozone density profiles showing the SaskMART retrieval bias.

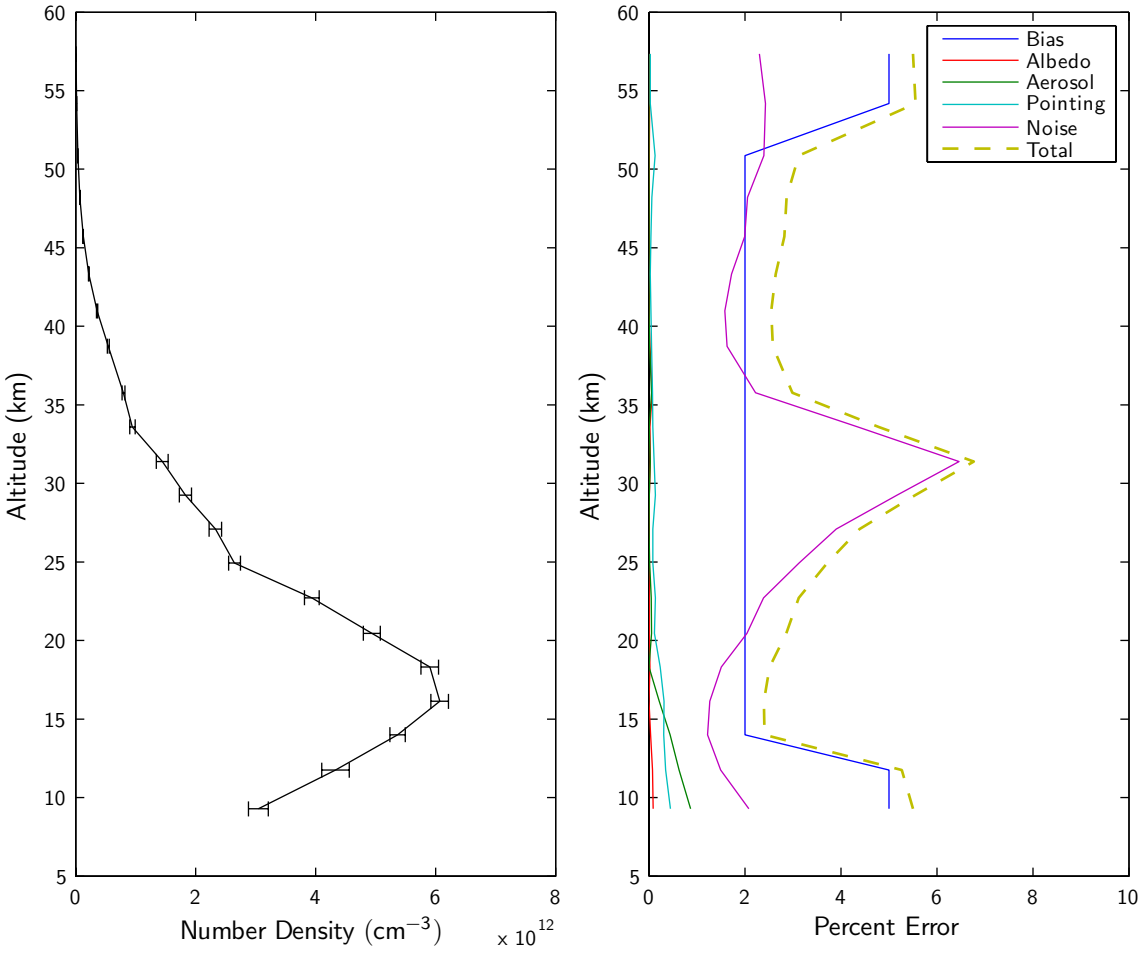

(a) Retrieved profile with error.

(b) Percent difference.

Figure 3.19: A sample OSIRIS scan with error bars denoting the total error and the errors due to the different error sources.

so the retrieval noise error drops to the smaller amount of error in the HVPs. This effect causes the peak in the error at 32 km. Above this peak the retrieval noise error remains close to two percent.

3.6.5 Total Error

Figure 3.19(b) shows the sum of the individual variances: bias, albedo, aerosol, pointing, and retrieval noise errors. The total error bar for the SaskMART technique using both Chappuis and Hartley-Huggins vectors is plotted in Figure 3.19(a) for the sample scan used in this error analysis.

The resultant error profile is a combination of bias error and retrieval vector noise that peaks at both altitude extremes due to the bias error and at the central altitudes due to the retrieval vector noise of the CVTs. The total error varies between two percent and six percent. The other sources of error are very small in comparison and can be safely ignored. This error profile is determined at the same time as the ozone profile itself in the same manner as described in Section 2.8.7.

3.7 Effect of the SaskTRAN Multiple Scattering Parameter on Ozone Retrievals

Figure 3.20 shows the effect of different levels of multiple scattering in the SaskTRAN model on the mean retrieved ozone profile of the first comparison set. The mean retrieved profiles when the model is run with single-scattering only, one, two, and three orders of multiple-scattering is shown. These results show that the model should be run with two orders of multiple-scattering as there is substantial difference between the retrievals for one and two orders, but only a negligible difference between the retrievals for two and three orders of multiple-scattering.

3.8 Conclusion

The MART technique outlined in Section 1.9.4 has been extended to use radiance data from the Hartley-Huggins wavelength band. This data was added in the form of the HVP introduced in Section 3.2.1. The theory and methodology behind the choice of the wavelengths making up the HVP was the subject of Section 3.3. With the wavelengths chosen, the weighting filter function was discussed in Section 3.4. Four comparison sets of the SaskMART ozone density profiles have been performed for SAGE II and SAGE III (Section 3.5). The results were favourable. An error analysis on the combined Chappuis/Hartley-Huggins SaskMART ozone density profiles was discussed in Section 3.6. The effects of multiple scattering on the retrievals was the subject of Section 3.7.

This chapter demonstrates that by adding data from the Hartley-Huggins wavelength band, the SaskMART retrieval technique is extended to between 10 and 60 km. The ozone density profiles calculated compared well with the ozone products of SAGE II and SAGE III.

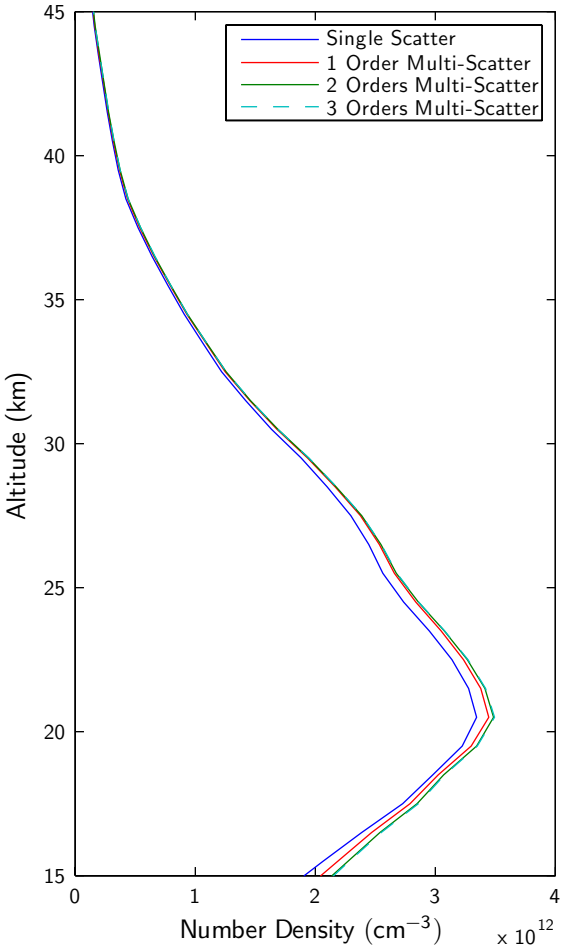

Figure 3.20: The effect of different levels of multiple scattering in the SaskTRAN model on the mean ozone retrieval for the first comparison set. The difference between two orders of multiple scattering and three orders is negligible compared to the error in the retrieval (the dashed curve lies right on top of the green curve).

Chapter 4

Conclusion

The results from the first implementation of the SaskMART retrieval using the SaskTRAN radiative transfer model and the Multiplicative Algebraic Reconstruction technique were presented in Chapter 2. Radiance measurements from wavelengths in the Chappuis absorption band were used in the retrieval. Radiances at three wavelengths were combined to form a Chappuis Vector Triplet. This was done in order to decrease the effects of the Earth albedo and aerosol concentration on the retrieval. Two different CVTs were formed, by varying each of the wavelengths independently, and were weighted equally in the SaskMART retrieval. This had the effect of decreasing the noise in the individual retrieved ozone density profiles and making the retrieval process more stable. The comparisons of the Chappuis-only SaskMART retrieval with those from the OSIRIS Version 2.5 and SAGE II ozone products provided favourable results and demonstrated the viability of the SaskMART retrieval technique. The error analysis showed that the retrieved ozone profiles had an error of five percent from 10–25 km, the error increased to 15% by 40 km.

In an effort to increase the altitude range of the ozone retrievals the Chappuis Vector Triplets investigated in Chapter 2 were combined with Hartley-Huggins Vector Pairs formed with radiance measurements in the blue end of the spectrum. These used an absorbed wavelength and reference wavelength from the Hartley-Huggins ozone absorption region. A discussion of the relationship between absorbed wavelength, optical depth, and tangent height weighting was presented in Chapter 3. Multiple HVPs were formed and combined with the previous CVTs according to a weighting filter function. The comparison sets from SAGE II and SAGE III that were used to validate the combined CVT/HVP retrieval showed favourable results. The error

analysis made on the full retrieval showed that the maximum error in the SaskMART ozone density profiles is six percent. The combination of the HVPs with the CVTs increased the altitude range of the retrievals to 60 km.

The ozone density profiles produced by the SaskMART retrieval can be combined on a global scale to produce ozone maps at a given altitude. Sample ozone maps that demonstrate the features of the vertically resolved OSIRIS/SaskMART data set have been produced. Global maps are shown in Section 4.1, and several maps showing the 2005 ozone hole are presented in Section 4.2.

4.1 Global Ozone Map

The individual ozone measurements shown in Figure 4.1(a) were interpolated to create the ozone map shown in Figure 4.1(b). The individual measurements were interpolated to 2° by 2° bins using the nearest neighbours. The colour white has been used to represent either missing data or where insufficient data is available.

The global ozone distribution shown in Figure 4.1 is typical for that time of year, *i.e.,* lowest over the equator and highest over the northern mid- to high-latitudes.

4.2 Southern Hemisphere Ozone Hole Evolution

Figures 4.2 through 4.7 show the progression of the ozone hole in the southern hemisphere during the austral spring of 2005. Each of the figures shows the ozone number density (cm^{-3}) between 20 and 50 km in 10 km steps. The data has been interpolated to 2° by 2° bins (white areas represent missing data). As the Optical Spectrograph only collects data from the sunlit portion of the atmosphere, the earliest figure (September 10–14) has more missing data around the pole than the following figures.

The ozone hole and its progression can be seen at each of the four altitude shown. The ozone density profiles retrieved by the SaskMART technique makes this type of vertically resolved analysis possible.

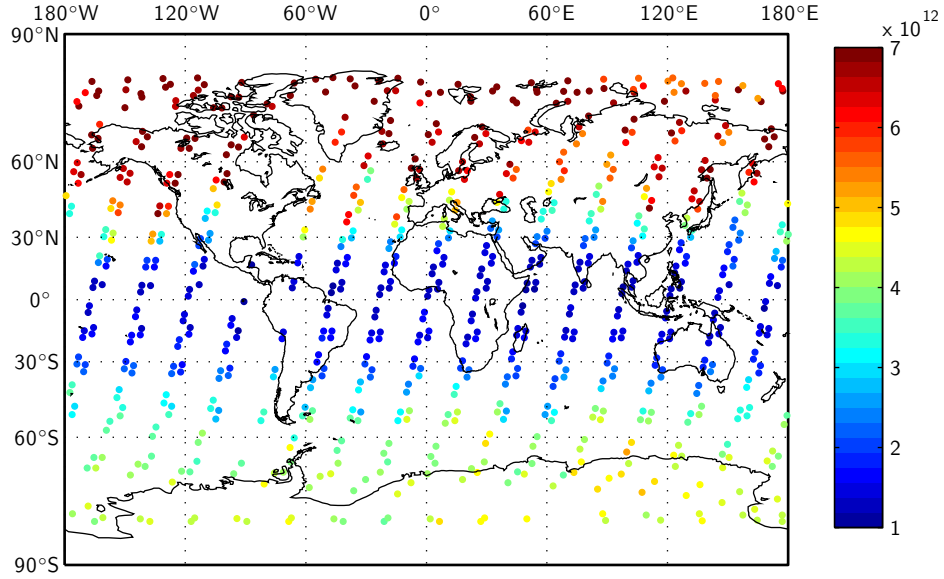

(a) Individual Measurements

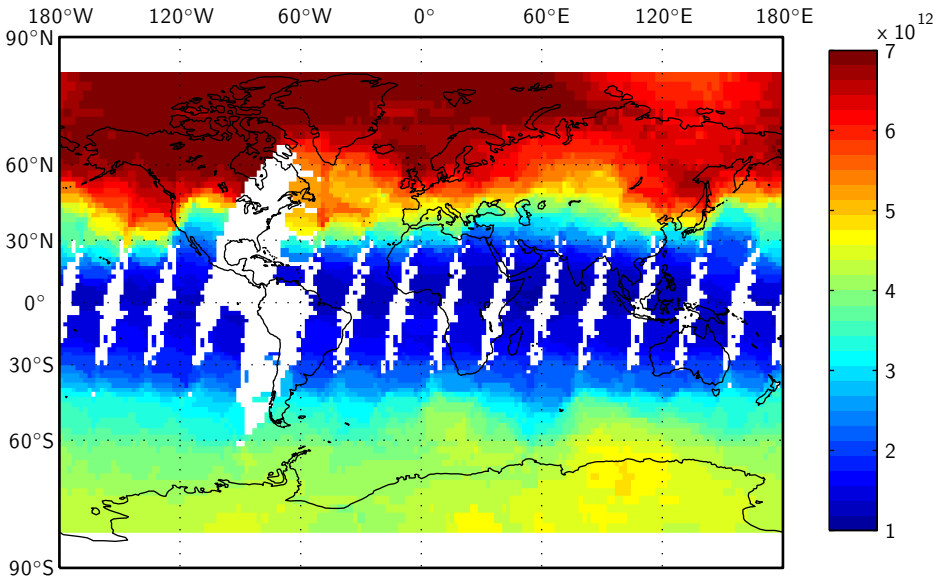

(b) Interpolated Map.

Figure 4.1: Ozone number density (cm^{-3}) at 20 km, February 27 to March 3, 2006 (767 scans).

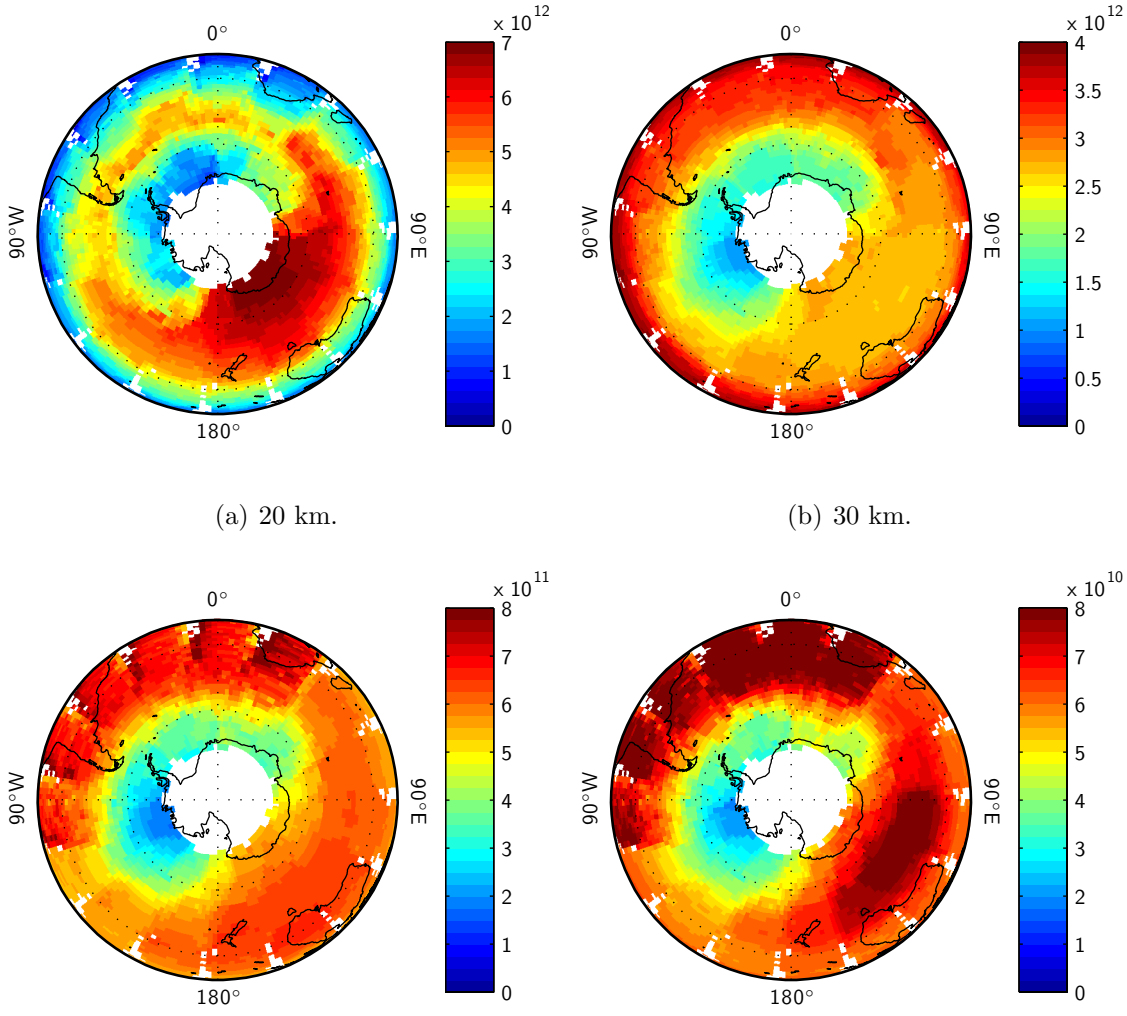

(a) 20 km.

(b) 30 km.

(c) 40 km.

(d) 50 km.

Figure 4.2: South pole ozone number density (cm^{-3}) September 10–14, 2005 (1462 scans).

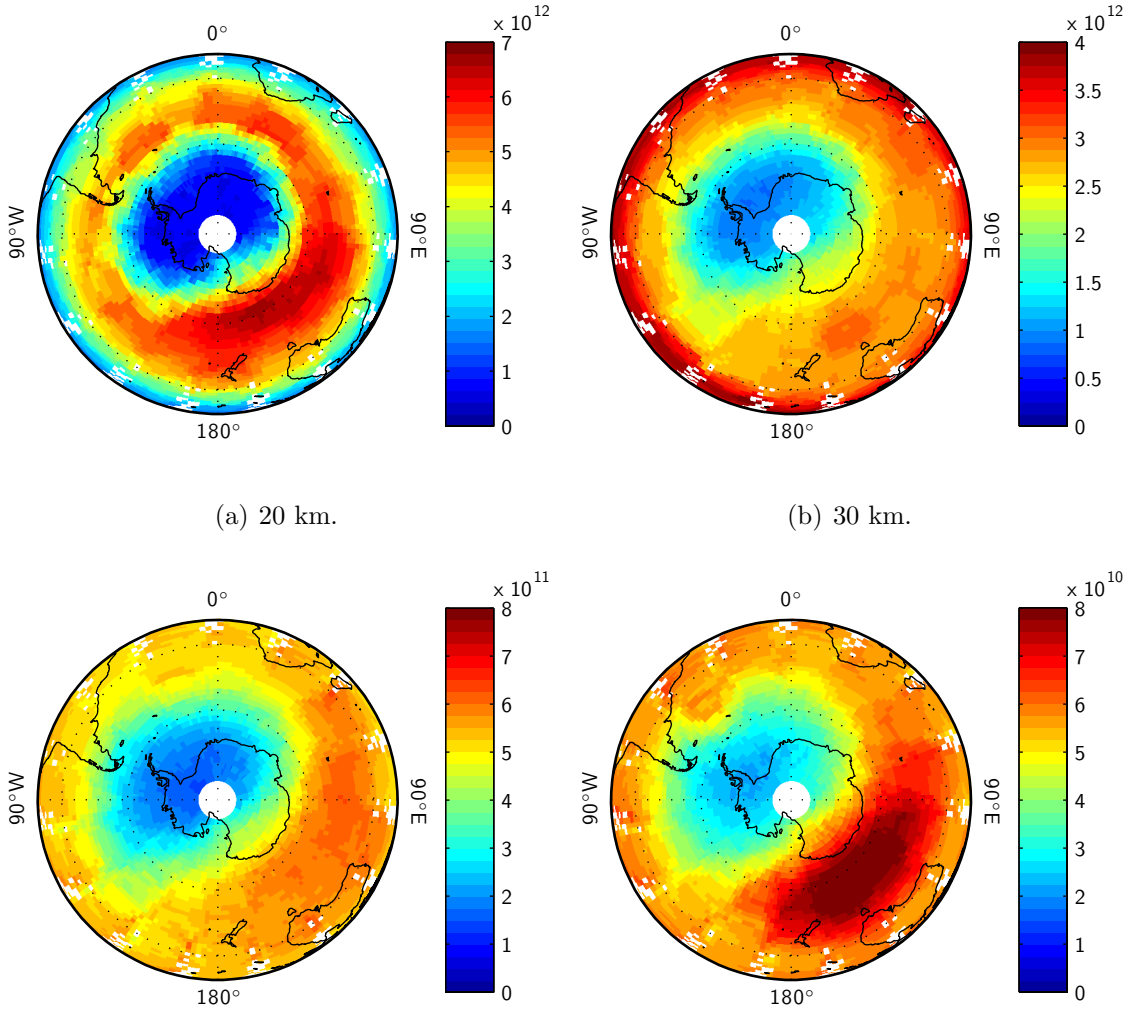

(a) 20 km.

(b) 30 km.

(c) 40 km.

(d) 50 km.

Figure 4.3: South pole ozone number density (cm^{-3}) September 22–26, 2005 (1112 scans).

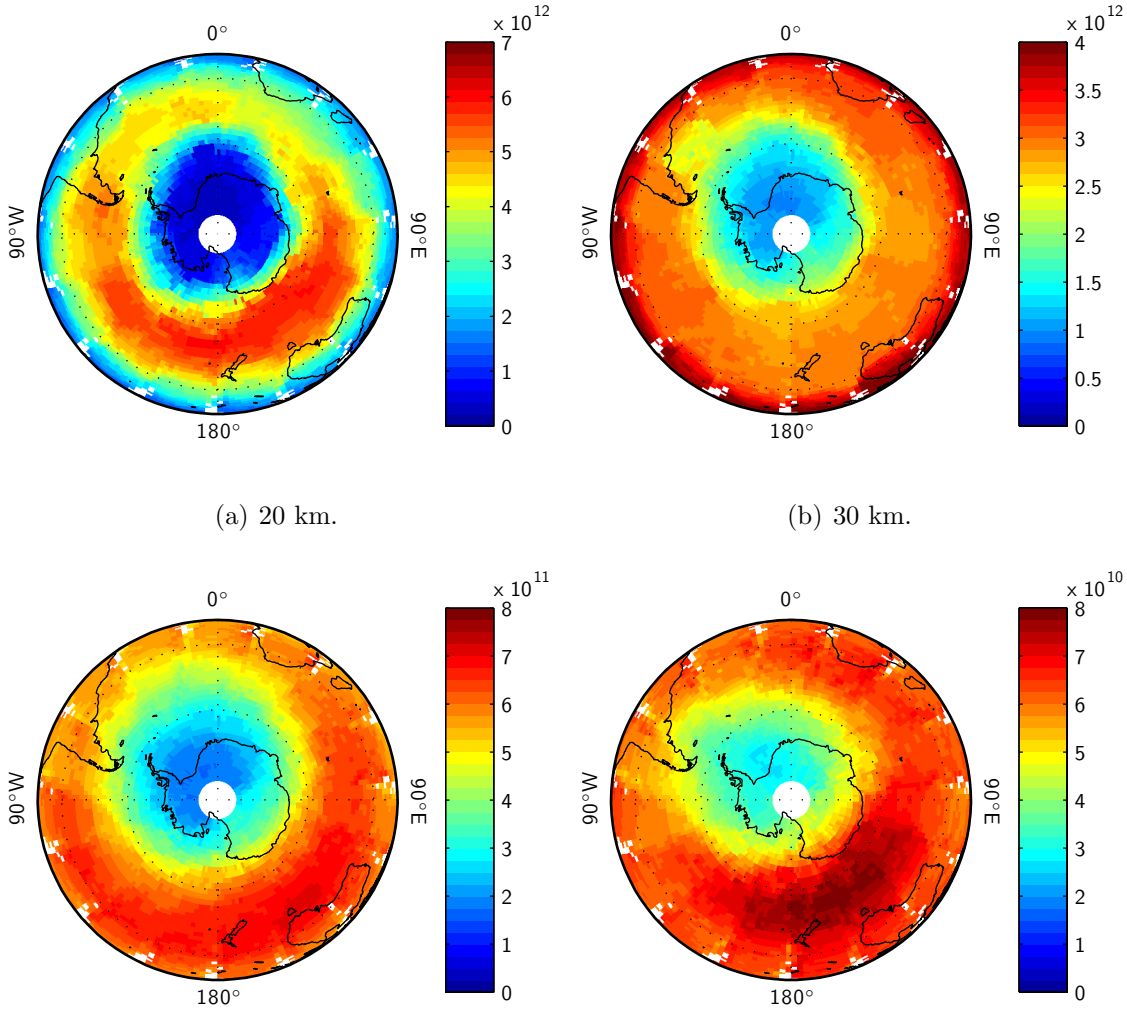

(a) 20 km.

(b) 30 km.

(c) 40 km.

(d) 50 km.

Figure 4.4: South pole ozone number density (cm^{-3}) September 28 to October 2, 2005 (1366 scans).

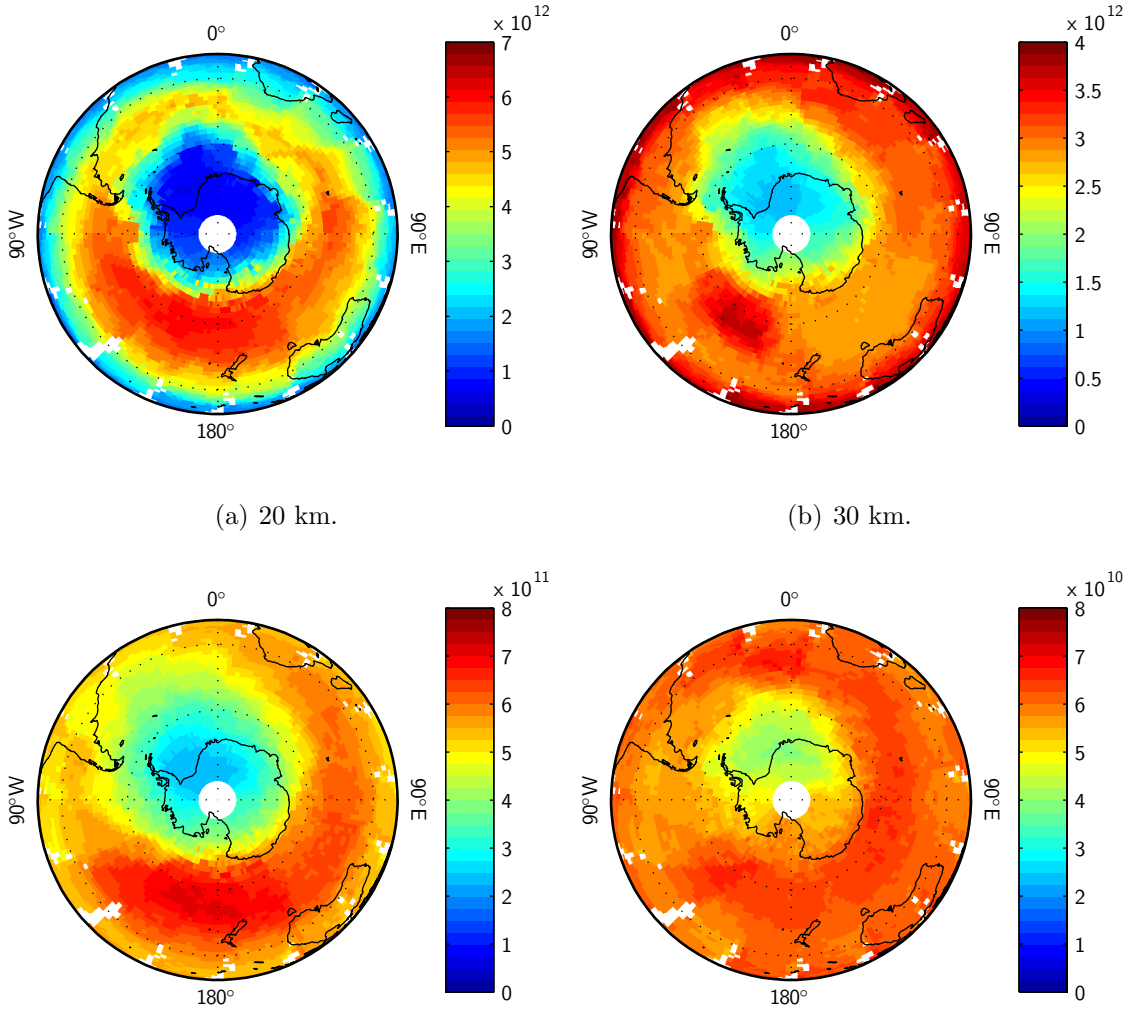

(a) 20 km.

(b) 30 km.

(c) 40 km.

(d) 50 km.

Figure 4.5: South pole ozone number density (cm^{-3}) October 16–20, 2005 (1185 scans).

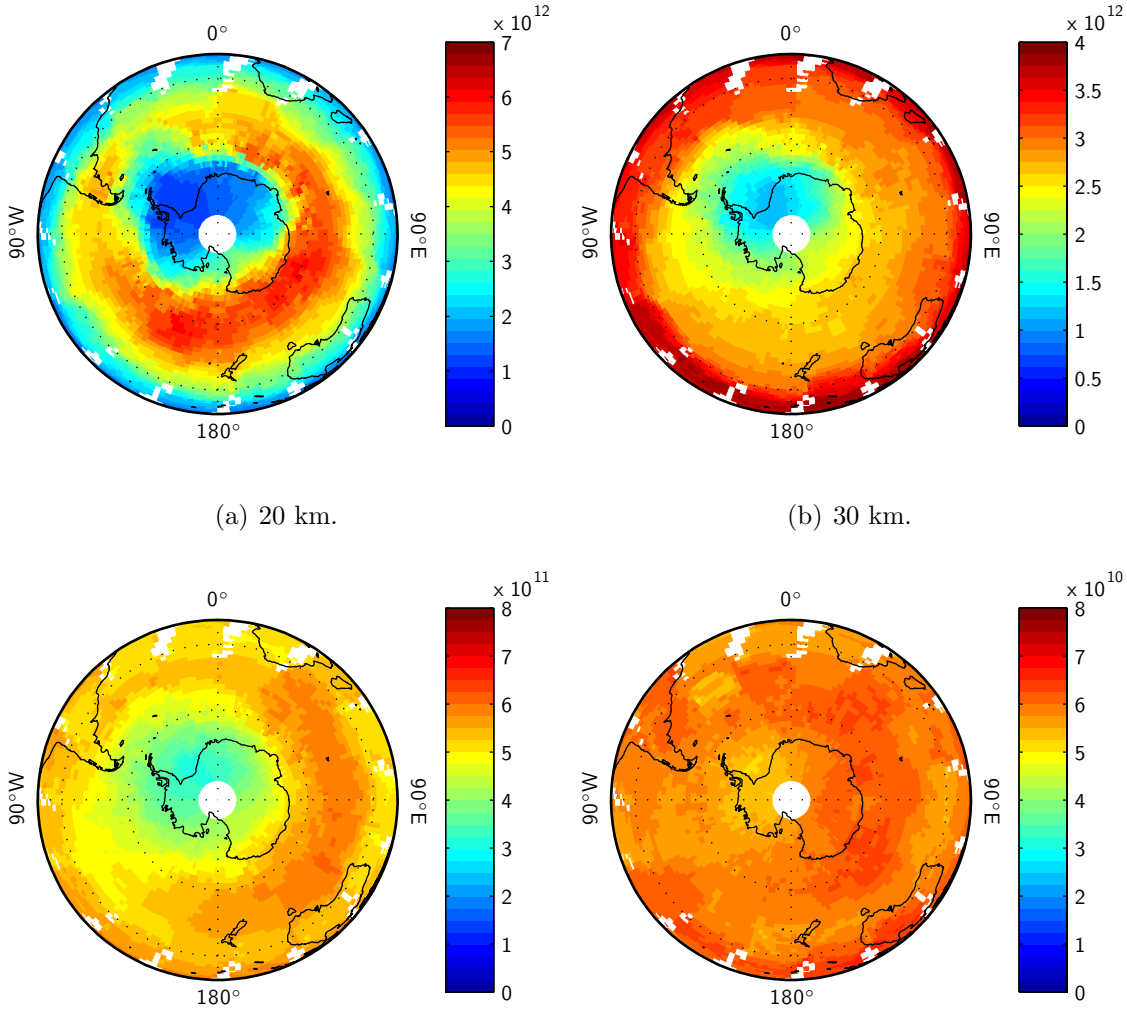

(a) 20 km.

(b) 30 km.

(c) 40 km.

(d) 50 km.

Figure 4.6: South pole ozone number density (cm^{-3}) November 3–7, 2005 (1090 scans).

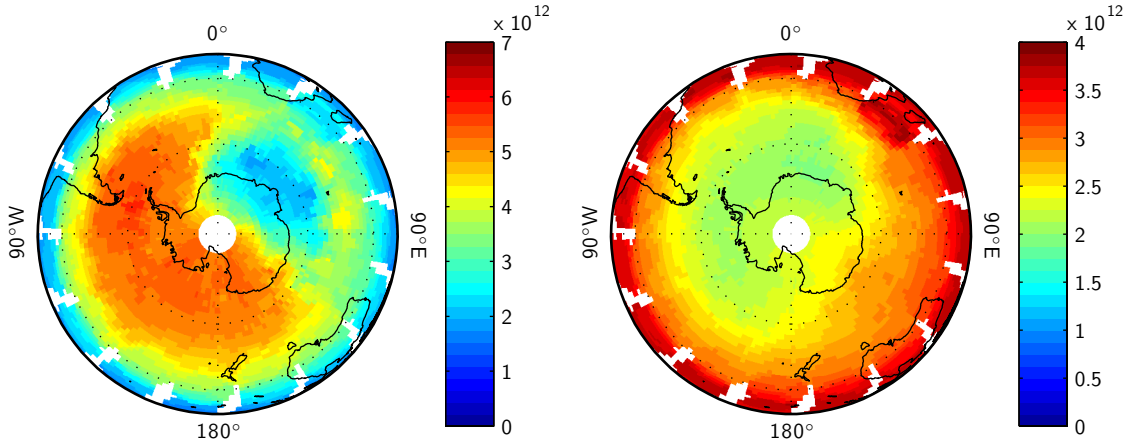

(a) 20 km.

(b) 30 km.

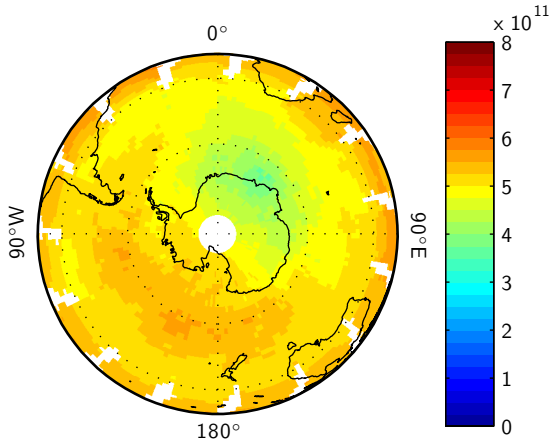

(c) 40 km.

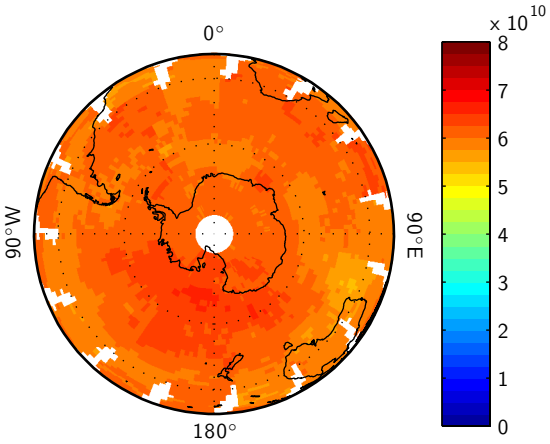

(d) 50 km.

Figure 4.7: South pole ozone number density (cm^{-3}) November 21–25, 2005 (922 scans).

4.3 Future Work

This thesis has presented a new technique for the retrieval of ozone density profiles from limb radiance measurements. It has also presented sample comparison sets that validate the technique. However, the comparison sets will need to be expanded in order to validate the new technique for all viewing conditions. The expanded comparison sets should be taken over a broad range of OSIRIS geometries (*e.g.,* including the complete range of OSIRIS SZAs). The OSIRIS tangent heights used in each retrieval have been calculated using the satellite pointing vectors given by the OSIRIS instrument. An attempt at a better tangent height calculation could be performed using the radiance measurements rather than the satellite pointing vectors. Finally, although the SaskMART retrieval was designed with computational restraints that limit the number of pairs/triplets used in the retrieval and the level of multiple-scattering included in the SaskTRAN model, an investigation into the value of using many more pairs/triplets and higher orders of multiple-scattering should be made.

Bibliography

Auvinen, H., L. Oikarinen, and E. Kyrölä (2002), Inversion algorithms for recovering minor species densities from limb scatter measurements at UV-visible wavelengths, *J. Geophys. Res.*, *107*, ACH 7–1 – ACH 7–7, doi:10.1029/2001JD000407.

Bates, D. R., and M. Nicolet (1950), The photochemistry of atmospheric water vapour, *J. Geophys. Res.*, *55*, 301–327.

Bernath, P. F., C. T. McElroy, et al. (2005), Atmospheric Chemistry Experiment (ACE): Mission overview, *Geophys. Res. Lett.*, *32*, doi:10.1029/2005GL022386.

Bourassa, A. E., D. A. Degenstein, R. L. Gattinger, and E. J. Llewellyn (2006), Stratospheric aerosol retrieval with OSIRIS limb scatter measurements, *J. Geophys. Res.*, submitted.

Bourassa, A. E., D. A. Degenstein, and E. J. Llewellyn (2007), SASKTRAN: A spherical geometry radiative transfer code for measurements of limb scattered sunlight, *J. Quant. Spectrosc. Radiat. Transf.*, submitted.

Bovensmann, H., J. P. Burrows, M. Buchwitz, J. Frerick, S. Noël, V. V. Rozanov, K. V. Chance, and A. P. H. Goede (1999), SCIAMACHY: Mission objectives and measurement modes, *J. Atmos. Sci.*, *56*, 127–150.

Burrows, J. P., A. Richter, A. Dehn, B. Deters, S. Himmelmann, S. Voigt, and J. Orphal (1999), Atmospheric remote sensing reference data from GOME-2, temperature dependent absorption cross sections of O_3 in the 234-794 nm range, *J. Quant. Spectrosc. Radiat. Transf.*, *61*, 509–519.

Burrows, J. P., M. Weber, M. Buchwitz, V. Rozanov, A. Ladstätter-Weißenmayer, A. Richter, R. Debeek, R. Hoogen, K. Bramstedt, K.-U. Eichmann, M. Eisinger, and D. Perner (1999), The global ozone monitoring experiment (GOME): Mission concept and first scientific results, *J. Atmos. Sci.*, *56*, 151–175.

Chahine, M. T. (1970), Inverse problems in radiative transfer: Determination of atmospheric parameters, *J. Atmos. Sci.*, *27*, 960–967.

Chahine, M. T. (1972), A general relaxation method for inverse solution of the full radiative transfer equation, *J. Atmos. Sci.*, *29*, 741–747.

Chapman, S. (1930), A theory of upper-atmosphere ozone, *Mem. Roy. Meteorol. Soc.*, *3*, 103–125.

Chappuis, J. (1882), Etude spectroscopique sur l'ozone, *Ann. Sci. Éc. Norm. Sup.*, *11*, 137–186.

Chu, W. P., M. P. McCormick, J. Lenoble, C. Brogniez, and P. Pruvost (1989), SAGE II inversion algorithm, *J. Geophys. Res.*, *94*, 8339–8351.

Cicerone, R. J. (1974), Stratospheric ozone destruction by man-made chloroflouromethanes, *Science*, *185*, 1165–1167.

Cunnold, D. M., W. P. Chu, M. P. McCormick, R. E. Veiga, and R. A. Barnes (1989), Validation of SAGE II ozone measurements, *J. Geophys. Res.*, *94*, 8447–8460.

Degenstein, D. (1999), Atmospheric tomography, Ph.D. thesis, University of Saskatchewan.

Flittner, D. E., P. K. Bhartia, and B. M. Herman (2000), O_3 profiles retrieved from limb scatter measurements: Theory, *Geophys. Res. Lett.*, *27*, 2601–2604, doi:10.1029/1999GL011343.

Griffioen, E., and L. Oikarinen (2000), LIMBTRAN: A pseudo three-dimensional radiative transfer model for the limb-viewing imager OSIRIS on the Odin satellite, *J. Geophys. Res.*, *105*, 29,717–29,730, doi:10.1029/2000JD900566.

Haley, C. S., S. M. Brohede, C. E. Sioris, E. Griffioen, D. P. Murtagh, I. C. McDade, P. Eriksson, E. J. Llewellyn, A. Bazureau, and F. Goutail (2004), Retrieval of stratospheric O_3 and NO_2 profiles from Odin Optical Spectrograph and Infrared Imager System (OSIRIS) limb-scattered sunlight measurements, *Journal of Geophysical Research (Atmospheres)*, *109*, D16,303, doi:10.1029/2004JD004588.

Hartley, W. N. (1881a), On the absorption spectrum of ozone, *J. Chem. Soc.*, *39*, 57.

Hartley, W. N. (1881b), On the absorption of solar rays by atmospheric ozone, *J. Chem. Soc.*, *39*, 111–128.

Heath, D. F., A. J. Krueger, H. A. Roeder, and B. D. Henderson (1975), The Solar Backscatter Ultraviolet and Total Ozone Mapping Spectrometer /SBUV/TOMS/ for Nimbus G, *Opt. Eng.*, *14*, 323–331.

Herman, B. M., A. Ben-David, and K. J. Thome (1994), Numerical technique for solving the radiative transfer equation for a spherical shell atmosphere, *Appl. Opt.*, *33*, 1760–1770.

Houzeau, A. (1858), Preuve de la présence dans l'atmosphère d'un nouveau principe gazeux l'oxygene naissant, *C. R. Acad. Sci. Paris*, *46*, 89–91.

Lindemann, F. A., and G. M. B. Dobson (1923), A theory of meteors, and the density and temperature of the outer atmosphere to which it leads, *Proc. Roy. Soc. A*, *102*, 411–437.

Llewellyn, E. J., N. D. Lloyd, D. A. Degenstein, R. L. Gattinger, S. V. Petelina, A. E. Bourassa, J. T. Wiensz, E. V. Ivanov, I. C. McDade, B. H. Solheim, J. C. McConnell, C. S. Haley, C. von Savigny, C. E. Sioris, C. A. McLinden,

E. Griffioen, J. Kaminski, W. F. Evans, E. Puckrin, K. Strong, V. Wehrle, R. H. Hum, D. J. W. Kendall, J. Matsushita, D. P. Murtagh, S. Brohede, J. Stegman, G. Witt, G. Barnes, W. F. Payne, L. Piché, K. Smith, G. Warshaw, D.-L. Deslauniers, P. Marchand, E. H. Richardson, R. A. King, I. Wevers, W. McCreath, E. Kyrölä, L. Oikarinen, G. W. Leppelmeier, H. Auvinen, G. Mégie, A. Hauchecorne, F. Lefèvre, J. de La Nöe, P. Ricaud, U. Frisk, F. Sjoberg, F. von Schéele, and L. Nordh (2004), The OSIRIS instrument on the Odin spacecraft, *Can. J. Phys.*, *82*, 411–422.

Loughman, R. P., E. Griffioen, L. Oikarinen, O. V. Postylyakov, A. Rozanov, D. E. Flittner, and D. F. Rault (2004), Comparison of radiative transfer models for limb-viewing scattered sunlight measurements, *J. Geophys. Res.*, *109*, 1–16, doi: 10.1029/2003JD003854.

Lucke, R. L., D. R. Korwan, R. M. Bevilacqua, J. S. Hornstein, E. P. Shettle, D. T. Chen, M. Daehler, J. D. Lumpe, M. D. Fromm, D. Debrestian, B. Neff, M. Squire, G. König-Langlo, and J. Davies (1999), The polar ozone and aerosol measurement (POAM) III instrument and early validation results, *J. Geophys. Res.*, *104*, 18,785–18,800, doi:10.1029/1999JD900235.

McCormick, M. P., J. M. Zawodny, R. E. Beiga, J. C. Larsen, and P. H. Wang (1989), An overview of SAGE I and II ozone measurements, *Planet. Space Sci.*, *37*, 1567–1586.

McCormick, M. P., W. P. Chu, J. M. Zawodny, L. E. Mauldin III, and L. R. McMaster (1991), Stratospheric Aerosol and Gas Experiment III (SAGE III) aerosol and trace gas measurements for Earth Observing System (EOS), *Proceedings SPIE Int. Soc. Opt. Eng.*, *1491*, 125–141.

McDade, I. C., K. Strong, C. S. Haley, J. Stegman, D. P. Murtagh, and E. J. Llewellyn (2002), A method for recovering stratospheric minor species densities from the Odin/OSIRIS scattered-sunlight measurements, *Can. J. Phys.*, *80*, 395–408.

McLinden, C. A., J. C. McConnell, E. Griffioen, and C. T. McElroy (2002), A vector radiative-transfer model for the Odin/OSIRIS project, *Can. J. Phys.*, *80*, 375–393.

McPeters, R. D., S. J. Janz, E. Hilsenrath, T. L. Brown, D. E. Flittner, and D. F. Heath (2000), The retrieval of O_3 profiles from limb scatter measurements: Results from the shuttle ozone limb sounding experiment, *Geophys. Res. Lett.*, *27*, 2597–2600, doi:10.1029/1999GL011342.

Molina, M. J., and F. S. Rowland (1974), Stratospheric sink for chloroflouromethanes: Chlorine atom catalysed destruction of ozone, *Nature*, *249*, 810–812.

Murtagh, D., U. Frisk, F. Merino, M. Ridal, A. Jonsson, J. Stegman, G. Witt, P. Eriksson, C. Jiménez, G. Megie, J. de La Noë, P. Ricaud, P. Baron, J. R. Pardo, A. Hauchcorne, E. J. Llewellyn, D. A. Degenstein, R. L. Gattinger, N. D. Lloyd, W. F. J. Evans, I. C. McDade, C. S. Haley, C. Sioris, C. von Savigny,

B. H. Solheim, J. C. McConnell, K. Strong, E. H. Richardson, G. W. Leppelmeier, E. Kyrölä, H. Auvinen, and L. Oikarinen (2002), Review: An overview of the Odin atmospheric mission, *Can. J. Phys.*, *80*, 309–319.

Newchurch, M. J., E.-S. Yang, D. M. Cunnold, G. C. Reinsel, J. M. Zawodny, and J. M. Russell III (2003), Evidence for slowdown in stratospheric ozone loss: First stage of ozone recovery, *J. Geophys. Res.*, *108*, 4507, doi:10.1029/2003JD003471.

Oikarinen, L. (2001), Polarization of light in UV-visible limb radiance measurements, *J. Geophys. Res.*, *106*, 1533–1544, doi:10.1029/2000JD900442.

Oikarinen, L. (2002), Effect of surface albedo variations on UV-visible limb-scattering measurements of the atmosphere, *J. Geophys. Res.*, *107*, 4404, doi:10.1029/2001JD001492.

Oikarinen, L., E. Sihvola, and E. Kyrölä (1999), Multiple scattering radiance in limb-viewing geometry, *J. Geophys. Res.*, *104*, 31,261–31,274, doi:10.1029/1999JD900969.

Puliafito, E., R. Bevilacqua, J. Olivero, and W. Degenhardt (1995), Retrieval error comparison for several inversion techniques used in limb-scanning millimeter-wave spectroscopy, *J. Geophys. Res.*, *100*, 14,257–14,268, doi:10.1029/95JD00212.

Rault, D. F. (2004), Ozone, NO_2 and aerosol retrieval from SAGE III limb scatter measurements, *Proceedings SPIE Int. Soc. Opt. Eng.*, *5571*, 205–216.

Rault, D. F. (2005), Ozone profile retrieval from Stratospheric Aerosol and Gas Experiment (SAGE III) limb scatter measurements, *J. Geophys. Res.*, *110*, 1–14, doi:10.1029/2004JD004970.

Rind, D., and M. McCormick (2002), *SAGE III: Algorithm Theoretical Basis Documents for Solar Lunar Products*, EOS Project Science Office, Goddard Space Flight Center.

Rodgers, C. D. (1976), Retrieval of atmospheric temperature and composition from remote measurements of thermal radiation, *Rev. Geophys. Space Phys.*, *14*, 609–624.

Rodgers, C. D. (2000), *Inverse methods for atmospheric sounding: theory and practice*, 167-186, World Scientific.

Rozanov, A. V., V. V. Rozanov, and J. P. Burrows (2000), Combined differential-integral approach for the radiation field computation in a spherical shell atmosphere: Nonlimb geometry, *J. Geophys. Res.*, *105*, 22,937–22,942, doi:10.1029/2000JD900378.

Rusch, D. W., G. H. Mount, C. A. Barth, R. J. Thomas, and M. T. Callan (1984), Solar mesospheric explorer ultraviolet spectrometer: Measurements of ozone in the 1.0–0.1 mbar region, *J. Geophys. Res.*, *89*, 11,677–11,687.

Russell, J. M., L. L. Gordley, J. H. Park, S. R. Drayson, W. D. Hesketh, R. J. Cicerone, A. F. Tuck, J. E. Frederick, J. E. Harries, and P. J. Crutzen (1993), The halogen occultation experiment, *J. Geophys. Res.*, *98*, 10,777–10,797.

Schönbein, C. F. (1840), Recherches sur la nature de l'odeur qui se manifeste dans certaines actions chimiques, *C. R. Acad. Sci. Paris*, *10*, 706–710.

Sioris, C. E., C. S. Haley, C. A. McLinden, C. von Savigny, I. C. McDade, J. C. McConnell, W. F. J. Evans, N. D. Lloyd, E. J. Llewellyn, K. V. Chance, T. P. Kurosu, D. Murtagh, U. Frisk, K. Pfeilsticker, H. Bösch, F. Weidner, K. Strong, J. Stegman, and G. Mégie (2003), Stratospheric profiles of nitrogen dioxide observed by Optical Spectrograph and Infrared Imager System on the Odin satellite, *J. Geophys. Res.*, *108*, 4215, doi:10.1029/2002JD002672.

Strong, K., B. M. Joseph, R. Dosanjh, I. C. McDade, C. A. McLinden, J. C. McConnell, J. Stegman, D. P. Murtagh, and E. J. Llewellyn (2002), Retrieval of vertical concentration profiles from OSIRIS UV-visible limb spectra, *Can. J. Phys.*, *80*, 409–434.

von Savigny, C., I. C. McDade, E. Griffioen, C. S. Haley, C. E. Sioris, and E. J. Llewellyn (2005), Sensitivity studies and first validation of stratospheric ozone profile retrievals from Odin/OSIRIS observations of limb-scattered solar radiation, *Can. J. Phys.*, *83*, 957–972.

von Savigny, C., C. S. Haley, C. E. Sioris, I. C. McDade, E. J. Llewellyn, D. Degenstein, W. F. J. Evans, R. L. Gattinger, E. Griffioen, E. Kyrölä, N. D. Lloyd, J. C. McConnell, C. A. McLinden, G. Mégie, D. P. Murtagh, B. Solheim, and K. Strong (2003), Stratospheric ozone profiles retrieved from limb scattered sunlight radiance spectra measured by the OSIRIS instrument on the Odin satellite, *Geophys. Res. Lett.*, *30*, 1755, doi:10.1029/2002GL016401.

Wayne, R. P. (2000), *Chemistry of Atmospheres*, chap. Ozone in Earth's stratosphere, 155–320, 3rd ed., Oxford University Press, Oxford.

Weatherhead, E. C., G. C. Reinsel, G. C. Tiao, C. H. Jackman, L. Bishop, S. M. H. Firth, J. DeLuisi, T. Keller, S. J. Oltmans, E. L. Fleming, D. J. Wuebbles, J. B. Kerr, A. J. Miller, J. Herman, R. McPeters, R. M. Nagatani, and J. E. Frederick (2000), Detecting the recovery of total column ozone, *J. Geophys. Res.*, *105*, 22,201–22,210, doi:10.1029/2000JD900063.